

**WA School of Mines, Energy and Chemical Engineering
Centre for Exploration Geophysics**

**Modelling elastic properties of clastic rocks from
microtomographic images using multi-mineral segmentation
and machine learning**

Jiabin Liang

0000-0002-0105-193X

**This thesis is presented for the Degree of
Doctor of Philosophy
of
Curtin University**

February 2022

Declaration

To the best of my knowledge and belief this thesis contains no material previously published by any other person except where due acknowledgment has been made.

This thesis contains no material which has been accepted for the award of any other degree or diploma in any university.

Signature:

Date: 20.02.2022

Abstract

The essence of rock physics consists of finding relationships between pore-scale characteristics and elastic properties estimated from geophysical data. Theoretical rock physics models based on idealised microstructures have given important insights to understanding of such relationships. However, because of variability of rock geologic histories, structures and textures, these models must always contain several parameters (such as pore aspect ratios, coordination numbers etc.), which are usually adjusted to measured velocities. This limits the predictive power of these models. At the same time, high resolution tomographic images are often available. Such data can provide detailed information about the rock structure. Furthermore, digital rock physics (DRP) enables direct calculation of effective elastic properties from tomographic images using different numerical schemes. Thus, DRP could act as a great tool to study on the relationship between effective elastic properties and pore-scale characteristics of rock, and potentially be used to constrain the theoretical rock physics models.

In this research, I will first build a digital rock physics workflow by numerical computation of elastic properties with finite element method based on X-ray micro-Computed Tomography (micro-CT) images of Bentheimer sandstones. The effect of sample size and micro-CT resolution on the computed elastic properties will be evaluated. Furthermore, a novel segmentation workflow will be built to detect feldspar and clay minerals in micro-CT images, despite their grayscale similarity to quartz. The simulated results based on the segmented multi-mineral labels will be compared against core measurements (Chapter 2).

Elastic properties of sandstones can be highly pressure dependent. However, the pressure-induced deformation of intact sandstones in micro-CT images are below the resolving power of conventional image analysis methods. Also, most digital rock physics studies of the elastic properties operate with micro-CT images acquired at ambient pressure. In Chapter 3, I will perform a comprehensive analysis of micro-CT images acquired at a variety of pressures using a reservoir sandstone sample with pronounced stress-sensitivity. A purpose-built X-ray-transparent pressure cell enables scanning micro-CT images at confining pressures of up to 36 MPa. The pressure effect

on high-resolution micro-CT images of sandstone sample and elastic properties computed from these images will be investigated.

Grain contact stiffness is crucial for predicting the effective elastic moduli of sandstones, and the change of effective elastic moduli in different cementation and pressure conditions. Contact stiffness cannot be measured directly with any current method. Even with the latest synchrotron-based X-ray tomographic microscopy, micro-CT still cannot resolve the majority of soft pores at grain contacts due to resolution limitation. These missing information lead to an overestimation of computed elastic moduli in DRP. In Chapter 4, I reconstruct the contacts according to the morphology of grains using watershed separation algorithm. These approximated grain contacts can then be used as a uniform phase with lower moduli in the numerical computation. In this way, the effect of unresolved soft pores is taken into account, so the computed moduli can be in a reasonable agreement with laboratory ultrasonic measurements. At the same time, the stiffness of contact phase can be inverted in this matching experiment. This inverted stiffness is a valuable information for understanding cementation or stress effect on the grain contact.

The micro-CT image segmentation workflow developed in Chapter 2 consists of many stages, and thus becomes time and computationally expensive and involves a lot of manual labour. In Chapter 5, I propose an automated workflow for the multi-mineral segmentation of micro-CT images using a convolutional neural network (CNN). The CNN model is trained using labels of two sets of images of a Bentheimer sandstone that are segmented into pore, quartz, clay and feldspar using a segmentation workflow, which is introduced in Chapter 2. The trained model is then used to segment a new set of images of the Bentheimer sandstone. The segmented multi-mineral labels can achieve an accuracy of $\sim 97\%$ and the process takes only ~ 10 minutes as compared with interactive workflow which takes ~ 3 hours. The methodology developed in this study is not limited to the segmentation of micro-CT images of sandstones. A specific segmentation workflow may be designed, where segmentation for other kinds of rock or material is required. Then, a CNN model can be used to automate and standardize the segmentation process.

In summary, this thesis provides a comprehensive study on digital rock physics in elastic properties estimation of sandstones, which includes scanning, segmentation and

computation. Significant improvement on micro-CT image multi-mineral segmentation is achieved with an advanced workflow and then automated with convolutional neural network. Furthermore, the pressure effect on micro-CT images of sandstone is successfully detected and the effect on computed effective elastic properties is evaluated. The well-developed digital rock physics workflow is applied to understand the grain contact stiffness in sandstones with different cementation conditions or under different pressures.

Acknowledgements

I am extremely fortunate and deeply grateful to be supervised by my outstanding and devoting thesis committee. I would like to thank my supervisor Prof Boris Gurevich, co-supervisor Prof Maxim Lebedev, associate supervisor Dr Stanislav Glubokovskikh and chairperson Dr Stephanie Vialle. Thank you all for the great support to my research and generous sharing your expertise. I am impressed and inspired by your enthusiasm for research. I benefit tremendously by learning the immense knowledge and research skills from you through my PhD journey. Special thanks go to Dr Stanislav Glubokovskikh, who was the main supervisor for the first two years of my PhD study, for his guidance in my research and life.

Thanks go to Prof Christoph Arns for his great support in the numerical simulations and insightful discussions. Thanks to Prof Maxim Lebedev, Dr Stephanie Vialle, Dr Alexey Yurikov and Dr Lionel Esteban for conducting laboratory measurements. Thanks to Dr Zubair Ahmed, Dr Michel Nzikou and Dr Yongyang Sun for the discussion on the micro-CT image processing and machine learning algorithms. Thank you all my colleagues at the Centre for Exploration Geophysics, at Curtin University, for your joyful company in the research journey.

I would like to thank Curtin University for granting Curtin Strategic Stipend Scholarship to support my PhD study. I also thank sponsors of Curtin Reservoir Geophysics Consortium for their financial support. Special thanks go to Santos Limited for the financial support, data sharing and technical discussion. This study would not be possible without resources provided by the Pawsey Supercomputing Centre with funding from the Australian Government and the Government of Western Australia.

Finally, I would like to thank my family for their unconditional love and support. This PhD journey would not be possible without your great sacrifice.

Contents

Chapter 1 Introduction.....	1
1.1 Background and motivation	1
1.2 Objectives	7
1.3 Thesis outline and related publications	9
1.4 Author’s contributions.....	10
1.5 List of publications related to the research project.....	10
Chapter 2 Digital rock physics workflow for elastic moduli estimation from micro-CT images of sandstones	12
2.1 Introduction.....	12
2.2 The laboratory data set.....	14
2.3 Scanning effects evaluation	17
2.3.1 Numerical simulations	18
2.3.2 Scanning parameters and resolution-size trade-off.....	20
2.4 Specialised image processing for arenites	24
2.4.1 Suppression of random noise	25
2.4.2 Standard techniques for multi-mineral segmentation	26
2.4.3 Four-phase multi-mineral segmentation: clay segmentation	27
2.4.4 Four-phase multi-mineral segmentation: feldspar segmentation	28
2.5 Effective moduli computation with reduced mineral moduli	30
2.5.1 Multi-mineral matrix.....	31
2.5.2 Reduced matrix moduli.....	32
2.6 Discussion.....	34
2.7 Conclusions.....	35
Chapter 3 Tracking the stress effect on micro-CT images of a reservoir sandstone.....	37
3.1 Introduction.....	37

3.2 Laboratory characterisation of sandstone sample.....	39
3.3 Pressure effect detection method.....	42
3.4 Estimates of the static moduli.....	45
3.5 Comparison between static and dynamic bulk moduli.....	46
3.6 Pressure effect on computed elastic moduli.....	47
3.7 Discussion.....	48
3.8 Conclusions.....	49
Chapter 4 Grain contact stiffness inversion with digital rock physics.....	51
4.1 Introduction.....	51
4.2 The laboratory study.....	53
4.2.1 Ultrasonic and porosity measurements.....	54
4.2.2 Micro-CT imaging.....	55
4.2.3 Nuclear Magnetic Resonance for pore size distribution estimation.....	57
4.2.4 Nano-indentation as a reference for mineral moduli.....	58
4.3 Micro-CT image processing, segmentation and grain contact reconstruction..	61
4.4 Grain contact moduli inversion.....	62
4.5 Discussion.....	65
4.6 Conclusions.....	66
Chapter 5 Multi-mineral segmentation of micro-CT images using a convolutional neural network.....	67
5.1 Introduction.....	67
5.2 Micro-CT images of a Bentheimer sandstone.....	69
5.3 Multi-mineral segmentation through a workflow.....	70
5.4 Convolutional neural network setup.....	71
5.5 Results.....	73
5.6 Discussion.....	75
5.7 Conclusions.....	77

Chapter 6 Conclusions and future work.....	78
6.1 Conclusions.....	78
6.2 Future work.....	80
References	81
List of Figures.....	95
List of Tables	100
Appendix A: Co-author contribution table	101
Appendix B: Copyright Information.....	103

Chapter 1 Introduction

1.1 Background and motivation

Direct access to log and core data from deep geological reservoirs is always sparse due to the limited number of wells. Hence, extrapolation of the rock properties away from the wells is often done using quantitative interpretation of seismic volumes (Avseth, Mukerji, & Mavko, 2010). This requires the knowledge of the relationship between observed seismic parameters and petrophysical properties of the subsurface, which is the central topic of the rock physics discipline. Seismic properties are controlled by at least three main factors: mineral composition of the rock frame, rock microstructure and fluid saturation. When microstructure is not known, Hashin-Shtrikman bounds provide the rigorous range of effective properties based on the volume fractions and moduli of the constituents (Hashin & Shtrikman, 1963). However, for porous sedimentary rocks, the upper and lower bounds are quite far apart due to the large contrast among different minerals in rock matrix and pore fluid. Thus, theoretical rock physics models have been developed to estimate the elastic moduli of rocks more accurately.

Naturally, real rocks have very complex microstructure, so that their deformation is analytically intractable. Therefore, theoretical models to estimation of their elastic moduli are inevitably based on some simplifying assumptions about the rock geometry and deformation process itself (Berryman, 1995; Watt, Davies, & O'Connell, 1976). The modelling procedures usually consist of two steps: (1) deformation of an isolated and idealised pore/matrix configuration is derived; (2) cumulative effect of such building blocks is then found according to their spatial distribution (volume concentration, spacing etc.). For loose clastic sediments, spherical grain assemblage is the most appropriate (Digby, 1981; Norris & Johnson, 1997; Walton, 1987), and rock physics models based on this approximation are normally called contact models. Most of these models are based on the Hertz-Mindlin solution (Mindlin, 1949) for the elastic behaviour of two identical elastic spheres in contact. Then, the estimated effective moduli depend on the average number of contacts per grain. Conversely, for consolidated rocks, elastic properties are often modelled with an alternative approach called inclusion models—isolated pores are embedded in the solid matrix. Eshelby (1957) found deformation of an isolated ellipsoidal inclusion in the homogeneous

infinite medium. This idealised pore shape became very popular because it captures isometric matrix pores, thin cracks and needle-shaped pore throats. Kuster and Toksöz (1974) derived expressions for P- and S-wave velocities for a variety of simple inclusion shapes with dilute concentrations in low porosity rocks. This approach was extended to arbitrary concentrations of inclusions using a self-consistent method which approximates interaction between inclusions by replacing the background medium with the as-yet-unknown effective medium (O'Connell & Budiansky, 1974). Another way to extend the Kuster and Toksöz (1974) to higher concentration is by using it in an iterative manner by incrementally adding inclusions of one phase (phase 2) to the matrix phase until the desired proportion of the constituents is reached (Norris, Sheng, & Callegari, 1985). This approach is called Differential Effective Medium or DEM.

A single model is unlikely to capture the entire range of clastic rocks. More advanced integrated rock physics models have been developed to cover a broader porosity range and reduce the uncertainty using geological constraints on rock microstructure. Avseth et al. (2010) used a series of contact models to estimate the elastic properties of rocks with higher porosity and then applied modified Hashin-Shtrikman bounds to deduce the elastic properties of rocks with lower porosity in different geologic trends. Dræge, Johansen, Brevik, and Dræge (2006) developed a composite rock physics model with a selection of some contact models and inclusion models in different processes of diagenesis. A distribution scheme for quartz cement, K-feldspar and some of the most common clay minerals in sandstones (illite, kaolinite, smectite and chlorite) was suggested on the basis of thin-section observations. The predictable mineral reaction paths during burial and increasing temperature were then entered into the composite rock physics model to reproduce the diagenetic evolution of seismic rock properties. In another approach, Vernik and Kachanov (2010) built a sand diagenesis model for the entire range of porosities by combining the inclusion models and empirical relations. In the consolidated regime, the modelling is micromechanics based and yields the moduli in terms of porosity, pore-shape factor, and crack density, based on the non-interaction approximation with the Mori-Tanaka correction for interactions (Mori & Tanaka, 1973). By necessity, this approach contains empirical parameters reflecting highly irregular shapes of pores and micro cracks. In the unconsolidated

regime, Vernik and Kachanov (2010) proposed empirical relations of the Mori-Tanaka type where pore-shape factors assume large values, consistent with very soft, concave pore shapes typical in this regime.

Even though these advanced rock physics models are more informed by geology, they are still based on rather schematic topological arrangement. They use conceptual spatial characteristics that may not be simple to derive from the images of rock samples, such as crack density, aspect ratio and grains radii. The uncertainties related to describing these shape parameters reduces the predictive power of these models because of variability of rock geologic histories, structures and textures (Vernik, 2016). A high-quality match between model results and measured data does not necessarily indicate that the model is yielding useful information about the underlying controls on velocities (Smith, 2011), or even that the geometrical configuration underlying the model is an adequate representation of the rock structure.

With the rapid advances in computing capacity, Digital Rock Physics (DRP) has emerged as an tool for the analysis of pore-scale processes governing effective rock properties (Andrä et al., 2013a). This technique relies on numerical simulations of rock deformation for a given rock microstructure, which may be obtained directly from stochastic simulations, process-based methods or real rock images (Sain, 2010). The stochastic methods could reconstruct the structure of general random heterogeneous media from limited morphological information artificially designed or obtained from 2D thin sections (Yeong & Torquato, 1998a, 1998b). Process-based discrete element method may simulate spherical grain and even irregularly shaped grains packing deposit. Computational diagenesis schemes could mimic rock microstructures changes due to geological factors including deposition (grain size distribution, mineralogy), stress conditions (isotropic and anisotropic) and diagenesis (quartz overgrowth, cementation mode and cement material) (Al Ibrahim, Kerimov, Mukerji, & Mavko, 2018; García & Medina, 2007; Sain, 2010). Then, effective elastic properties of the generated models can be calculated using various numerical schemes (Andrä et al., 2013b).

High resolution tomographic data provide detailed information about the rock structure and could be used to describe pore geometry. Microstructure of real rocks can be obtained using micro-CT, short for micro-scale X-ray computed tomography,

which provides three-dimensional images of a small rock fragment with a typical size of one to a few millimetres in each dimension. After image processing (noise reduction, smoothing, and segmentation), setting up the numerical experiment (object size and resolution as well as the boundary conditions), and numerically solving the field equations, macroscopic properties of rock sample with realistic microstructure information could be estimated (Andrä et al., 2013a).

Volume fractions and spatial distributions of different rock constituents can be potentially extracted from micro-CT images through the segmentation process (Schlüter, Sheppard, Brown, & Wildenschild, 2014). The most obvious method of segmentation is through setting global threshold values on the greyscale histogram of the whole micro-CT image. However, greyscale values of different minerals can often overlap due to the following reasons. First, the greyscale values of a mineral are distributed within a range, which may be larger than the difference between mean greyscale values of two minerals. Second, random noise, which is a common artefact in micro-CT images, makes the greyscale value of some small dotted parts inside a phase fall into the range of another mineral. Third, due to limited resolution, voxels on grain boundaries may include more than one phase, so that the effective greyscale value may fall into the greyscale range of another mineral. As a result, the segmentation of micro-CT images with global greyscale thresholds is not able to generate satisfactory multi-mineral labels (Iassonov, Gebrenegus, & Tuller, 2009).

In contrast to the global thresholding method, local adaptive methods can further account for the local variations of greyscale value. In a popular local adaptive method named watershed (Roerdink & Meijster, 2000), only zones with the most distinctive greyscale values are selected as markers with global thresholding method, leaving the more ambiguous areas undefined. Then, markers grow like water emerging until they meet at the zones with high greyscale gradient, then the whole image is segmented. However, with the complexity of natural rocks and the artefacts of micro-CT scanning, it is even challenging to select appropriate markers. Due to these limitations, micro-CT image analysis is often restricted to two-phase segmentation, lumping all the mineral phases into one solid phase. This simplification can induce significant systematic errors in the subsequent effective property estimation (Ahmed, Müller,

Liang, Tang, & Madadi, 2017; Ahmed, Müller, Madadi, & Calo, 2019; Andrä et al., 2013a; Saenger, Lebedev, et al., 2016; Shulakova et al., 2013).

Another common problem of DRP is a trade-off between the required representative sample size for the physical property and the maximum achievable resolution of micro-CT images (Bazaikin et al., 2017). Dvorkin, Derzhi, Diaz, and Fang (2011) and Murphy III, Roberts, Yale, and Winkler (1984) reported substantial spatial variation of porosity for mm- and cm sized samples from a relatively homogeneous interval. Dvorkin et al. (2011) suggested that the properties of a small sample used in imaging and computing do not have to match the properties of its cm-sized host and suggested finding a trend calculated from subsamples. Furthermore, limited resolution could only partially characterise microstructure of a rock sample, which can lead to significant discrepancy between numerical estimates of rock properties based on micro-CT images and laboratory data. To overcome this problem, Madonna, Almqvist, and Saenger (2012) suggested separating the solid rock component into two phases, a pressure-insensitive mineral phase, and a pressure-sensitive grain-contact phase to get a reasonable agreement between computational and laboratory velocities. The limitations of DRP will be investigated in Chapter 2 and the corresponding improvement measures will be introduced in Chapter 2 and 4.

Rock properties, especially elastic, can be strongly pressure dependent (Eberhart-Phillips, Han, & Zoback, 1989; Han, Nur, & Morgan, 1986; Zimmerman, 1990). However, micro-CT images, as the foundation of DRP, are mostly scanned under ambient pressure (Ahmed et al., 2017; Arns, Knackstedt, Pinczewski, & Garboczi, 2002; Shulakova et al., 2013). There are a few attempts to obtain medical CT and micro-CT images of rock at higher pressure. Kawakata, Cho, Yanagidani, and Shimada (1997) succeeded in observing faulting process in granite with medical CT images under confining pressure. Watanabe et al. (2011) scanned a fractured granite sample with medical CT at different confining pressures, and numerically simulated the corresponding fracture flow. Yu et al. (2019) scanned a fractured shale with micro-CT to investigate the fracture morphology changes under different confining pressures. Furthermore, a digital volume correction (DVC) method can be used on micro-CT images analysis to quantitatively describe the three-dimensional strain field inside the sample due to applied stress (Seyed Alizadeh, 2014). For example, Shi et al. (2021)

monitored local creep strain field and cracking process in claystone by DVC analysis on micro-CT images.

Compared with fractured rocks and unconsolidated sediments, studies of pressure effect on an intact sandstone micro-CT images is quite scarce. The deformation of intact sandstones under stress is much smaller, so its direct observation is very challenging. Saenger, Lebedev, et al. (2016) scanned a Bentheimer sandstone using micro-CT microscopy at confining pressures of 1MPa and 20MPa. The difference between the two sets of images (image size 400×400×400 voxel, voxel size length 2.4μm) cannot be distinguished visually from the greyscale images. Saenger, Lebedev, et al. (2016) also compared the simulated elastic properties and permeability from images scanned at different pressures. The computed values are quite similar while the laboratory measurements show a strong pressure dependency. Furthermore, the traditional quantification of the strain field using the DVC method cannot capture small strain in an intact sandstone caused by small (under 50 MPa) stress. The application of DVC on intact objects is limited for determining large internal strain for soft materials (Bar-Kochba, Toyjanova, Andrews, Kim, & Franck, 2015). In Chapter 3, the study to further push the boundary of pressure effect detection in micro-CT images will be presented.

Several recent studies suggest that multi-mineral segmentation can be automated using convolutional neural networks (CNN) (Karimpouli & Tahmasebi, 2019; Wang, Shabaninejad, Armstrong, & Mostaghimi, 2020). In any application of neural network, a critical part is “ground truth” or labeled data. In previous applications of CNN on micro-CT segmentation, significant efforts were devoted to prepare the labeled data. Karimpouli and Tahmasebi (2019) semi-manually segmented only 20 slices of micro-CT images of a sandstone, because the segmentation of each slice required a long time. Then, they augmented the manually segmented images with stochastic image generator algorithm. However, the generated images are very similar to the original ones with limited new mineral features included, which restricts the amount of information to be learnt by their CNN. Wang et al. (2020) scanned a mini-plug for micro-CT images and then selected the middle part of the image to create two surfaces. Then, they scanned one surface with Quantitative Evaluation of Minerals by SCANNing electron microscopy (QEMSCAN) to automatically generate a mineral

map. After that, this 2D QEMSCAN image was used to guide the multi-mineral segmentation of 3D micro-CT using a local adaptive segmentation method. The 3D labels offered more realistic varieties of mineral phases for training than stochastic images generated from 20 slices. However, this label inherited the segmentation errors from QEMSCAN and the local adaptive segmentation method. Moreover, these studies tested the prediction of the CNN models based on sub-images from the same dataset. Ideally, trained CNN models should show effectiveness and robustness on a separate dataset (creating the so-called blind test). In Chapter 5, an encouraging study in applying CNN in micro-CT image segmentation will be introduced.

In summary, a variety of theoretical rock physics models based on idealised microstructures have been developed to quantify the relationships between seismic properties and petrophysical properties. These models have a few parameters (such as pore aspect ratios, coordination numbers etc.), which are usually adjusted to measured velocities. At the same time, high resolution tomographic data is often available. Such data can provide detailed information about the rock structure, which can be used to directly calculate effective elastic properties using different numerical schemes. Thus, DRP could act as a great tool to study on the relationship between pore scale characteristics and effective elastic moduli and potentially indicate the validity of various rock physics models. However, it still requires significant effort in understanding and improving different processes of DRP. An investigation on how to handle these challenges is quite necessary.

1.2 Objectives

The general objective of this thesis is to first build and improve a digital rock physics workflow for estimation of elastic moduli based on micro-CT images of sandstones, and then use this workflow to help understand the relation between pore scale characteristics and macroscale effective elastic moduli. More specifically, this objective will be achieved in the following steps.

Objective 1. Evaluate the limitation of DRP in the estimation of effective moduli, such as sample size, resolution and segmentation, and investigate a possible solutions.

Successful examples of previous DRP for elastic moduli estimation are limited to samples with simple structure and mineralogy. The physical size of sample is often too small to present heterogeneities at a larger scale and the image resolution is insufficient to characterise the details of rocks. Also, the greyscale values of different minerals in micro-CT images are often similar, and previous attempts to segment them as separate phases are not very successful. To push the boundary of DRP, these issues should be carefully investigated and hopefully addressed.

Objective 2. Understand how pressure can change micro-CT images and the corresponding estimated elastic moduli.

Elastic properties of sandstones can be highly pressure dependent. However, the pressure-induced deformation of intact sandstones in micro-CT images are below the resolving power of conventional image analysis methods. Also, most digital rock physics studies of the elastic properties operate with micro-CT images acquired at ambient pressure. The pressure effect on high-resolution micro-CT images of sandstone sample and on elastic properties computed from these images should be investigated.

Objective 3. Use DRP as a tool to understand the grain contact stiffness of sandstones in different cementation and stress conditions.

Grain contact stiffness is the key factor in predicting effective elastic moduli in different cementation or stress conditions. However, the direct measurement of grain contact stiffness is not possible with any current method. By adjusting the grain contact stiffness in the DRP setup to match the computed elastic moduli and laboratory ultrasonic measurements, the stiffness of contact phase can be inverted. This inverted stiffness is a valuable information for understanding the cementation and stress effect on the grain contact.

Objective 4. Explore how deep learning can automate the segmentation process in the DRP workflow.

Convolutional neural networks (CNN) have been successfully applied to empower computers with the ability to derive meaningful information from images. Micro-CT images segmentation may involve significant manual effort and subjective parameter

adjustments. CNN may be tested to see the potential to automate the segmentation process and achieve consistent results.

1.3 Thesis outline and related publications

The outline of thesis will be as follows:

Chapter 2: A digital rock physics workflow will be built to numerically compute elastic properties with finite element method, using micro-CT images of Bentheimer sandstones. The effect of sample size and image resolution on the computed elastic properties will be evaluated. Furthermore, a novel segmentation workflow will be built to detect feldspar and clay minerals, despite their grayscale similarity to quartz in micro-CT images. The simulated results based on the segmented multi-mineral labels will be compared against core measurements.

Related publications:

Liang, J., Gurevich, B., Lebedev, M., Vialle, S., Yurikov, A., & Glubokovskikh, S. (2020). Elastic Moduli of Arenites From Microtomographic Images: A Practical Digital Rock Physics Workflow. *Journal of Geophysical Research: Solid Earth*, 125(10), e2020JB020422.

Chapter 3: I will perform a comprehensive analysis of the stress effect on micro-CT-images, using a reservoir sandstone sample with pronounced stress-sensitivity. A purpose-built X-ray-transparent pressure cell enables scanning micro-CT images at confining pressures of up to 36 MPa. An unbiased workflow will be designed to detect the overall rock deformation under different pressure. Elastic properties will be computed based on high-resolution micro-CT images of a sandstone sample scanned at different pressures.

Related publications:

Liang, J., Lebedev, M., Gurevich, B., Arns, C. H., Vialle, S., & Glubokovskikh, S. (2021). High-Precision Tracking of Sandstone Deformation From Micro-CT Images. *Journal of Geophysical Research: Solid Earth*, 126(9), e2021JB022283.

Chapter 4: I will reconstruct the contacts according to the morphology of grains using watershed separation algorithm. These approximated grain contacts can then be used as a uniform phase with lower moduli in the numerical computation. In this way, the

effect of unresolved soft pores is taken into account, so the computed moduli can be in a reasonable agreement with laboratory ultrasonic measurements. At the same time, the stiffness of contact phase can be inverted in this matching experiment.

Chapter 5: I will propose an automated workflow for the multi-mineral segmentation of micro-CT images using a convolutional neural network (CNN). The CNN model is trained using labels of two sets of images of Bentheimer sandstone. The training labels include pore, quartz, clay and feldspar phases, resulting from the segmentation workflow, which will be introduced in Chapter 2. The trained model is then used to segment a new set of images of the Bentheimer sandstone.

Chapter 6: The conclusion of this thesis will be presented and future work will be suggested.

1.4 Author's contributions

The work presented in this thesis is done with the support from scientists at Centre for Exploration Geophysics, Curtin University as well as collaborating with researchers at the University of New South Wales (UNSW) and The Commonwealth Scientific and Industrial Research Organisation (CSIRO). The building and optimisation of digital rock physics workflow was primarily done by myself with the guidance of my thesis committee. Micro-CT scanning was carried out by Prof. Maxim Lebedev. Ultrasonic measurements were performed by Prof. Maxim Lebedev and Dr. Alexey Yurikov. Nano-indentation was carried out by Dr. Stephanie Vialle. Some finite element computation was conducted by Prof. Christoph Arns from UNSW. Optical and electron based microscopy (TIMA) was prepared by Michael Verrall from CSIRO. The Nuclear Magnetic Resonance was done by Dr. Lionel Esteban from CSIRO. Since all the publications arising from this research are results of teamwork, I use “we” instead of “I” in the following chapters where appropriate.

1.5 List of publications related to the research project

The chapters of the thesis include the edited version of the following publications.

All copyright material, where necessary, has been reproduced with permission.

- Liang, J., Gurevich, B., Lebedev, M., Vialle, S., Yurikov, A., & Glubokovskikh, S. (2020). Elastic Moduli of Arenites From Microtomographic Images: A Practical

Digital Rock Physics Workflow. *Journal of Geophysical Research: Solid Earth*, 125(10), e2020JB020422.

- Liang, J., Lebedev, M., Gurevich, B., Arns, C. H., Vialle, S., & Glubokovskikh, S. (2021). High-Precision Tracking of Sandstone Deformation From Micro-CT Images. *Journal of Geophysical Research: Solid Earth*, 126(9), e2021JB022283.

Chapter 2 Digital rock physics workflow for elastic moduli estimation from micro-CT images of sandstones*

2.1 Introduction

Quantitative interpretation of reflection seismic measurements is often used to map the spatial distribution of petroleum reservoir properties in the subsurface. In this process, elastic properties of rocks are first derived from seismic data, and then used to estimate the reservoir properties. The relationship between elastic properties and reservoir characteristics is referred to as rock physics models (Mavko et al., 2009). These models are either derived analytically, as hybrid of theoretical, empirical and heuristic relationships, or based on empirical trends observed in laboratory measurements. Analytical models relies on idealised microstructures and simplify the physics of rock deformation. For example, rocks are often modelled as solid particles with isolated ellipsoidal inclusions (Eshelby, 1957; Zimmerman, 1990). The critical input parameters of these models for estimating the elastic properties are pore microstructure parameters, which are often derived from elastic properties. Therefore, rock physics diagnostics can become a poorly constrained model-fitting exercise. Empirical models rely on laboratory measurements of elastic properties (usually, ultrasonic velocities) that are then correlated with some bulk petrophysical parameters: porosity, clay content, etc. For sedimentary rocks, elastic properties are only partially controlled by bulk petrophysical properties. The key pore microstructure parameters, such as micro-cracks, may have a first-order effect of rock elasticity (Smith, Sayers, & Sondergeld, 2009), but this effect cannot be well understood from the empirical models.

Digital rock physics (DRP) aims to overcome this limitation (Ahmed et al., 2017; Ahmed et al., 2019; Andrä et al., 2013a, 2013b; Arns et al., 2002; Dvorkin et al., 2011; Makarynska, Gurevich, Ciz, Arns, & Knackstedt, 2008). In DRP, 3D geometry of the mineral and pore phases of a rock is imaged to digitise the sample into a dataset. Micro computed tomography (micro-CT) is the most popular method to acquire such pore-scale information, which is attained from the local x-ray absorption difference (Andrä

* This chapter is a modified version of the paper Liang, J., Gurevich, B., Lebedev, M., Vialle, S., Yurikov, A., & Glubokovskikh, S. (2020). Elastic Moduli of Arenites From Microtomographic Images: A Practical Digital Rock Physics Workflow. *Journal of Geophysical Research: Solid Earth*, 125(10), e2020JB020422.

et al., 2013a). Then, various physical processes can be simulated on this digital rock sample to quantify the corresponding effective rock properties (Andrä et al., 2013b). With the recent development of high-resolution 3D imaging technique and ever-growing computational resources, DRP has the potential to provide a comprehensive analysis of rock properties and to simulate various conditions and processes that would be time and cost demanding if they were to be performed in the laboratory.

In this chapter, we will focus on computing effective elastic moduli based on micro-CT images. The standard approach to compute effective elastic moduli is the Finite Element Method (FEM) (Ahmed et al., 2017; Ahmed et al., 2019; Arns et al., 2002; Shulakova et al., 2013), which solves partial differential equations (PDE) numerically. Displacement or stress is induced on the boundary of a sample to define the boundary conditions for the PDE, and the displacement and stress field inside the heterogeneous medium is computed by minimising the elastic energy. Then, the effective elastic moduli of the whole medium can be derived by averaging the computed physical field.

A major limitation of this technology is the fact that DRP predictions for the elastic moduli are systematically higher than the laboratory ultrasonic measurements (Andrä et al., 2013b; Saxena et al., 2019). First, current micro-CT images still lack resolution (voxel size of hundreds of nm at best) to characterise fine rock features: intergranular contacts, clay clusters etc. (Madonna et al., 2013). For instance, mercury porosimetry, which can measure pore throat diameters between 3nm and 14 μm , provides a long tail in the smaller pore throats part of the spectrum, which remains unresolved in micro-CT scans (Madonna et al., 2012). For most lithology types, the narrow compliant pores have significant effect on the elastic properties despite their small volumetric fraction. Secondly, there is a trade-off between resolution and the image volume. The number of voxels in micro-CT scans is usually 2000^3 or fewer, and hence digital samples with $0.5\mu\text{m}$ voxel size are around 1mm^3 , which is usually insufficient to adequately represent the laboratory sample, let alone larger rock volumes (Bazaikin et al., 2017; Saxena et al., 2019; Wollner, Kerimov, & Mavko, 2018). Thirdly, DRP modelling requires moduli of each mineral component. These moduli are often uncertain, because (1) some minerals do not form a sufficient volume to be measured (e.g. clay minerals) and (2) chemical composition and crystal structure of some minerals, such as feldspar, are variable (W. L. Brown, 2013; Mondol, Jahren,

Bjørlykke, & Brevik, 2008). Furthermore, computer simulations of rocks deformation require segmented images, where each voxel is attributed to a particular mineral or pore space. This segmentation process is uncertain because the grayscale values of different mineral are not clearly separated and grain boundaries are smeared as a result of the limited imaging resolution (Saxena et al., 2017).

Due to the complexity of the problem, methodological studies are often limited to the simplest porous materials, such as Fontainebleau sandstone, oolites or sintered glass (Arns et al., 2002; Kalo et al., 2017; Knackstedt et al., 2009). The standard techniques tested on these materials require verification and often modification when applied to more complex rocks. This chapter proposes a practical DRP workflow for somewhat more complex and ubiquitous rocks, namely, sandstones that contain mostly quartz and a small fraction of dispersed clay (known as arenites) (Vernik, 2016).

Our study relies on a set of micro-CT images of Bentheimer sandstones accompanied by ultrasonic measurements on the samples from the same block. Rock images are acquired under a variety of settings, so we can address the effects of image sizes and resolution on the computed effective moduli. In particular, we segment clay and feldspar as separate phases instead of treating all the solid material as one “mineral phase”. Thus, we can evaluate the effect of the minerals other than quartz on the computed moduli. Based on extensive tests, we establish an optimal image segmentation graph and a set of post-processing corrections for the computed moduli of the Bentheimer sandstone samples. To compare the computation results against laboratory measurements, we divide the digital samples into subsamples to reconstruct the porosity-moduli trends and compare this trend against laboratory measurements (Dvorkin et al., 2011). We find that the computed moduli are consistent with the laboratory measurements at higher pressure. We believe that the proposed DRP workflow should be directly applicable to rocks with similar lithology, and the approach to workflow optimisation can be extended to a wider range of rock types.

2.2 The laboratory data set

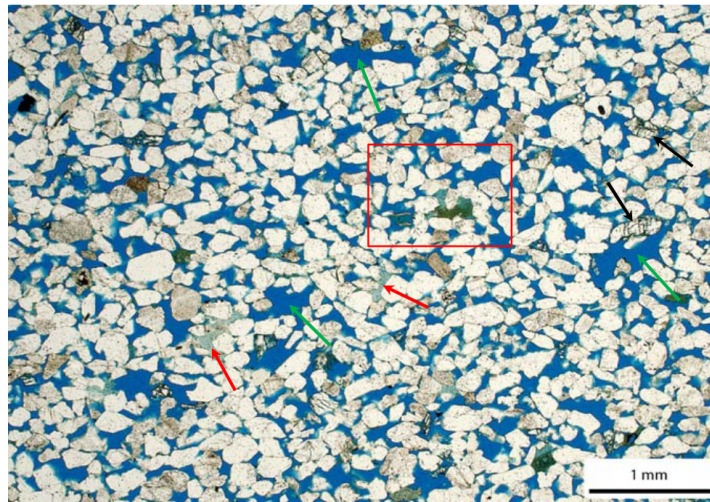
Bentheimer is an outcrop sandstone, which occurs in two varieties: clay- and iron-rich red type and clean pale yellow type (Peksa, Wolf, & Zitha, 2015). The analysis of thin section (Figure 2.1) shows that our samples belong to the pale class with mainly quartz (>90% of the matrix) with accessory feldspar, kaolinite and other minor rock

fragments, which is a typical kind of arenite. The moldic porosity most likely originates from dissolved feldspar grains, although some clay particles may also have been removed from large pores. Matrix and intergranular pores contain minor amounts of clay minerals and moderate quartz overgrowth. The microstructure is typical for relatively shallow hydrocarbon reservoirs that have not undergone extensive burial history, except for the fact that some of the clay did not form in-situ but inherited while the sample was exposed in an outcrop.

Cylindrical (38.5 mm in diameter, 70.0 mm length) samples for laboratory ultrasonic measurements are visually indistinguishable from one another, and have been extracted from the same sandstone block right next to each other to guarantee similar porosity and texture. Samples were frequently sprinkled with water while being cored for cooling. Then, samples were put into a drying chamber at 50°C for 24h. Velocities were measured at ultrasonic frequencies (1MHz) inside a pressure cell at a range of hydrostatic pressures from 4MPa to 50MPa and back to 4MPa. Pressure-dependency curves showed only a negligible difference between loading and unloading cycles and are very similar for all the three samples (Figure 2.2). Since the measured parameters are almost identical for the selected samples, they collide into a single calibration point for standard rock physics modelling that involves no detailed petrographical information. The data set may therefore highlight the importance of information that can be extracted from a careful DRP study.

Cylindrical (5 mm diameter, 20 mm length) samples for micro-CT imaging are extracted from the same sandstone block as for ultrasonic measurements. For this study, four sets of micro-CT images of Bentheimer sandstone were acquired with the Versa XRM-500 (XRadia-Zeiss) X-ray microscope at various resolutions and sizes (Table 2.1). This apparatus can provide a scanning voxel of less than 1 μm , and the maximum size of the sample is 2000 voxels in each dimension, which needs to be reduced by about 30% when the cylindrical scan is cut into cubic computational domain.

(a)



(b)

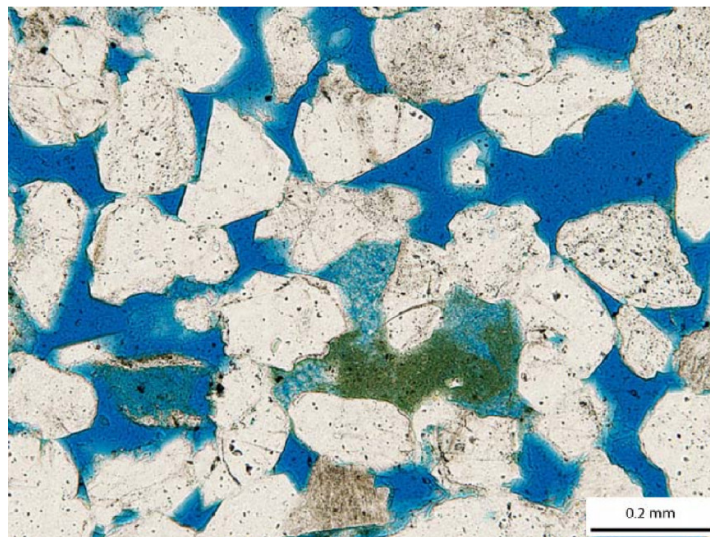


Figure 2.1 Thin section of Bentheimer sandstone. (a) The sample is lower-medium-grained well-sorted sandstone. The grains are predominantly monocrystalline quartz, with potassium feldspar (black arrow) and other rock fragments. Authigenic minerals include minor amounts of clay minerals (red arrow) and moderate quartz overgrowths. Intergranular pores (blue) are abundant, but the largest blue spaces are grain-moldic dissolution pores (green arrows). The location of the high-magnification image (image b) is outlined with a red rectangle within the low-magnification image. Thin section preparation and analysis was conducted by Core Laboratories.

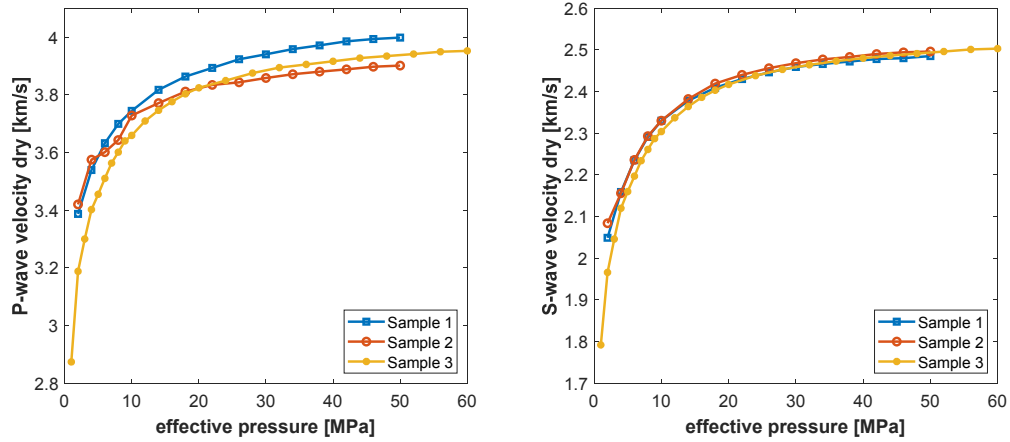


Figure 2.2 Pressure dependent ultrasonic velocities of three Bentheimer sandstone samples at dry conditions. Samples are dried in a vacuum at 50°C for 24h. The effective pressure is varied by changing confining pressure.

Table 2.1 Bentheimer sandstone micro-CT images

Image Name	Voxel size (μm)	Voxel
A-1	1.5854	972×1012×1007
A-2	3.3452	988×1012×1007
B-1	2.1137	988×1012×992
B-2	3.4348	988×1012×992
C-1	0.9814	988×1012×992
C-2	3.4348	988×1012×999
C-3	4.7003	988×1012×998
D-1	1.0009	988×1012×992
D-2	2.0002	984×1012×996
D-3	4.0009	988×1012×1000

2.3 Scanning effects evaluation

First, we analyse the effects of the image sizes and resolution on the computed effective moduli. Theoretically, a DRP study require a Representative Volume Element (RVE) to make the computed results consistent with measurements at larger scales. A RVE should be large enough to satisfy the following two criteria:

- Sampling criterion: the fractions of pores, cracks and grains are the same as in the laboratory sample;

- Physical criterion: the computed moduli are independent of boundary conditions, that is, the parts near the boundary are small compared to the whole sample volume.

2.3.1 Numerical simulations

Here and below, we define a numerical simulator as a suite of algorithms required to model elastic deformations of a segmented micro-CT image – regular 3D grid where each voxel is indexed according to the material it belongs to: pore space or a particular mineral. Essentially, the simulator is defined by the approach to solution of two inter-dependent problems: discretization of the image’s geometry – meshing, and numerical solution of the differential equations that govern the physical field. Several studies reviewed existing approaches to these problems (Andrä et al., 2013b; Cotton, Tompsett, Smigaj, Kerim, & Agarwal, 2016; Saxena et al., 2019) and concluded that a numerical solver has relatively small effect on computed moduli and cannot explain their discrepancy from measured moduli. Hence, our choice of the computational framework is driven by practical considerations: robustness of the computations and sensitivity to user input, such as meshing parameters and post-processing of the results.

For the computations, we implemented FEM approach of Garboczi (1998) in COMSOL (v. 5.4.) to get direct access to the rich toolbox of pre- and post-processing algorithms and solvers in this software (Figure 2.3). The framework of Garboczi is widely used in DRP, because it treats each voxel of an image as a cubic computational grid cell. Some other workflows aim to recover the smooth surface between grains and pores, and then mesh the reconstructed geometry using tetrahedral elements (Ahmed et al., 2017; Shulakova et al., 2013). However, due to complicated microstructure of natural rocks, the reconstructed surface process may produce a less accurate representation of the real geometry (Antiga, Ene-Iordache, Caverni, Cornalba, & Remuzzi, 2002; Cebal & Löhner, 2001). Therefore, a voxel-based approach such as Garboczi code is more popular in practical applications.

An important component of the numerical simulator are the boundary conditions, because the physical RVE criterion is almost never fulfilled and hence the behaviour imposed at the boundaries will affect the computed moduli. Regardless of the numerical implementation, kinematic (fixed displacements) and dynamic (fixed surface tractions) boundary conditions on the surface of the computational domain

provide the upper and lower bounds on the effective rock moduli, respectively (Huet, 1990). The moduli computed with periodic boundary conditions always lie between the bounds computed from the kinematic and dynamic boundary conditions and are less scattered around the mean values when samples are small (Kanit, Forest, Galliet, Mounoury, & Jeulin, 2003). The periodic boundary conditions enforce the strain to be relatively uniform through the digital sample, while the value of strain is determined in a self-consistent manner during computations.

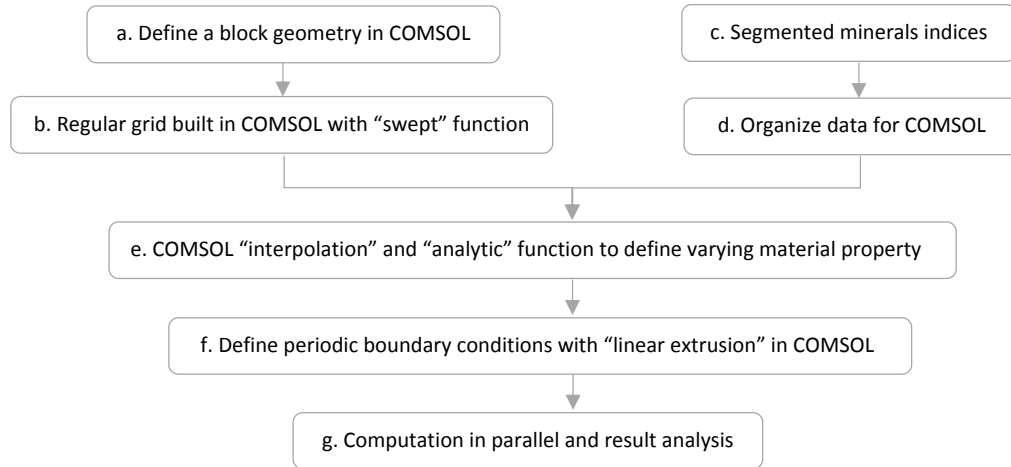


Figure 2.3 Digital rock workflow implemented in COMSOL.

The numerical simulations require significant computational resources, especially in terms of RAM. Due to an internal limitation of COMSOL, we limit the models to 600^3 cells, which already require 4TB RAM. The computations are run on a research cluster at the Curtin Centre for Exploration Geophysics and Pawsey Supercomputing Centre. The first cluster has 16 virtual nodes with a total of 368 Intel Xeon Gold 5120 CPUs and 5TB RAM, and the second includes six nodes, each with 16 “Broadwell” Intel Xeon CPUs and 1T RAM. Depending on the purpose for the specific simulation and availability of the cluster, the computational times are shown in Table 2.2.

Table 2.2 Computational resource requirement for samples of difference sizes and computation efficiency.

Sample voxel number	Node number	CPU number of each node	RAM of each node (GB)	Computation time (hour)
600^3	4	16	1024	~18
500^3	4	16	1024	~10
300^3	6	28	256	~1

The simulation workflow will remain the same for the subsequent analysis of this Chapter. One may see it as a pre-defined image processing procedure that converts the segmented micro-CT images into estimates of the moduli. Therefore, the user controls only two internal parameters of this conversion: dimensions of the computational domain and the grid cell size. This approach allows us to explore how the match between the measurements and DRP results depends on the image processing and post-processing of the computations.

There is always a trade-off between sample size and resolution, because any increase in the scanned volume would result in a lower resolution. However, we may compensate for the size/resolution effects using statistical analysis of a suite of images and computations as shown below.

2.3.2 Scanning parameters and resolution-size trade-off

To investigate the size effect of the computational domain, we use images with the largest physical dimensions, and hence, the coarsest resolution. To further reduce the computational cost, the greyscale images are down-sampled with Lanczos method (Madhukar & Narendra, 2013) from 680^3 voxel to 500^3 . We first analyse only binary segmentation into dry pores and solid quartz using Otsu method (Otsu, 1979), as implemented in AVIZO (2019.3). Figure 2.4 shows the computed moduli for the samples that grow outwards from the same centres. The moduli seem to stabilise as the sample gets larger. Once the edge length reaches $\sim 1.25\text{mm}$, the moduli remain almost constant. However, the computed moduli of four samples still do not converge even they are extracted from the same sandstone block. It indicates that the theoretical Sampling RVE cannot be fulfilled in our DRP study even with relatively homogeneous sandstone samples and large scanning resolution. Thus, we cannot assume that the mm scale DRP sample statistically contains the same microstructure and mineral information as the cm scale ultrasonic sample. A promising solution is to divide the image set of DRP study further into subsamples and compare the trend of computed moduli from subsamples with the ultrasonic measurements (Dvorkin et al., 2011).

Next, we investigate the effect associated with the Physical RVE criterion. Fluctuations of the stress/strain prescribed at the boundary are controlled by the size of heterogeneities and hence characteristic thickness of the boundary layer is the same for samples of the same material. However, the volume fraction of the boundary layer

increases for smaller samples, and thus causes size-dependence of the computed moduli. As a result, computed moduli of subsamples will in general be scattered around the moduli of the largest sample with biased mean value. Figure 2.5 shows computed moduli for four full-size samples and their subsamples with a half and quarter of the original edge length. The variability of moduli increases significantly as the edge gets smaller. We describe the relationship between the mean computed moduli and edge length using an exponential fit $A \exp(-L/B) + C$, where A controls the magnitude of the size dependence, B the characteristic size of the computational domain where the effect of boundary conditions vanishes and C the estimated effective modulus (see equations in Figure 2.5 and Table 2.3). The regressions show the same trend: the mean values of moduli computed on smaller subsamples are systematically higher. Even at $\sim 1.25\text{mm}$ edge length, where the local computed moduli stabilise, the mean computed moduli are higher than the true one. In the following sections, we use the exponential relationship between computed moduli and edge length to correct computed moduli to their asymptotic limits.

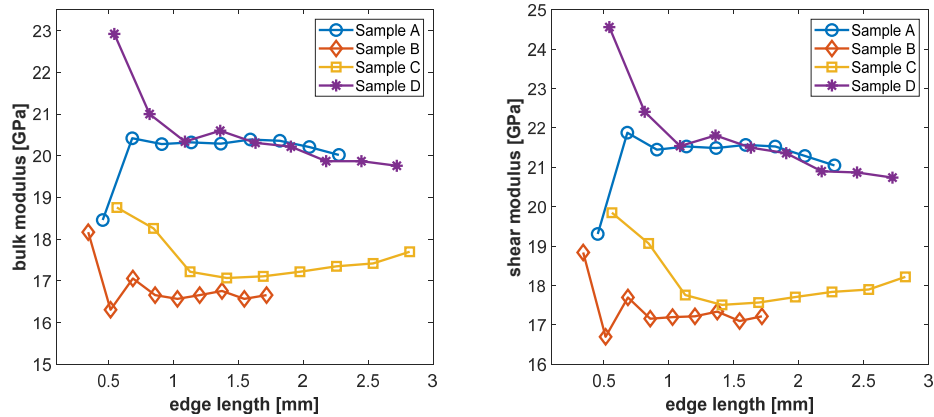


Figure 2.4 Computed moduli change as the edge length grows. Variability of computed moduli decrease, and the values of each single sample relatively stabilise from 1.25mm edge length, but the difference among four samples remain.

Finally, we need to consider the effect of resolution. Although micro-CT may not accurately image the grain contacts in Bentheimer sandstone, $1\mu\text{m}$ voxel size carries much more information about the microstructure of sample D than $4\mu\text{m}$ voxels (Figure 2.6). Arns et al. (2002) proposed a simple method to compensate the resolution effect on computed moduli. They found a linear relationship between the computed moduli and voxel size ($y = kx + b$, where x is voxel size and y is computed moduli; k and b

are coefficients defining the linear relationship). The coarser mesh was obtained by artificially resampling original images. We have however found that the trends estimated from resampled images deviate from the trends for scans that were physically acquired at different resolutions (Figure 2.7). We will use the trend observed in all four samples as a heuristic correction to bring the computed moduli to a reference resolution of $1\mu\text{m}$. The extrapolation would not have been necessary, were the computational facilities capable of handling models of 2000^3 voxels.

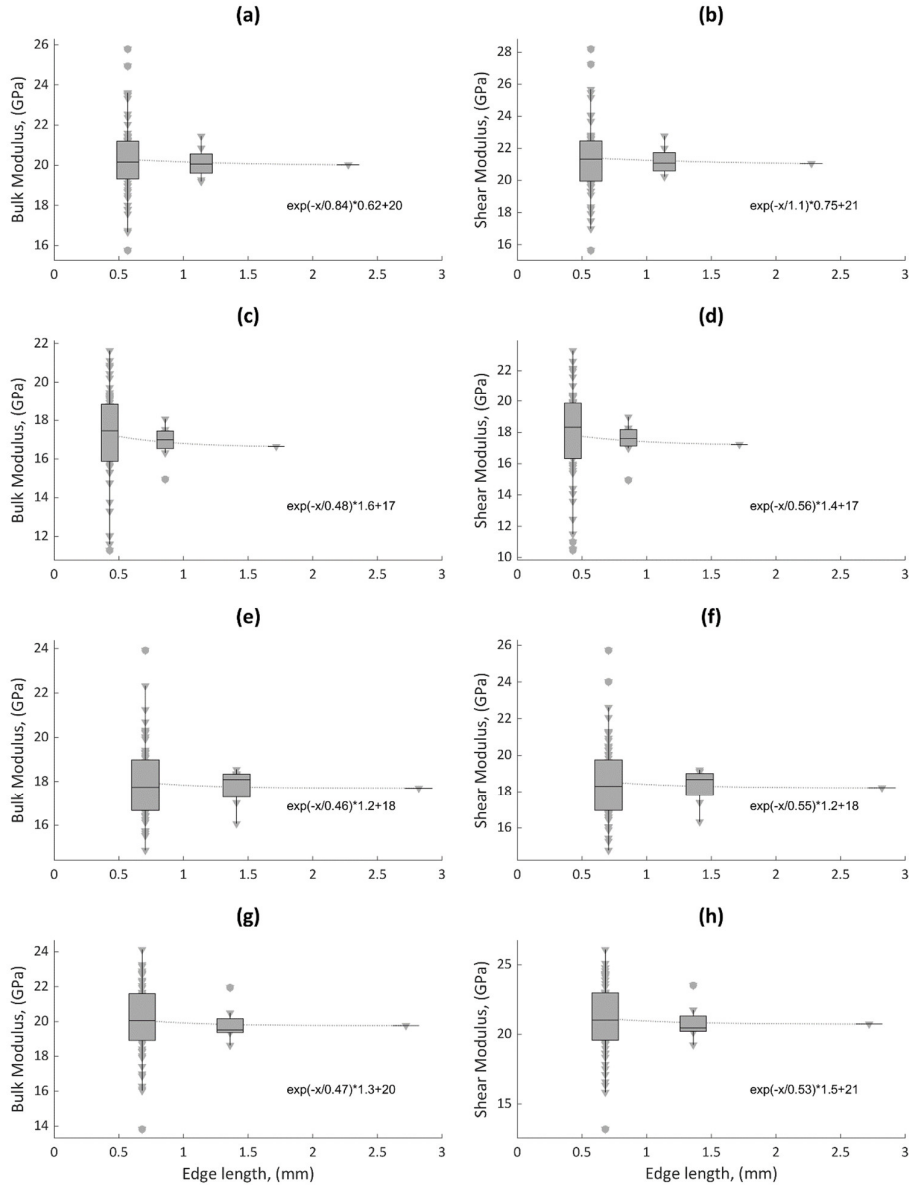


Figure 2.5 Boundary condition effect on the computed moduli. In each row, bulk and shear moduli computed from each of our four samples and the corresponding subsamples with half and a quarter of original edge length are plotted. The variability

of moduli increases significantly while the edge length decreases as the box plot shows. Assuming the relationship between mean moduli and edge length is exponential, we derive the asymptotic moduli for each sample.

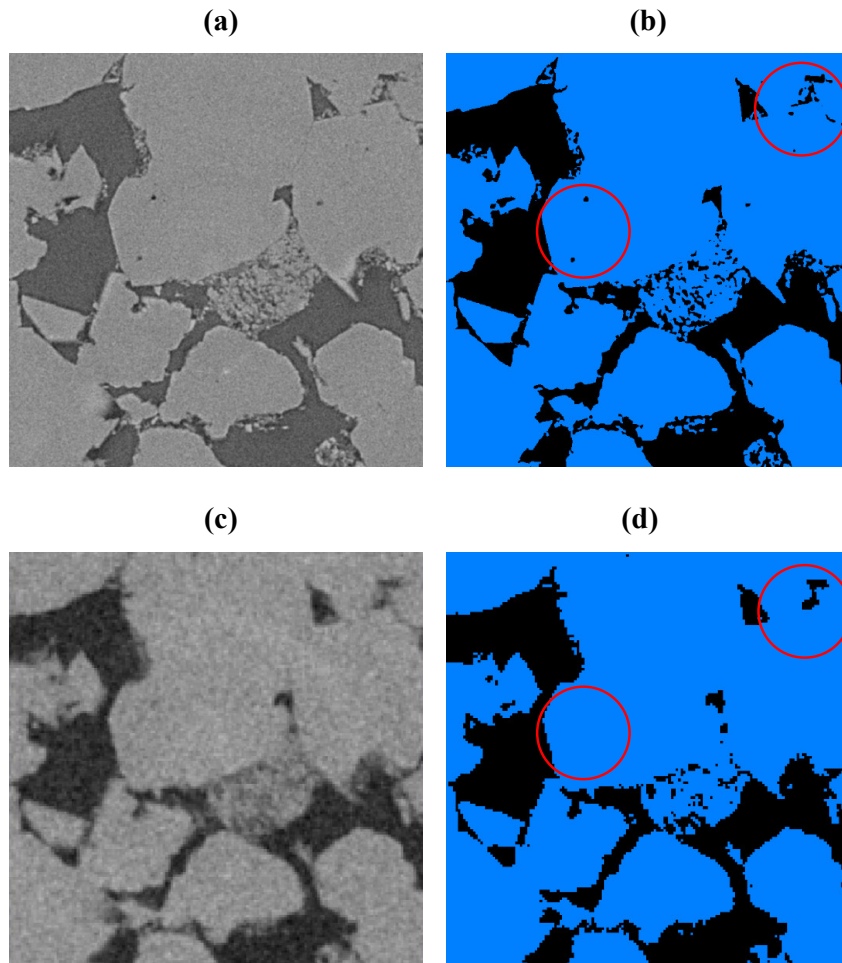


Figure 2.6 Resolution effect on greyscale and segmented images. (a) Sample D greyscale image (voxel size $1\mu\text{m}$), (b) Sample D segmented image (voxel size $1\mu\text{m}$), (c) Sample D greyscale image (voxel size $4\mu\text{m}$), (d) Sample D segmented image (voxel size $4\mu\text{m}$).

Based on the tests above, we have several key findings related to limitations of microtomography and computational facilities in the present study. For Bentheimer sandstone, we conclude that the images with the largest edge length still cannot satisfy the theoretical RVE requirement. The deviation effect of the boundary conditions exists and can be corrected using an exponential relationship between computed moduli and sample edge length. As for the resolution effect, a linear relationship between computed moduli and voxel size can remove the extra stiffness of low-resolution samples. Quantitatively, the correction for the boundary condition effects

reduces the computed moduli by 0.45%-0.7% for samples with 1.25mm edge length and by 1.45%-2.59% for samples with 0.625mm edge length (Table 2.3). The resolution effect can cause up to 10% reduction of the computed stiffness (Figure 2.7).

Table 2.3 The deviation of computed bulk modulus (GPa) in absolute value and percentage due to boundary effect.

	A	B	C	D
asymptotic	19.98 / 0.00%	16.60 / 0.00%	17.70 / 0.00%	19.76 / 0.00%
1.25 mm	20.12 / 0.70%	16.71 / 0.66%	17.78 / 0.45%	19.85 / 0.46%
0.625 mm	20.27 / 1.45%	17.03 / 2.59%	18.01 / 1.75%	20.11 / 1.77%

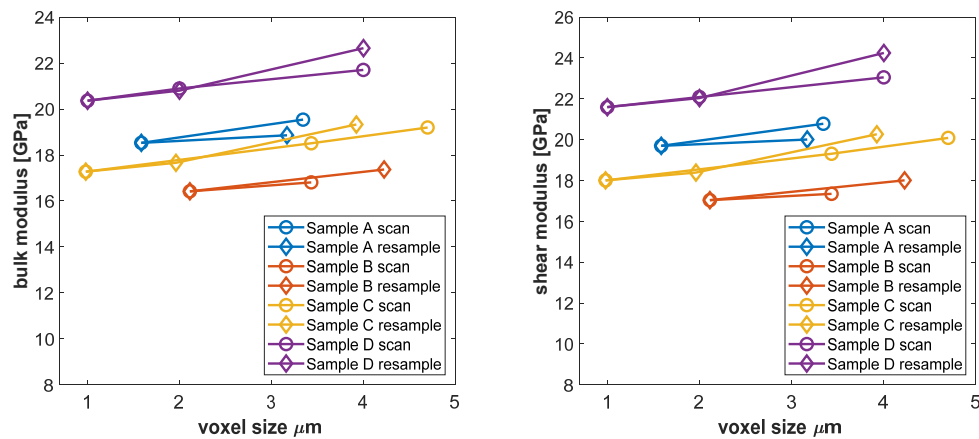


Figure 2.7 The relationship between computed moduli and voxel size. The computed moduli based on images scanned with different voxel size and manually resampled images from one high resolution image are compared.

Among the images available in our study, the proposed corrections may be directly applied to image pairs B-1, B-2 and D-2, D-3 (Table 2.1). They are sufficiently large to minimise the moduli variability associated with the mentioned RVE issues. Also, two resolutions can define a linear trend to extrapolate the moduli to higher resolution.

2.4 Specialised image processing for arenites

The previous section treated an arenite sample as a two-phase medium – solid minerals had the moduli of quartz and pores zero moduli. Most digital rock physics studies lump all solid material into the same “mineral phase” (Andrä et al., 2013a; Shulakova et al., 2013). It is however well-known that the effective moduli of sandstones vary significantly with properties and spatial distribution of clay (Dræge et al., 2006; Sams & Andrea, 2001). Hence the clay (mainly kaolinite) may have first-order effect on the

stiffness of the Bentheimer sandstone samples of this study. To incorporate the clay phase, we design a detailed workflow for image processing, which is implemented using AVIZO software.

2.4.1 Suppression of random noise

The original micro-CT images are contaminated with random noise, which is caused by instrumentation noise and variability of the conditions inside the tomography instrument. Most the random noise suppression approaches involve comparison of a voxel intensity against average intensity in its vicinity. Such procedures tend to blur the images, so we use a *non-local means filter* (Buades, Coll, & Morel, 2005) with parameters as mild as possible to reduce the blurring (Figure 2.8). Our goal is to reduce the noise level so that a segmentation algorithm may detect pores and solid phase accurately. After extensive tests, we conclude that *unsharp masking* recovers most of the small pores and cracks from the blurred images (Figure 2.8) by enhancing the high frequency content of the images (Sheppard, Sok, & Averdunk, 2004).

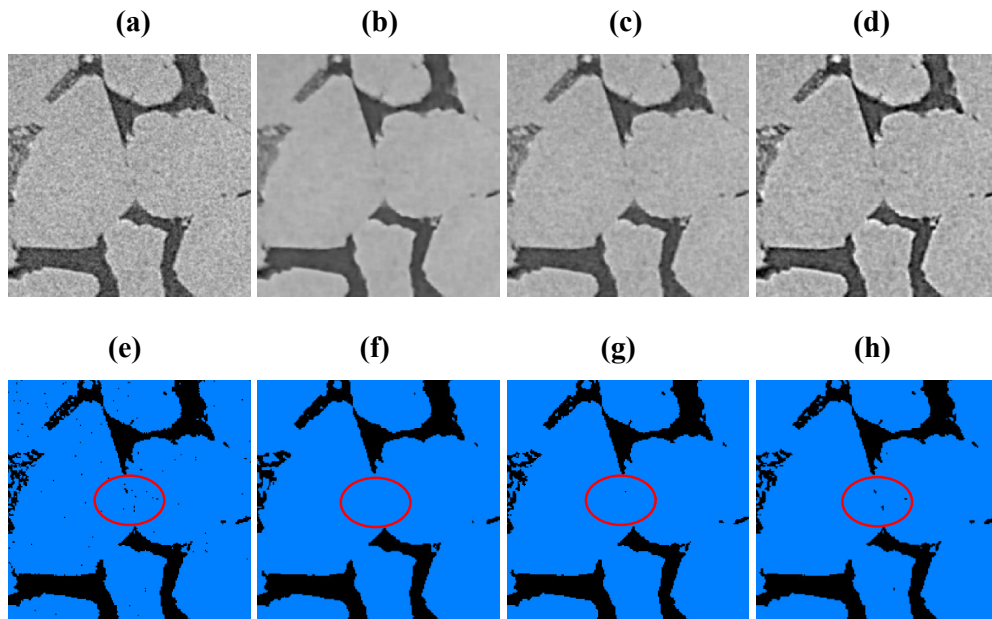


Figure 2.8 Image processing effects on greyscale and segmented images. (a) Part of original CT image D-2, (b) after *non-local means filter* with strong parameters from (a), (c) after *non-local means filter* with mild parameters from (a), (d) *unsharp masking* from (c). (e) – (h) are segmented images from the corresponding greyscale images above.

2.4.2 Standard techniques for multi-mineral segmentation

Although feldspar and clay particles can be identified visually (Figure 2.9a), their automatic segmentation is challenging, since the histogram of voxels intensity indicates only two phases - solid and pore (Figure 2.9b). Figure 2.10a shows the result of three-phase segmentation using global thresholds in *Otsu* segmentation (*Otsu, 1979*). This approach fails due to the overlapping greyscale for feldspar, random noise, instrumentation ringing (*Sijbers & Postnov, 2004*) and grain boundaries. Figure 2.10b shows the output of *watershed* segmentation for the same image (*Roerdink & Meijster, 2000*). Compared with *Otsu*, *watershed* is less sensitive to the local noise, but tends to ignore small features (red ellipse in Figure 2.10c). Also, the X-ray intensity of quartz grains gets closer to feldspar because of the proximity to air-filled pores (*Joseph & Spital, 1981*), hence the boundaries are misclassified as a feldspar. Both *Otsu* and *watershed* fail to accurately detect clay in the solid phase.

With these unsatisfactory segmentation results, most studies resort to two-phase *Otsu* segmentation, which is more robust and hence produces less unphysical features. The simplification of various minerals with a single solid phase will certainly bring about systematic errors. Here, we propose a more advanced segmentation workflow implemented in AVIZO. Then, Bentheimer sandstone greyscale images can be accurately segment into four-phase labels (quartz, pore, clay and feldspar).

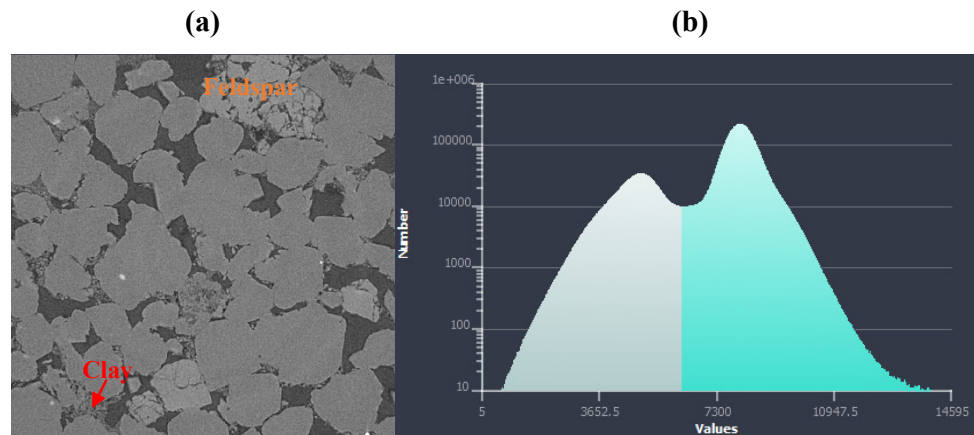


Figure 2.9 Micro-CT image of D-2 and the greyscale histogram.

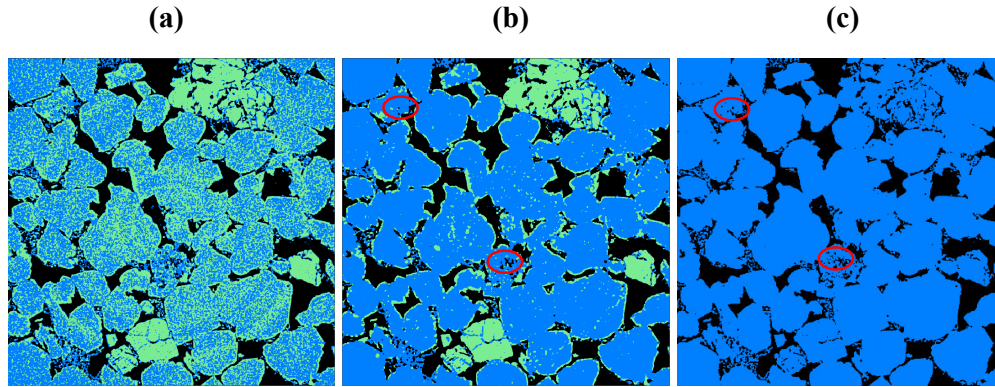


Figure 2.10 Greyscale images segmented into three phases using Otsu (a) and watershed (b) method, segmented into two phases with Otsu method (c).

2.4.3 Four-phase multi-mineral segmentation: clay segmentation

The workflow for clay segmentation takes advantage of both pixel intensity and morphology of clay particles.

- *Median filter* is used to suppress random noise.
Intensities of the solid constituents become distinguishable in the blurred image. The clay phase, which formed fluffy clusters in the original images, now shows as homogeneous light-grey regions due to stacking of the micro pores and particles (Figure 2.11).
- Three-phase *Otsu* algorithm to segment the filtered images.
Segmentation attributes each voxel to the following three groups: pores, quartz and feldspar, clay and grain boundaries (Figure 2.12a). Then, we extract the phase including clay with *arithmetic* function in AVIZO (Figure 2.12b).
- *Opening* algorithm (Haralick, Sternberg, & Zhuang, 1987) removes the high-intensity lines at grain boundaries.
The algorithm consists of a sequential *erosion* and *dilation* operations with disc as a matching template, which first highlight the thin shell-like artefacts and then remove them (Figure 2.12c). Eventually, the third solid phase includes almost exclusively clay.
- Segmented clay region as a mask for unsmoothed two-phase segmented images.
The *mask* module in AVIZO is applied on unsmoothed two-phase segmented images (Figure 2.10c) using segmented clay region to retrieve back the clay particles and micro pores (Figure 2.12d). Then the recovered clay particles are

combined with unsmoothed two-phase segmented images to achieve the three phase segmented labels (Figure 2.12e). At this stage, the segmented images contain clay phase, pores and combination of the quartz/feldspar grains.

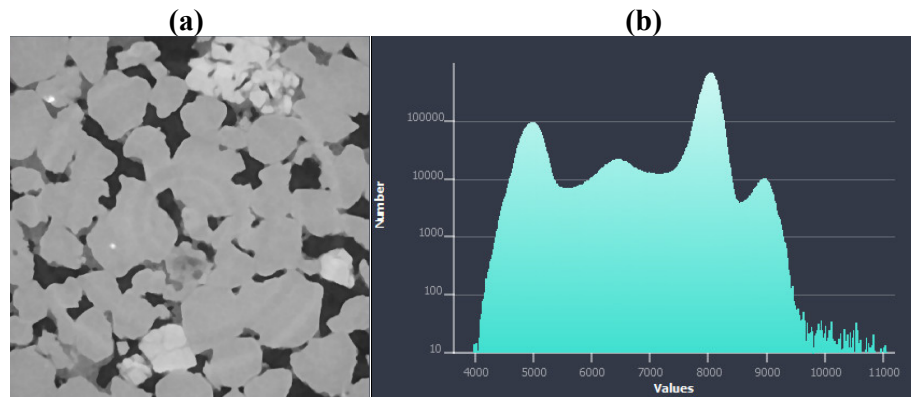


Figure 2.11 Grayscale image blurred with median filter (a) and histogram (b).

2.4.4 Four-phase multi-mineral segmentation: feldspar segmentation

We have seen that quartz and feldspar may not be discriminated by the voxel intensity. Straightforward application of *watershed segmentation* fails too (see Figure 2.10b). The fundamental reason for the latter failure is inappropriate initial seeding for the segmentation (Vincent & Soille, 1991). A refined workflow for preparation of the initial seeds include the following:

- Select the *feldspar* phase from figure 2.10b according to the phase index. Feldspar phase is mixed with random noise and grain boundaries (Figure 2.13a).
- Apply *closing* algorithm to remove intragranular voids by sequential *dilation* and *erosion* operations (Haralick et al., 1987) (Figure 2.13b).
- Use *erosion* function to remove the noise and edge artefacts (Haralick et al., 1987). The resulting patches become initial seeds for *watershed segmentation* (Figure 2.13c).
- Apply *watershed segmentation* again with the seeds obtained at the previous step (Figure 2.13d). The segmented feldspar phase becomes a mask for the output shown in Figure 2.10c. This retrieves back the intra-granular pores (Figure 2.13e).
- Combine the segmented feldspar with three-phase labels from Figure 2.12e to get the final four-phase segmented label (Figure 2.13f).

The whole segmentation process is summarised as a flowchart in Figure 2.14.

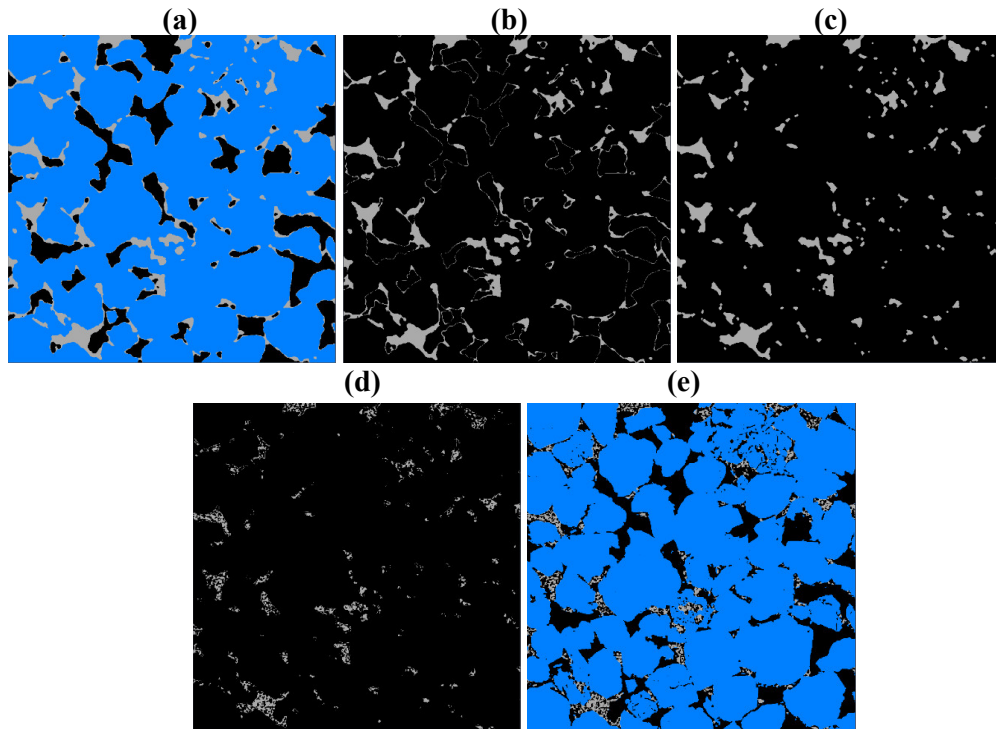


Figure 2.12 Three-phase segmented image with *Otsu* method (a), extracted clay phase (b), further apply *Opening* algorithm to eliminate the partial volume effect on grain boundaries (c), use clay phase as mask to extract clay particles from the unsmoothed two-phase segmented label (d) and final three-phase segmented label (e).

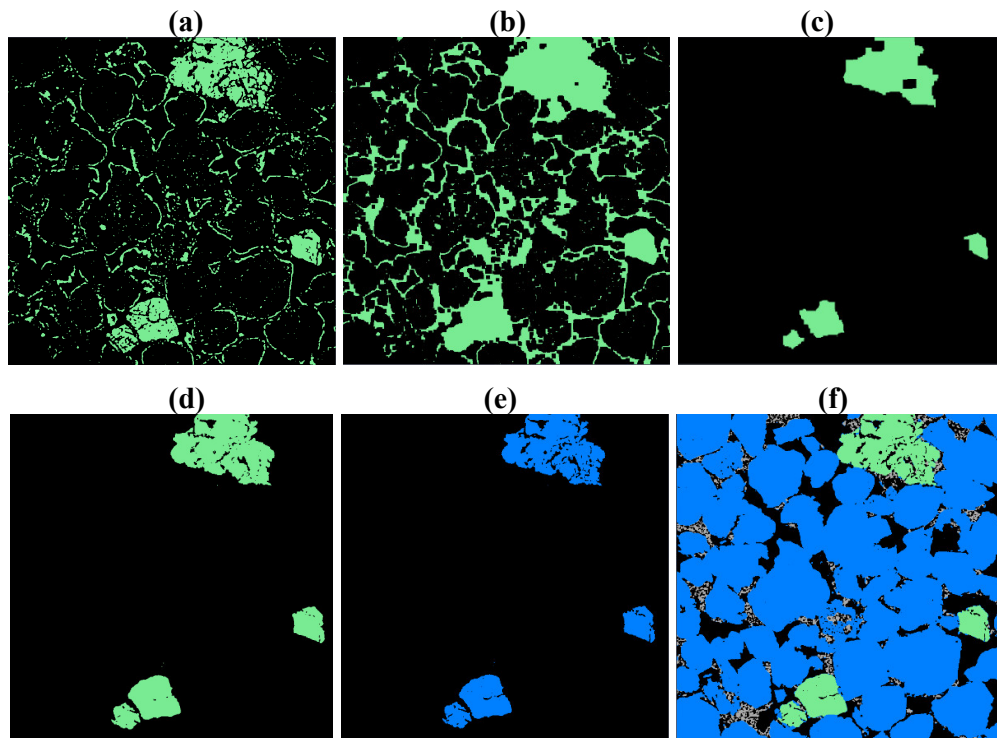


Figure 2.13 Extracted feldspar phase is mixed with random noise and grain boundaries (a), after *Closing* operation, feldspar grain becomes more connected (b), with *Erosion* operation, the noise and boundaries artefacts are removed (c), with (c) as watershed seeds, feldspar can be better segmented (d), segmented feldspar acts as Mask for Figure 9c to recover the micro cracks (e) and final segmented four-phase label (f).

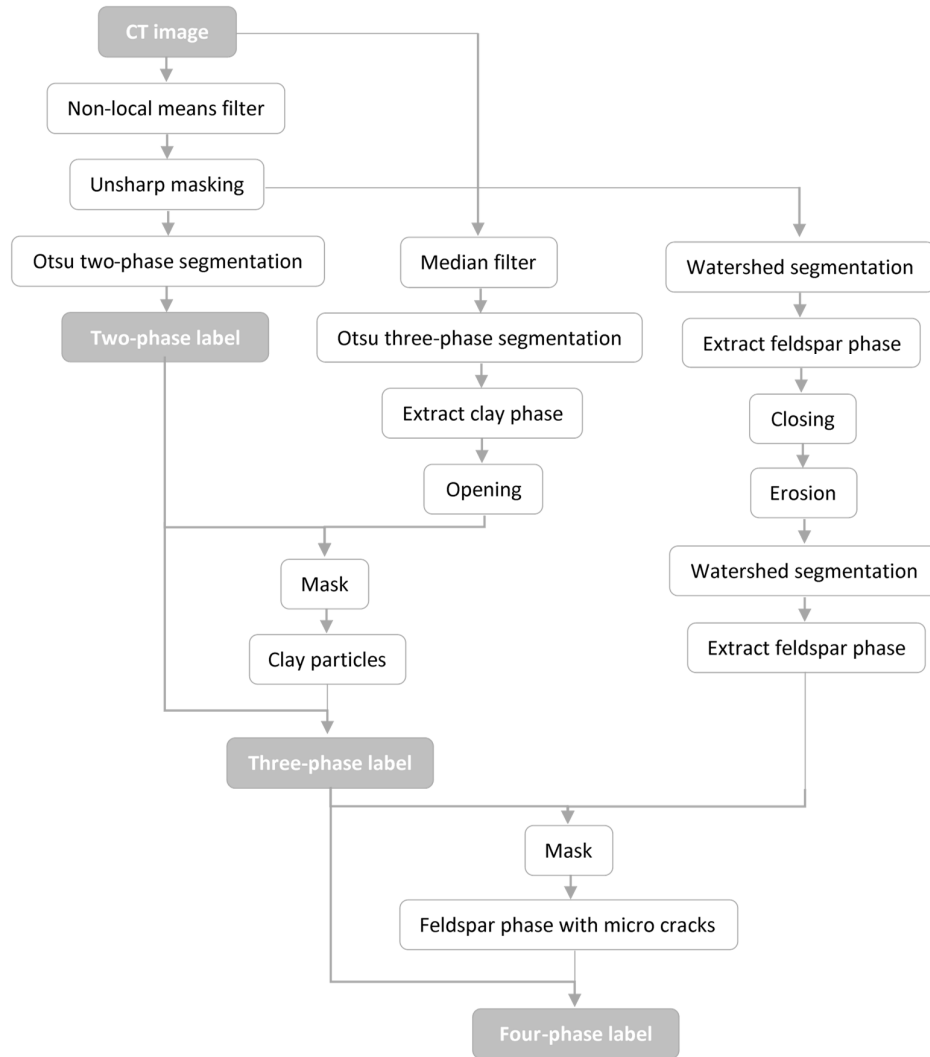


Figure 2.14 Optimised segmentation workflow for Bentheimer sandstone.

2.5 Effective moduli computation with reduced mineral moduli

Finally, we implement the full DRP workflow: multi-mineral segmentation followed by corrections for the sample size and grid cell size. We assess the accuracy of the predicted moduli by comparison with the moduli-porosity trends obtained at 40MPa from the laboratory measurements on Bentheimer sandstones and from literature data (Han et al., 1986). We only analyse the measurements in the range of relatively high

confining pressure or effective pressure (40MPa), which increases the stiffness of intergranular contacts by closing the voids between the contacting grains (Glubokovskikh, Gurevich, Lebedev, & Mikhaltsevitch, 2015) and suppressing the sorption-induced deformations (Yurikov, Lebedev, Gor, & Gurevich, 2018).

2.5.1 Multi-mineral matrix

First, we divide the samples B-2 and D-3 into eight subsamples, compute the elastic moduli, and compensate for the boundary effect using the corresponding equation in Figure 2.5. Figure 2.15 shows that even for sample B-2 with 0.6% clay and 1.69% feldspar, the four-phase segmentation results in ~5% difference from the two-phase segmentation. For sample D-3 with 2.16% clay and 2.19% feldspar, the average difference reaches 12%. Yet, the computed moduli still overestimate the measurements. Yet, the computed moduli still overestimate the measurements.

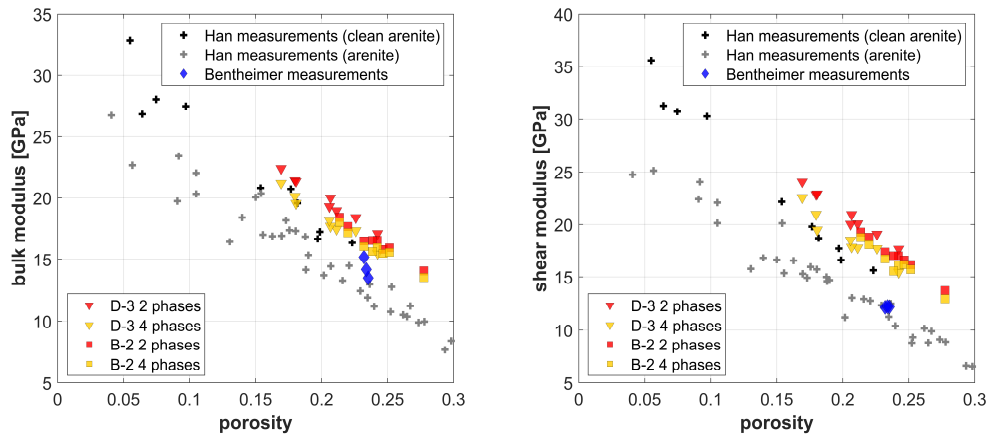


Figure 2.15 Computed moduli with different segmentation methods versus measurements. Red and yellow marks stand for the moduli computed from two- and four-phase images respectively. The triangle marks stand for the subsamples of image B-2. The square marks stand for subsamples of image D-3. The moduli deduced from our ultrasonic measurements on Bentheimer sandstones are shown in blue diamonds. Also, we show similar measurements on clean arenites (<2% clay) with black cross and arenites (2-14% clay) with grey cross from published laboratory data set of Han et al. (1986).

Partially, this discrepancy is compensated by the linear extrapolation to resolution of $1\mu\text{m}$ (Figure 2.16). For bulk moduli the multi-phase segmentation and correction for resolution result in a good match with the ultrasonic measurements. Yet, the shear moduli are still systematically higher. This deviation may be empirically compensated by the adjustment of mineral moduli.

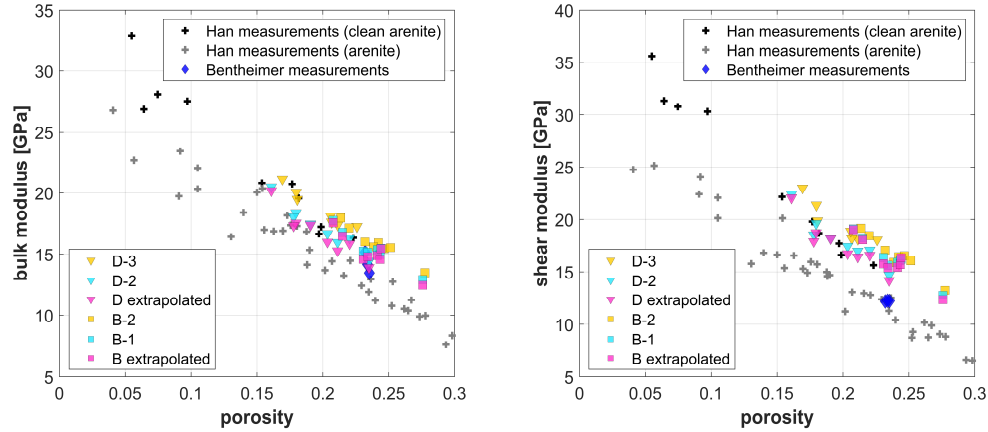


Figure 2.16 Computed moduli with different voxel sizes versus measurements. The triangle marks stand for the subsamples of sample B. The square marks stand for subsamples of sample D. Yellow and light blue marks stand for the moduli computed from four-phase images with low and high resolution respectively. Pink marks stand for the moduli extrapolate from moduli computed based on images with two different resolutions to 1 μ m voxel size. Blue diamonds, grey and black cross are the same as Figure 2.15.

A sharp drop of solid phase shear modulus with a small amount of clay has also been reported by Vernik (1997) and Goldberg and Gurevich (1998). They accounted for this effect by lowering the shear modulus of solid phase in rock physics modelling with calibrations from laboratory measurements. Vernik (1997) separated sandstones into several categories according to the clay content fraction and derive particular solid matrix moduli for each category. By contrast, Goldberg and Gurevich (1998) determined solid matrix moduli as a continuous function of clay fraction. Since we have specific clay content fraction from segmentation, we prefer the mineral moduli determined by Goldberg and Gurevich (1998).

2.5.2 Reduced matrix moduli

Goldberg and Gurevich (1998) proposed an empirical model that accounts for drop of the shear modulus due to the presence of clay. The model splits solid matrix into clay and sand, which have different moduli. The effective bulk modulus of the solid material is computed with lower Hashin-Shtrikman bound:

$$K_{solid} = K_{HS_} \quad (2.1)$$

In addition to the lower Hashin-Shtrikman bound, expression for the effective shear modulus includes an exponential term that accounts for the pronounced effect of clay:

$$\mu_{solid} = \mu_{HS_-} + (\mu_{quartz} - \mu_{sand}) \exp(-C/C_t), \quad (2.2)$$

where C is the clay content fraction, and C_t is the parameter that describes the interval of C over which μ_{sand} exponentially declines.

The derived effective moduli of the solid material are then substituted into the model of Krief, Garat, Stellingwerff, and Ventre (1990) to compute the effective moduli of the sample. With this rock physics modelling workflow and laboratory measurements by Han et al. (1986), Goldberg and Gurevich (1998) used a multivariate non-linear regression to derive the solid moduli as a function of clay content fraction.

Table 2.4 Elastic moduli of the mineral components used in computer simulations

	Bulk modulus (GPa)	Shear modulus (GPa)	Reference
Quartz	37	44	Carmichael (1989)
Feldspar	37	15	Mavko et al. (2009)
Kaolinite	12	6	Vanorio, Prasad, and Nur (2003)
Pore	0	0	
Matrix other than clay	39	function of clay	further derived from Goldberg and Gurevich (1998)
Clay	20	7.6	Goldberg and Gurevich (1998)

With clay volume from the segmented images, we further invert the shear modulus of matrix other than clay from solid shear modulus in Goldberg and Gurevich (1998), assuming only lower Hashin-Shtrikman bound relationship (Table 2.4). This matrix phase moduli are defined for the segmented quartz and feldspar phases. The moduli of clay from Goldberg and Gurevich (1998) are used for the segmented clay phase. Figure 2.17 shows the final computed moduli after the corrections for mineral moduli. The results agree well with the measurements on Bentheimer samples as well as Han et al. (1986) data. The observed agreement means that the proposed workflow may provide a rock physics template for velocity-porosity-clay relationships using only two sets of micro-CT images. Derivation of this template from the laboratory data would require ultrasonic measurements on dozens of samples and thin section/XRD for determination of the clay content.

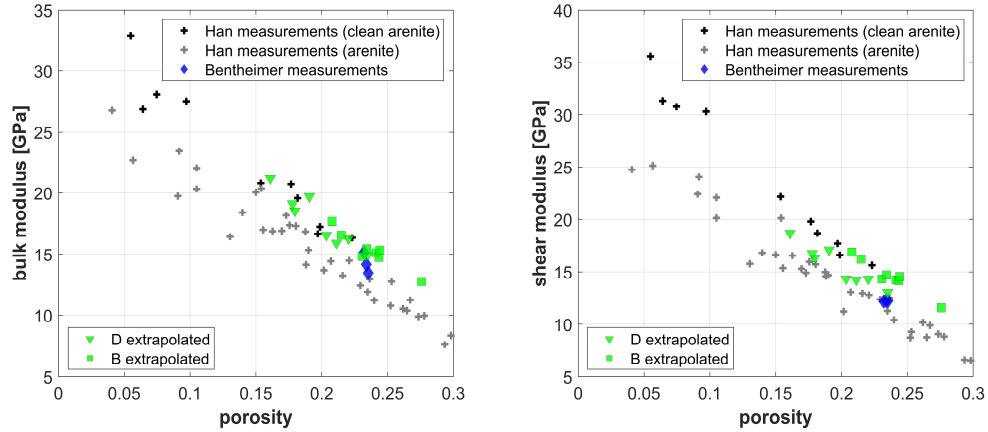


Figure 2.17 Computed moduli versus measurements. Green square marks stand for moduli extrapolated to $1\mu\text{m}$ of subsamples of sample B, and green triangle marks stand for moduli extrapolated to $1\mu\text{m}$ of subsamples of sample D. Blue diamonds, grey and black cross are the same as Figure 2.15.

2.6 Discussion

In this chapter, we carefully evaluated the effects of sample size, voxel size and segmentation on the computed moduli. With proper optimisation, the computed bulk moduli are consistent with the laboratory measurements. However, the presented data set – three samples and four sets of images – can only be used as an initial test. We discuss the basic assumptions behind the implemented DRP workflow below. To assess its accuracy and/or refine it, a more extensive data set is needed.

Estimates of shear modulus are known to be less accurate than the bulk modulus of sandstones (Bachrach & Avseth, 2008; Goldberg & Gurevich, 1998). The thin section in Figure 2.1 indicates that the presence of grain coating clay minerals which may prohibit some local quartz overgrowths, resulting in more complex and softer intergranular grain contact than the grain contact in clean sandstone (Han et al., 1986). However, this information is missing in the four-phase segmentation labels from micro-CT images. Also, we assumed that the contacts are fully closed at 40MPa. It is however known that sandstone samples continue to get stiffer until they collapse at really high pressure $\sim 150\text{MPa}$ (Adelinet, Fortin, Guéguen, Schubnel, & Geoffroy, 2010; David & Zimmerman, 2012). Furthermore, even with infinite resolution, careful discretisation of a contact would make computations intractable as the mesh has to be refined enormously near the grain contact to capture the complex stress distribution (Wong & Wu, 1995; Yastrebov, 2011). Thus, we would advocate an empirical

approach that reduces the mineral shear moduli for computing the effective elastic moduli, similarly to Vernik (1997) and Goldberg and Gurevich (1998).

Our workflow carefully verifies and integrates the DRP modules in previous studies. We evaluate sample size effect similarly to Saxena et al. (2019) and correct for the resolution effect based on the assumption of linear relationship between voxel size and moduli similarly to Arns et al. (2002). Periodic boundary conditions and voxel based mesh used in previous studies (Andrä et al., 2013b; Arns et al., 2002) are also shown to be appropriate in our workflow. The comparison of computed moduli against ultrasonic measurements is conducted by dividing the sample into subsamples and compute the moduli-porosity trend following Dvorkin et al. (2011). However, our workflow is not just a combination of the advantages of previous studies. The boundary condition effect on moduli is highlighted into notice and then compensated. A novel and effective approach of multi-mineral segmentation workflow is developed. This proves that the effect of minor amount of clay and feldspar on computed moduli, often neglected (Andrä et al., 2013b) or inverted from ultrasonic measurements (Saenger, Lebedev, et al., 2016), may be significant. Our reduced moduli approach is more practical as it is based on clay fraction derived from segmentation. It successfully counts in the assumed clay induced change of the shear modulus of the sandstone matrix.

Finally, the meshing part of workflow for numerical simulations was not explored thoroughly. We anticipate the computed moduli depend on the mesh size due to the stress concentration effect around relatively small contacts, especially, between clay particles. While it is relatively straightforward, studies optimizing the meshing parameters are relatively scarce (Aliyeva, Alabbad, Daza, & Mukerji, 2017; Cotton et al., 2016) as they require significant computational effort.

2.7 Conclusions

In this chapter, we developed an optimised digital rock physics workflow for predicting elastic moduli of sandstones with low clay content. Our approach recognizes the shortcomings of the micro-CT images as proxy for laboratory samples and does not attempt to replicate the laboratory measurements in the numerical simulations. Instead, we obtain a suite of post-computation corrections that are calibrated to images of different sizes and resolution and laboratory measurements.

First, we performed a set of simulations for images segmented into solid and pore constituents. We found that the boundary conditions induce size dependence into the computed effective moduli, which can be removed by an exponential correcting function. The insufficient resolution can be fixed by linear extrapolation to a desired voxel size based on the computations for images scanned with different resolution. Then, we developed a multi-stage four-phase segmentation graph that targets feldspar and clay minerals. In order to do so, we apply a combination of mathematical morphology filters, Otsu and watershed segmentation algorithms. Numerical simulations indicate that the appropriate segmentation graph and compensation for scanning parameters may reduce significantly the discrepancy between the measurements and computed moduli.

Eventually, the computed bulk modulus for multi-mineral matrix agrees well with the ultrasonic measurements at 40MPa, where the effect of unresolved compliant pores is small. The shear modulus remains overestimated. The discrepancy is corrected with an empirically determined matrix moduli. The current version of the workflow provides accurate velocity trends with porosity and clay content based on two samples of Bentheimer sandstone. Traditionally, such a relationship for quantitative interpretation would require ultrasonic measurements on dozens of samples and thin sections/XRD.

Chapter 3 Tracking the stress effect on micro-CT images of a reservoir sandstone[†]

3.1 Introduction

Understanding the relationship between microstructures and effective properties of rocks is a key for quantitative interpretation of geophysical measurements (Avseth et al., 2010). The recent development of micro-Computed Tomography (micro-CT) imaging technique provides high-resolution, three-dimensional representations of the pore geometry (Cnudde & Boone, 2013; Maire & Withers, 2014). Then, different physical processes are simulated based on the pore geometry to derive the rock effective properties (e.g., elasticity, permeability, electrical conductivity) (Andrä et al., 2013a, 2013b; Dai, Shikhov, Li, Arns, & Arns, 2021; Hossain, Arns, Liang, Chen, & Arns, 2019; Madadi, Jones, Arns, & Knackstedt, 2009). The whole “image and compute” workflow is called Digital Rock Physics (DRP).

Rock properties, especially elasticity, can be strongly pressure dependent (Eberhart-Phillips et al., 1989; Han et al., 1986; Zimmerman, 1990). However, micro-CT images, as the foundation of DRP, are mostly scanned under ambient pressure (Ahmed et al., 2017; Arns et al., 2002; Liang, Glubokovskikh, Gurevich, Lebedev, & Vialle, 2020a; Liang, Gurevich, et al., 2020; Shulakova et al., 2013). There are a few exceptional attempts to obtain medical CT and micro-CT images of rock at higher pressure. Kawakata et al. (1997) succeeded in observing faulting process in granite with medical CT images under confining pressure. Watanabe et al. (2011) scanned a fractured granite sample with medical CT at different confining pressures, and numerically simulate the corresponding fracture flow. Yu et al. (2019) scanned a fractured shale with micro-CT to investigate the fracture morphology changes under different confining pressures. Furthermore, a digital volume correction (DVC) method can be used on micro-CT images analysis to quantitatively describe the three-dimensional strain field inside the sample due to applied stress (Seyed Alizadeh, 2014). For

[†] This chapter is a modified version of the paper Liang, J., Lebedev, M., Gurevich, B., Arns, C. H., Vialle, S., & Glubokovskikh, S. (2021). High-Precision Tracking of Sandstone Deformation From Micro-CT Images. *Journal of Geophysical Research: Solid Earth*, 126(9), e2021JB022283.

example, Shi et al. (2021) monitored local creep strain field and cracking process in claystone by DVC analysis on micro-CT images.

Compared with fractured rocks and unconsolidated sediments, the study of pressure effect on intact sandstone micro-CT images is quite scarce. The deformation of intact sandstones under stress is much smaller, so the direct observation of it is very challenging. Saenger, Lebedev, et al. (2016) scanned a Bentheimer sandstone using micro-CT microscopy at confining pressures of 1MPa and 20MPa. The difference between the two sets of images (image size $400 \times 400 \times 400$ voxel, voxel size length $2.4 \mu\text{m}$) cannot be distinguished visually from the greyscale images. Saenger, Lebedev, et al. (2016) also compared the simulated elastic properties and permeability from images scanned at different pressures. The computed values are quite similar while the laboratory measurements show a strong pressure dependency. Furthermore, the traditional quantification of the strain field using the DVC method cannot capture small strain in an intact sandstone caused by small (under 50 MPa) stress. The application of DVC on intact objects is limited for determining large internal strain for soft materials (Bar-Kochba et al., 2015).

The study of Saenger, Lebedev, et al. (2016) concluded that the effect of stress on micro-CT image of Bentheimer sandstone was negligible. This suggests that we can compute elastic properties based on micro-CT images scanned at ambient pressure and there is no need to scan the rock at elevated pressures. However, there are still several questions requiring clarification. First, in the study of Saenger, Lebedev, et al. (2016), the comparison of micro-CT images scanned at different pressures were compared visually, which can be extended with more objective image analysis to detect the stress-induced displacement on the images. Secondly, even though the stress effect is shown to be small on computed elastic properties of Bentheimer sandstone, it is still not clear if image insensitivity of stress is applicable to other sandstones. According to previous studies, Bentheimer sandstone is quartz-cemented, and pressure dependency of elastic property may be weaker than for other less cemented sandstones (Peksa et al., 2015). Thirdly, the micro-CT images can be acquired with a much smaller voxel size length than $2.4 \mu\text{m}$, which was used in Saenger, Lebedev, et al. (2016). It is thus possible and interesting to see if higher resolution can better resolve the stress

effect on images. Lastly, a confining pressure of 20MPa may be still lower than in-situ pressure and can be raised further.

To address this objective, we study in this chapter the effect of confining pressure on micro-CT images of a gas reservoir sandstone. For this sandstone, laboratory measurements show significant pressure dependency of elastic properties. The sample is scanned at different confining pressures (up to 36MPa) in an X-ray transparent pressure cell (Lebedev, Zhang, Mikhaltsevitch, Inglauer, & Rahman, 2017). The voxel size length for image scanning is $\sim 1\mu\text{m}$ to capture more detailed information. With the difficulty of DVC detecting minor deformation, we design an unbiased workflow to detect the overall rock deformation under different pressures. For the first time, the displacement of an intact sandstone sample boundaries can be quantified from the micro-CT images scanned at different pressures. Then, we calculate the static bulk modulus based on the detected deformation, and compare it with the dynamic modulus derived from ultrasonic measurements to evaluate the accuracy of the deformation estimation workflow. We also compare the porosity change under pressure estimated using segmented labels from images with the value derived from the estimated static modulus using poroelastic theory. The results of this analysis prove the accuracy of the estimated displacement. Finally, we compute the elastic moduli and assess the stress effect on the computed results. The minor difference between the computed elastic moduli based on micro-CT images scanned at different pressures shows that micro-CT cannot capture most of the soft pores at the grain contacts, even with high resolution image scanning setting and higher pressure applied. Our results will enrich the understanding of confining pressure effect on the micro-CT images of sandstones and the corresponding estimated elastic properties.

3.2 Laboratory characterisation of sandstone sample

The studied sample is a Jurassic sandstone (named S60 hereafter) from a gas reservoir located offshore Australia in the Northern Carnarvon Basin. The original depth of this sample is about 2400m, which is above the common initial depth of quartz cementation (Dræge et al., 2006). According to the modal analysis performed with a Scanning Electron Microscopy-based technique (TESCAN integrated mineral analyser or TIMA) on a polished thin section (Figure 3.1), quartz is the most abundant mineral

(76.4% of the total minerals) with 11.6% of feldspar, 3.7% of clay and other accessory minerals. We cut a cylindrical sample (38.4 mm in diameter, 56.24 mm in length) for porosity and ultrasonic velocity measurements. Pressure dependent porosities are measured with helium porosimeter (Figure 3.2a). After stress loading and unloading, velocities are measured at ultrasonic frequencies (~ 1 MHz) in dry condition at confining pressures up to 40 MPa. Then, the sample is saturated with glycerol and ultrasonic velocities are again measured at several differential pressures. The uncertainty of ultrasonic measurements due to the ambiguity of first arrival picking is $\sim 1\%$ of the measured velocity. The measured velocities (and densities) are then used to compute pressure-dependent bulk and shear moduli (Figure 3.2b). This figure shows that the increase of effective pressure causes the compliant micro-pores and cracks of the sample to gradually close (Sayers, 1988), resulting in lower porosity. The closing of a small number of compliant pores with stress increases the elastic moduli (dry condition) almost a factor of two. The pressure dependency of the dynamic elastic moduli of the glycerol-saturated rock is much weaker, due to the significant squirt flow effect (Gurevich, Makarynska, de Paula, & Pervukhina, 2010). This indicates the abundance of micro pores, which is also the cause for the strong stress-sensitivity of the elastic moduli in dry condition.

A cylindrical mini-plug (5 mm in diameter, 20 mm in length) is extracted from the bigger sample used in the previous measurements. This plug is loaded into a pressure cell (Lebedev et al., 2017), which is made of X-ray transparent polyetheretherketone (PEEK). This pressure cell is then assembled in the 3D X-ray microscope VersaXRM 500 (XRadia-Zeiss). After stress loading and unloading cycles, sample is scanned at 0 MPa, 20 MPa and 36 MPa hydrostatic pressure. The voxel size lengths of three images are set to be exactly the same ($1.0042\mu\text{m}$) and the image sizes are approximately 2000^3 voxels. Then, the sample remains under ambient pressure for 21 days, before it is scanned at 0 MPa again with the same image size and resolution settings. This last image will be used as the reference image.

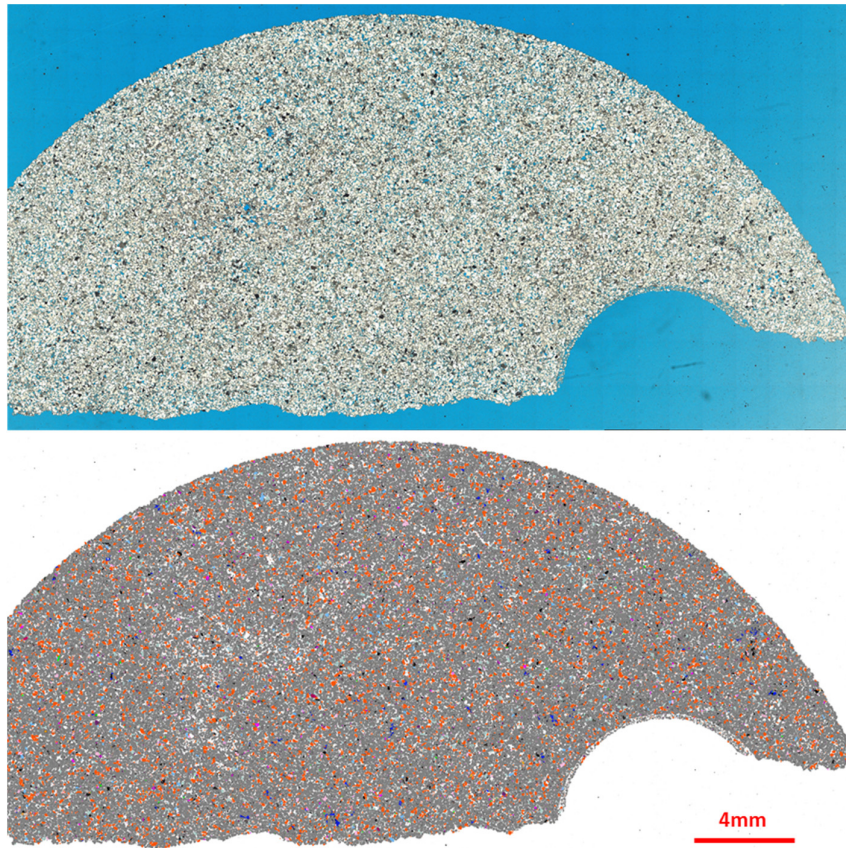


Figure 3.1 The optical microscopy (top) and TIMA (bottom) images of a thin section from S60. The image consists of quartz (shown in grey), feldspar (shown in orange) and other accessory minerals.

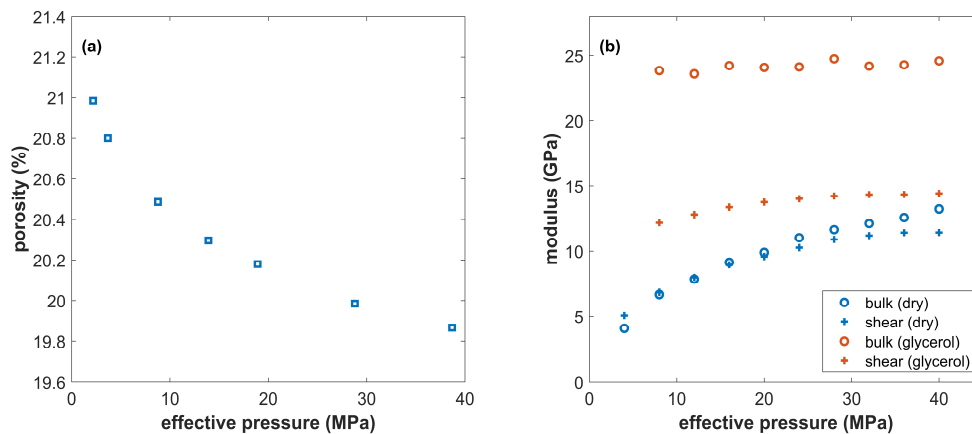


Figure 3.2 Pressure dependent properties of dry sandstone S60 from laboratory measurement: (a) helium porosity, (b) bulk and shear moduli derived from measured velocities at ultrasonic frequency in dry and glycerol-saturated conditions.

3.3 Pressure effect detection method

Next, we try to capture the pressure effect by comparing the first three sets of images with the baseline image. To this end, we process the micro-CT images with the software AVIZO (version 2020.2). First, we use a *non-local means filter* to suppress the random noise in the image while preserving the fine structures (Buades et al., 2005). Then, by setting the image scanned at 0MPa (image scanned after 21days at ambient pressure without residual stress) as the reference, the images scanned at 0MPa (with residual stress), 20MPa and 36MPa are rotated and moved rigidly (without rescaling) to eliminate the small shift between scans. This process is called registration and the metric to align the images is called normalized mutual information (Estévez, Tesmer, Perez, & Zurada, 2009). This metric is more robust than correlation methods, because it aims at minimizing the entropy, and does not require images with similar histograms. After registration, we try to select the maximum physical part of the sample that can be found in all the four scans. Visually, we find that the same part of the sandstone sample, which occupies $1255 \times 1021 \times 1620$ voxels in the reference image, shrinks slightly when imaged in other pressure conditions. The difference between two adjoining slices is tiny, and it is difficult to identify the deformation accurately by visual inspection. Next, we try to use the 2D slice searching method to quantitatively and unbiasedly locate the same physical part of the sample in different images.

First, we select the cube of $1255 \times 1021 \times 1620$ voxels in the reference image. Based on the visually identified corresponding parts in the other images, we select slightly larger cubes as targets. Each time we pick one of the six boundary slices of the reference cube and try to automatically locate the corresponding slice in the group of boundary slices of the target images (Figure 3.3). Again, the similarity is quantified with normalized mutual information (Figure 3.4). We find that the same physical part of the studied sample S60 occupies the space of $1255 \times 1021 \times 1620$ voxels at 0MPa (without residual stress), $1253 \times 1019 \times 1616$ voxels at 0MPa (with residual stress), $1250 \times 1017 \times 1613$ at 20MPa, and $1252 \times 1017 \times 1613$ at 36MPa (Figure 3.5). This means that the stress-induced deformation of an intact sandstone can be detected on the micro-CT images, even when the volumetric strain derived from deformation is only on the order of 0.001. More specifically, first, the amount of deformation can characterise how the residual stress affects the sandstone by comparing the two scans

at 0MPa. Secondly, the deformation is more significant between 0 and 20MPa than between 20 and 36MPa.

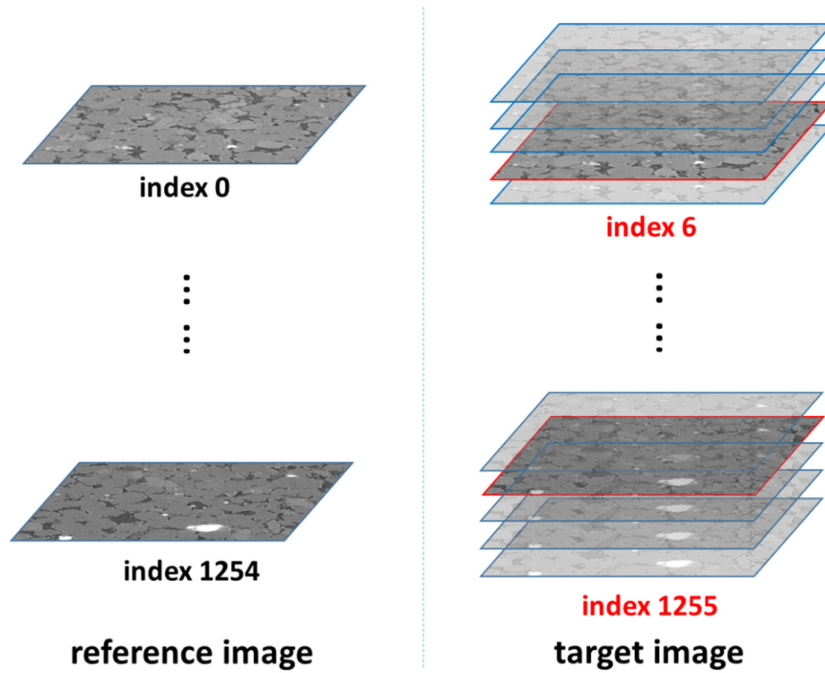


Figure 3.3 Diagram of the slice searching workflow in one dimension. The reference image is scanned at 0MPa (without residual stress), and the target image is scanned at 20MPa. In the reference image, two boundary slices with the index of 0 and 1254 (length of 1255 voxels) correspond to the slices with the index of 6 and 1255 (length of 1250 voxels) in the target images.

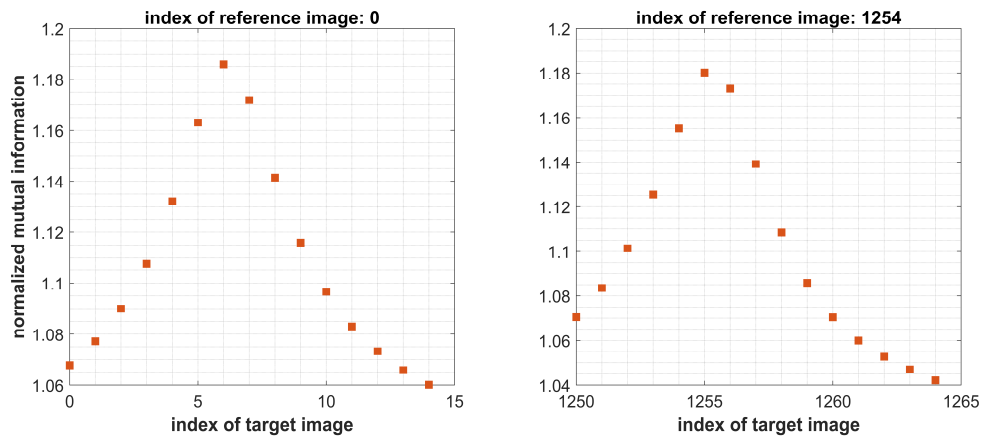


Figure 3.4 Searching for the best matching slices with normalized mutual information metric. The reference image is scanned at 0MPa (without residual stress), and the target image is scanned at 20MPa. The slices with index of 0 and 1254 (length of 1255 voxels) in the reference image correspond to the slices with the index of 6 and 1255 (length of 1250 voxels) in the target image.

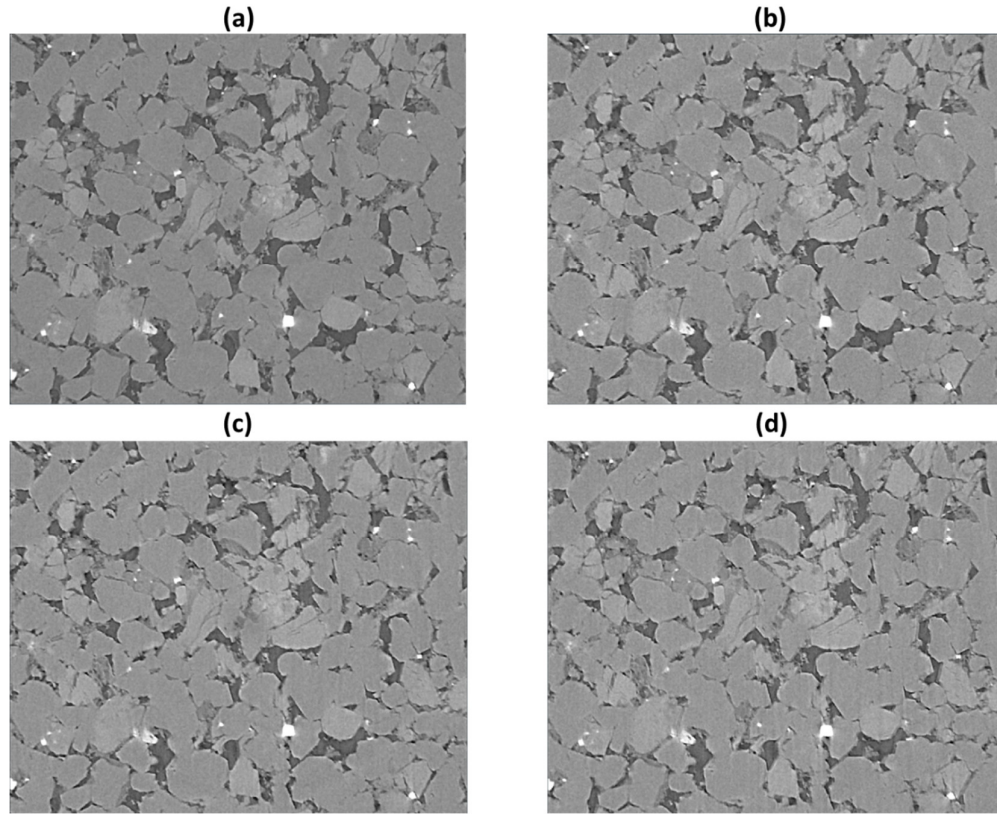


Figure 3.5 2D slices of micro-CT images showing the same physical part of sample S60 scanned at (a) 0MPa (without residual stress), (b) 0MPa (with residual stress), (c) 20MPa, and (d) 36MPa.

After locating the same physical part of the S60 sample on the micro-CT images scanned under different stress conditions, we segment the greyscale images into pore and solid phase with the Otsu method (Liang, Gurevich, et al., 2020; Otsu, 1979). The porosity of the same part of S60 is 0.1753 at 0MPa (without residual stress), 0.1673 at 0MPa (with residual stress), 0.1621 at 20MPa, and 0.1625 at 36MPa. To make a comparison, we fit the porosity measured for the larger sample with helium porosimeter with a $a - bx + ce^{-dx}$ relation. The fitted porosity decreases from 0.2127 at 0MPa to 0.2015 at 20MPa, and 0.1989 at 36MPa. It should be noted that the sample sizes for micro-CT scanning (mm scale) and porosity measurements (cm scale) are quite different, and the comparison are for qualitative understanding only. Next, we will calculate the static bulk modulus based on the detected deformation and compare with the dynamic modulus derived from ultrasonic measurements.

3.4 Estimates of the static moduli

The static bulk modulus of a rock refers to the elastic property derived from the ratio between static confining pressure and volumetric strain. The common way of measuring static bulk modulus is by strain gauges. The searching slice strategy described above gives an opportunity to calculate the static bulk modulus of a millimetre scale sample. Elastic moduli of our sample are highly pressure dependent, but it is only scanned at discrete pressure settings. Thus, the static bulk modulus derived from images is an effective value of a large pressure interval (e.g., 0-20MPa).

The estimation of the strain from micro-CT images is limited by the voxel size. To improve the result, we further resample the group of boundary slices in the target images. The resampling is conducted with the Lanczos method to decrease the voxel size length from 1.0042 μm to 0.10042 μm (Madhukar & Narendra, 2013). Because we will later compare the static moduli detected from images and dynamic moduli derived from the ultrasonic measurements and the ultrasonic velocities are measured after pressure loading and unloading, we will now use the image scanned at 0MPa after loading and unloading process as reference. After resampling, we find that the same physical part of S60 occupies the space of 1253 \times 1019 \times 1616 voxels at 0MPa (with residual stress), of 1250.1 \times 1016.6 \times 1611.9 at 20MPa, and of 1251.8 \times 1016.5 \times 1612.2 at 36MPa. The effective static bulk modulus from 0MPa to 20MPa is 2.78GPa. The sandstone under pressures of 20MPa to 36MPa is much stiffer than that in the lower pressure range, so the strain is comparable to the accuracy limit of the deformation detection workflow. We also try several resampling methods other than Lanczos, and the estimated static bulk modulus is invariant.

The derived static modulus can be further used to derive the porosity change from 0MPa (with residual stress) to 20MPa. The stress dependency of porosity can be described with poroelastic theory as below

$$\frac{d\phi}{dP} = \frac{1}{K_{gr}} - \frac{(1-\phi)}{K}, \quad (3.1)$$

where ϕ , P , K_{gr} and K stand for porosity, pressure, bulk modulus of grain material and dry rock frame (Zimmerman, 1990). K is assigned to be the static modulus derived

from the deformation (2.78GPa) and K_{gr} is assumed to be the bulk modulus of quartz (37GPa) (Mavko et al., 2009). As shown from the segmented label, the porosity is 0.1673 at 0MPa (with residual stress). Based on that, the derived porosity at 20MPa with poroelastic theory is 0.1618. The porosity change estimated with equation (3.1) is 0.0055, which is very close to, but slightly higher than, the resolvable porosity change from the segmented images (0.0052). The difference may be attributed to measurement or segmentation errors, or perhaps to the closure of the soft porosity unresolvable in the micro-CT image; indeed soft porosity is usually estimated to be on the order of 10^{-4} to 10^{-3} (Mavko & Jizba, 1991; Shapiro, 2003). This demonstrates the accuracy of the slice matching workflow.

3.5 Comparison between static and dynamic bulk moduli

Dynamic bulk modulus is the elastic property derived from the velocities of elastic waves propagating through the rock. According to the theory of elasticity, the dynamic and static moduli of a dry rock are one and the same. Indeed, the standard expressions for the compressional and shear wave velocities are derived from static Hooke's law. However for many dry rocks, static bulk modulus is smaller than dynamic one, mainly due to strong non-linearity caused by the presence of pores and cracks (Cheng & Johnston, 1981). Here, we compute the static and dynamic bulk modulus ratio and compare with literature values.

The dynamic bulk modulus of a core sample is obtained from ultrasonic and density measurements. The static and dynamic moduli are based on samples of different scales and the comparison is for qualitative understanding only. To match the effective static modulus, we need to extrapolate the effective dynamic modulus to the same pressure increment as the static moduli are measured from the images. Based on discrete ultrasonic measurements (Figure 3.2b), a regression is applied to derive a continuous function of compressibility (reciprocal of bulk modulus) and pressure. Then the strain between 0 and 20MPa is integrated. The accumulated volumetric strain is 0.0036247. Assuming the bulk modulus is a constant value in the pressure range from 0MPa to 20MPa, we can calculate the effective dynamic bulk modulus to be $20\text{MPa}/0.0036247 = 5.52\text{GPa}$. The integration of strains and stresses implies that the sample is linearly elastic within 0-20MPa. For such a pressure-sensitive rock, this assumption is

definitely invalid; hence the dynamic modulus obtained should be regarded as a linearized proxy, and not a modulus that we would have measured if the stress amplitude in the wave were ± 10 MPa (or strain amplitude ± 0.002). The static to dynamic modulus ratio is 0.504, which is consistent with the literature values (Cheng & Johnston, 1981; Fjær, 2009). Next, we will try to see the stress effect on the computed elastic moduli.

3.6 Pressure effect on computed elastic moduli

Based on the slice searching method, we locate the same physical part of sandstone in images scanned at different pressures. After the two-phase segmentation, we assign the bulk and shear moduli to be 0 for pore phase and, respectively, 37 and 44GPa for the solid phase. Then, we use the finite-element method to compute the effective elastic properties, treating each voxel as a trilinear finite element (Arns et al., 2002). The computed results are listed in Table 3.1.

Table 3.1 Comparison of properties from images scanned at different pressures.

Stress condition	Voxel	Porosity	Bulk modulus	Shear modulus
			(GPa)	(GPa)
0MPa (without residual stress)	1255×1021×1620	0.1753	20.8	22.0
0MPa (with residual stress)	1253×1019×1616	0.1673	21.7	23.1
20MPa	1250×1017×1613	0.1621	22.3	24.1
36MPa	1252×1017×1613	0.1625	22.2	24.1

The differences between the moduli computed from images at 0MPa (without residual stress) and 36MPa are 5.8% in bulk modulus and 9.5% in shear modulus. This indicates that the micro-CT images captured a small amount of confining pressure effect. Also, it shows that the pressure effect on computed elastic properties is more significant in the lower pressure range than at higher pressures.

Next, we compare pressure dependency of elastic properties from computation and ultrasonic measurements. As the sample is loaded and unloaded with stress before ultrasonic measurements, the reference computed elastic property here is also taken

from images scanned at 0MPa with residual stress. The comparison between computed results between images of 0MPa (with residual stress) and 36MPa shows that the differences are 2.3% in bulk modulus and 4.3% in shear modulus. In contrast, the elastic moduli derived from ultrasonic measurements increased by around 200% between these pressure points (Figure 3.2b).

3.7 Discussion

The stress induced deformation in the micro-CT images of an intact sandstone is extremely small and obscured by random noise and other artefacts from the image scanning and reconstruction processes. Thus, it is extremely difficult to identify the pore scale difference visually or with traditional digital volume correlation algorithms. By selecting a boundary slice of reference image, we use image registration to search for the most similar slice in the target images. We use normalized mutual information as the criteria to match slices, and compute the entropy by taking the information of the whole slice. The main advantage of this approach is that the differences from stress are accumulated while the random effects are cancelled out. Also, normalized mutual information does not require images with similar histograms, which may change in scans at different pressures. By minimizing the entropy between the reference and target slices, the matching slices can be located and the corresponding displacement of the sample boundaries can be deduced. Based on this technique, we see the more significant deformation when the stress is changed from 0MPa to 20MPa and minor deformation when the stress is further increased from 20MPa to 36MPa, which is in agreement with the laboratory observations. Furthermore, we observe the residual stress effect from micro-CT images.

Even though the overall deformation can be detected from the images, the relative changes of computed elastic properties from micro-CT images under stress is 20 to 30 times less than that derived from ultrasonic measurements. The much smaller relative change of computed moduli implies that the increased stress mainly stiffens already existing intergranular contacts by increasing either the number or area of the contacting asperities and closing nanopores (Glubokovskikh, Gurevich, Lebedev, Mikhaltsevitch, & Tan, 2016). To be noted, a direct match of moduli from computation and experiment may not be expected and DRP is only invoked to test whether there is sensitivity to

confining pressure by considering a 2-phase segmentation alone. In this current study, we are trying to understand the stress effect on the micro-CT images. We assume that the strong pressure dependency of elastic properties observed in the ultrasonic measurements results from the soft pores at grain contacts. Also, we assume the soft pores are surrounded by quartz, and if the soft pores are not resolved in the micro-CT, they are segmented to be quartz. We believe that it suffices to segment micro-CT images into two phases to see the effect of soft pore resolving differences on the relative pressure dependency of the rock. Segmenting micro-CT images into more difference phases with a workflow involving manual factors would increase the uncertainty of the segmentation process. Since the computed moduli difference with micro-CT images scanned at different pressures are very small, the segmentation uncertainty may obscure the stress effect on the computed moduli (which is the focus of this study). Based on the previous studies and our results, it can be concluded that DRP cannot fully capture the pressure dependent elasticity of intact sandstones directly from the micro-CT images.

A possible solution to overcome the limitation is to reconstruct the grain contact according to grain geometry (Arns, Madadi, Sheppard, & Knackstedt, 2007; Madonna et al., 2012; Saenger, Lebedev, et al., 2016). This so-called grain contact phase is actually a combination of grain and unresolved micro pores. In this approach, the grain contact part is considered as a separate phase with lower moduli than those of pure grains. The detected global scale deformation can be a source of information to estimate the effective moduli of the grain contact phase.

3.8 Conclusions

We have investigated the pressure effect on high-resolution micro-CT images of a reservoir sandstone and on elastic properties computed from these images. The X-ray transparent pressure cell allows micro-CT scanning at confining pressures of up to 36MPa. The images produced at different pressures are very close to each other and the differences are almost invisible to a naked eye. To detect these differences, we designed a slice matching workflow. Application of this workflow to our images shows that the same physical part of the studied sample occupies the space of $1255 \times 1021 \times 1620$ voxels at 0MPa (without residual stress), $1253 \times 1019 \times 1616$ voxels

at 0MPa (with residual stress), $1250 \times 1017 \times 1613$ at 20MPa, and $1252 \times 1017 \times 1613$ at 36MPa. The detected deformation is larger from 0MPa to 20MPa, than from 20MPa to 36MPa. The effect of stress release is also detected by comparing the images at 0MPa with and without residual stress. The derived static bulk modulus from deformation from 0MPa to 20MPa is 2.78GPa, which is consistent with literature values. The porosity change detected from segmented labels is consistent with the value derived from static modulus using poroelastic theory.

The images scanned at different pressures were used to compute the effective elastic moduli. The difference between the computed moduli is much smaller than the difference between the ultrasonic measurements. This shows, consistent with previous studies, that micro-CT imaging cannot resolve the geometry of grain contacts responsible for the pressure effect on the elastic properties. The accuracy improvement of the estimated elastic properties from images scanned at higher pressures is negligible. One way to overcome this limitation is to parameterize the pressure dependency of the contact stiffness indirectly.

Chapter 4 Grain contact stiffness inversion with digital rock physics

4.1 Introduction

Sandstone is a type of sedimentary rock with the structure of silicate grains deposited in contact. The stiffness of the grain contact plays a critical role in defining effective elastic moduli of sandstones (Digby, 1981; Winkler, 1983). In the diagenesis process of sandstone, with the first bit of cement at grain contacts, the elastic moduli of a sandstone increase sharply (Dvorkin, Nur, & Yin, 1994). With growing effective stress, the crack-like soft pores at grain contacts may be progressively closing, resulting in strong increase of the elastic properties of sandstones (Pervukhina, Gurevich, Dewhurst, & Siggins, 2010; Shapiro, 2003). Thus, grain contact stiffness is the key factor in understanding and predicting the cementation and stress effect on the effective elastic moduli of sandstones.

With the rapid advances in imaging and computing capacity, Digital Rock Physics (DRP) has emerged as an tool for the analysis of pore-scale processes governing effective elastic rock properties (Andrä et al., 2013a). This technique relies on numerical simulations of rock deformation for a given rock microstructure, which may be obtained directly from real rock micro-Computed Tomography (micro-CT) images (Sain, 2010). However, even with the latest synchrotron-based X-ray tomographic microscopy, micro-CT still cannot resolve the majority of soft pores at grain contacts due to resolution limitation. Ignoring compliance of these contacts leads to a significant overestimation of computed elastic moduli (Madonna et al., 2012). An alternative way is to reconstruct the contacts according to the morphology of grains using watershed separation algorithm (Madonna et al., 2012; Saenger, Lebedev, et al., 2016). These approximated grain contacts can then be treated as a uniform phase with lower moduli in the numerical computation. Hereafter, the term “grain contact” will be representing the approximated composite phase with soft pores and the neighbouring enclosing solid.

Saenger, Lebedev, et al. (2016) tried to take advantage of ultrasonic measurements to determine the value of the reduced grain contact moduli. A bigger sample and a smaller sample were cut from the same Bentheimer sandstone block for ultrasonic measurements and micro-CT imaging respectively. Ultrasonic measurements were conducted in dry condition at pressures from 4MPa to 20MPa. Greyscale micro-CT

images were segmented into three phases (pore, solid and contact zone). The overestimated computed moduli were first corrected to match the ultrasonic measurements at 20MPa by multiplying a coefficient, assuming grain contact effect on elastic moduli was minimum at 20MPa. Then, grain contact moduli were varied from 2% to 100% of quartz moduli to match the ultrasonic measurements at different pressures, to take into account of the effect of unresolved soft pores.

In order to derive meaningful contact moduli with inversion, several factors need to be better investigated. First, because of the difficulty of segmenting minerals out of grayscale micro-CT images, the solid part of rock sample is usually assumed to be a single phase (Andrä et al., 2013a). Yet, a sandstone often contains soft clay minerals or stiff carbonate cements, and the amount or the distribution of them may induce significance difference in effective elastic moduli (Dræge et al., 2006) (also see Chapter 2). Moreover, the effect of a contact may depend on the specific minerals connected by this contact. Second, in Saenger, Lebedev, et al. (2016), to estimate the contact moduli, the computed moduli are corrected to match the measured velocity at higher pressure (20MPa), assuming the contact moduli are the same as pure quartz. However, soft pores might not be fully closed until several hundred MPa (de Paula, Pervukhina, Makarynska, & Gurevich, 2012; Sun & Gurevich, 2020), which is well beyond the pressure range for common laboratory ultrasonic measurement. Third, even when we have multi-mineral segmented labels, the choice of corresponding mineral moduli is uncertain. Mineral moduli from laboratory measurements on mineral crystals (McSkimin, Andreatch Jr, & Thurston, 1965) and those derived with extrapolation of ultrasonic measurements on natural rocks to zero porosity (Vernik, 1997) are different. This uncertainty of matrix moduli will then affect the accuracy of the inverted grain contact moduli. Fourth, previous studies, attempted to match laboratory measurements, using a micro-CT image with similar porosity to that of the laboratory sample. Yet, the mercury porosimetry shows that up to ten percent of pores may be unresolved in the micro-CT images (Saenger, Lebedev, et al., 2016). This means that the comparison between computation and laboratory measurements is based on a higher porosity sample for imaging and lower porosity sample for ultrasonic measurements. This mismatch can cause additional errors in the estimated contact moduli. Due to these important factors, the grain contact moduli may be able to act as

fitting parameters, but may represent not just the properties of the contact (geometry, cementation, fluid content etc.), but also factors related to a larger area of the sample (such as position with respect to various mineral components and to other contacts, mineral moduli or unresolved porosity). As modelling contacts as flat layers of a fixed thickness is very idealised, the contact moduli derived in this way are still fitting parameters but they should be related to the properties of the contact (e.g., geometry, cementation, fluid), which is useful for analysis of the effect of these properties on the overall rock moduli.

In this chapter, we try to overcome these limitations by deriving the grain contact stiffness of a Bentheimer sandstone and a natural gas reservoir sandstone named S60 (S60 was also studied in Chapter 3). The contact stiffness will be inverted by varying the contact stiffness to match the computed elastic moduli based on high resolution micro-CT images with a full set of ultrasonic measurements at different pressures in dry condition. We will take advantage of a newly developed multi-mineral segmentation workflow which successfully segments different common minerals from micro-CT images (Chapter 2). To better define the mineral moduli, we will refer to values in recent literature and constrain them with the nano-indentation technique. Very importantly, we will take the micro-CT image subset with porosity reasonably smaller than laboratory samples to do the computation. Nuclear magnetic resonance (NMR) will be used to estimate the porosity that cannot be resolved in micro-CT images. With these efforts, the inverted contact moduli can better describe the stiffness of grain contacts when the cementation or pressure condition varies. More samples can be studied with this method to build a library of contact stiffness in different cementation and stress conditions. Thus, DRP is empowered with the ability to describe the cementation and pressure changes on the effective moduli by adjusting grain contact moduli within the reasonable range.

4.2 The laboratory study

Two sandstone samples were selected for this study: a Bentheimer sandstone and a reservoir sandstone named S60. According to previous studies, quartz is the main component of the Bentheimer sandstone matrix (mostly 90-98%) (Peksa et al., 2015). Even though Bentheimer sandstone is an outcrop sandstone, it has gone through moderate diagenesis. Quartz cement has grown around the original detrital quartz

grains and reduced the pore space. The accessory feldspar has been partially weathered to generate clay, which precipitates around the grains or fills the pores, especially the narrow parts around the grain contacts. When some parts of grains are coated by the early formed clay, the quartz cement may be difficult to precipitate, so the cement growth is inhibited (Ajdukiewicz & Lander, 2010). As a result, some grain contacts may be with lower stiffness than quartz grains (Figure 4.1).

S60 is a Jurassic sandstone from an Australian natural gas reservoir. According to the analysis on a polished thin section with TESCAN integrated mineral analyser (TIMA) (Figure 4.2), S60 has more mineral complexity than Bentheimer sandstone. The most abundant mineral is quartz (76.4% of the total minerals), with 11.6% of feldspar, 3.7% of clay, as well as other accessory minerals. The more abundant feldspar and clay may inhibit the quartz overgrowth more considerably than that in the Bentheimer sandstone, resulting in possibly weaker grain contact in S60.

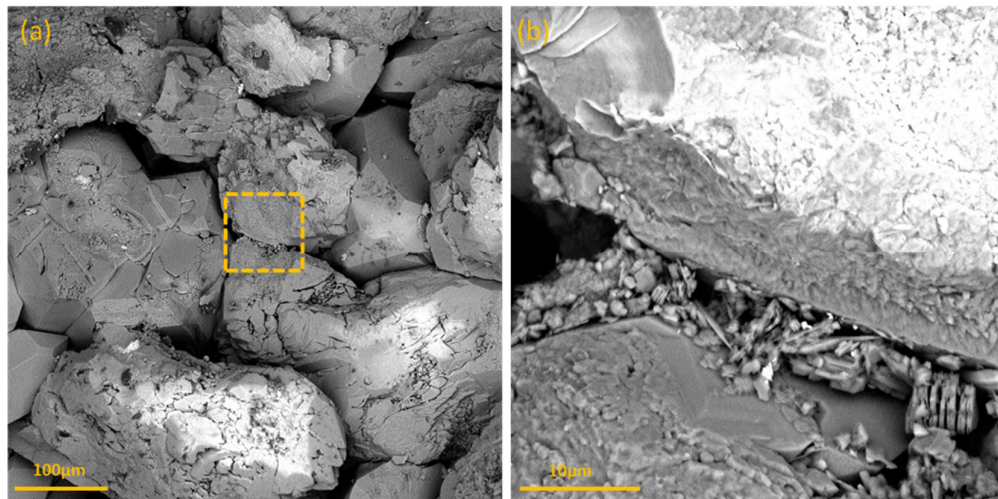


Figure 4.1 Scanning Electron Microscope (SEM) image of a Bentheimer sandstone. The location of the high-magnification image (b) is marked with a yellow dashed square within the low-magnification image (a).

4.2.1 Ultrasonic and porosity measurements

A cylindrical part (~38mm in diameter, ~50 mm in length) of each sample was extracted from block or core for porosity and ultrasonic (~1MHz) velocity measurements. Samples were cooled with frequently sprinkled water when cutting. For ultrasonic velocity measurement, samples were kept in a drying chamber at 50°C for 24 hrs. Then, velocities were measured in dry condition at different hydrostatic

confining pressures. The elastic moduli derived from the measured ultrasonic velocities are shown in Figure 4.3. The measured velocity in S60 shows much stronger pressure dependency than in the Bentheimer, probably due to differences in the grain contact cementation. For porosity measurements, samples were dried for 24 hrs at 105°C in a vacuum oven. After measurement of the mass (m_{dry}) of a dry sample, the sample was fully saturated with brine (NaCl 3.5%) under vacuum. The mass of sample was measured again (m_w) and the porosity was determined as $(m_w - m_{dry})/V_w$, where V_w stands for the bulk volume of the sample and the density of the water is assumed to be 1000 kg/m³. The porosities of Bentheimer and S60 sample were measured to be 0.2381 and 0.2105.

4.2.2 Micro-CT imaging

A cylindrical mini-plug (5 mm in diameter, 20 mm in length) was then extracted for micro-CT scanning from the larger sample used in the previous measurements. These two mini-plugs were scanned with 3D X-ray microscope VersaXRM 500 (XRadia-Zeiss) with consistent scanning parameters (Figure 4.4). The voxel size length and voxel number of Bentheimer sandstone micro-CT image is 1.0000 μ m and 1984 \times 2028 \times 1998 voxels, while the parameters for S60 micro-CT image are 1.0042 μ m and 1980 \times 2028 \times 1991 voxels. The choice of scanning parameters is based on the study in Chapter 2. The scanning parameter evaluation for Bentheimer sandstone showed that theoretical representative volume element criteria could not be fulfilled even with lower resolution setting. However, sample size with \sim 1.25mm edge length seemed to be able to provide a locally stable image set for elastic moduli estimation. The voxel edge length of \sim 1 μ m is the highest resolution that can be achieved with the selected sample size, considering the limitation of the scanning apparatus.

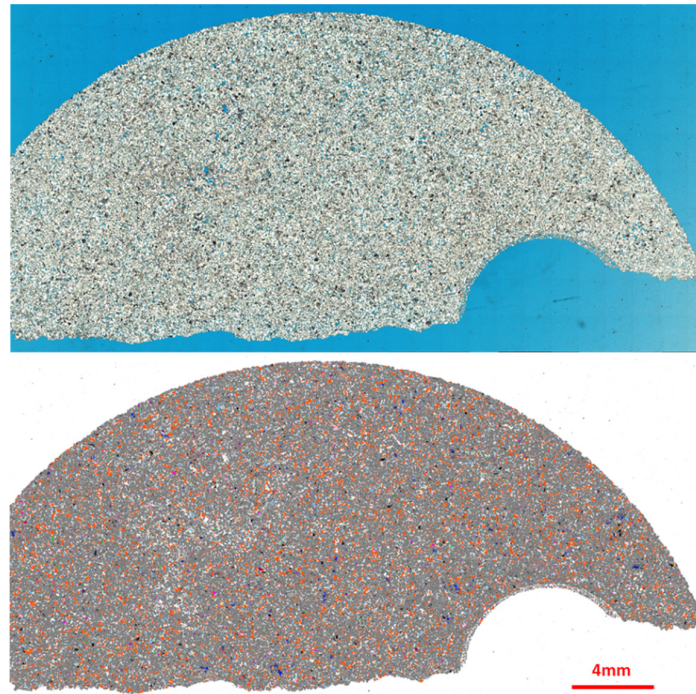


Figure 4.2 The optical microscopy (top) and TIMA (bottom) images of a thin section from S60. The image consists of quartz (shown in grey), feldspar (shown in orange) and other accessory minerals.

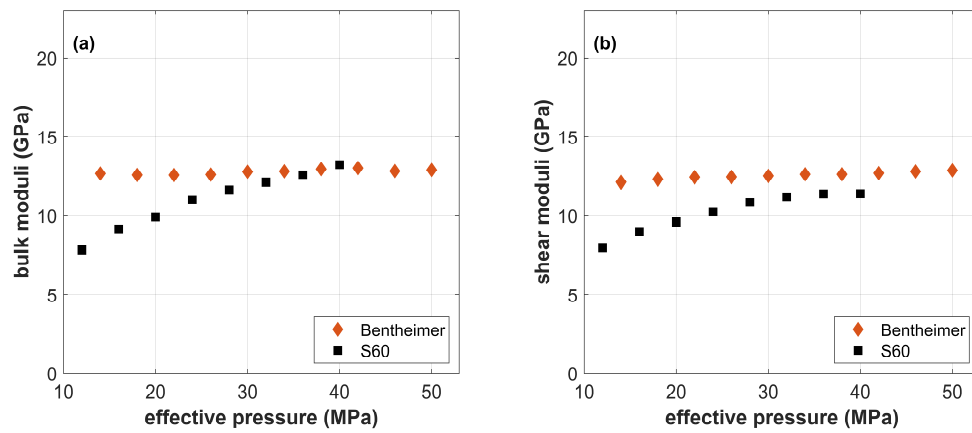


Figure 4.3 Elastic moduli of Bentheimer and S60 sample derived from ultrasonic measurements under different pressures in dry condition.

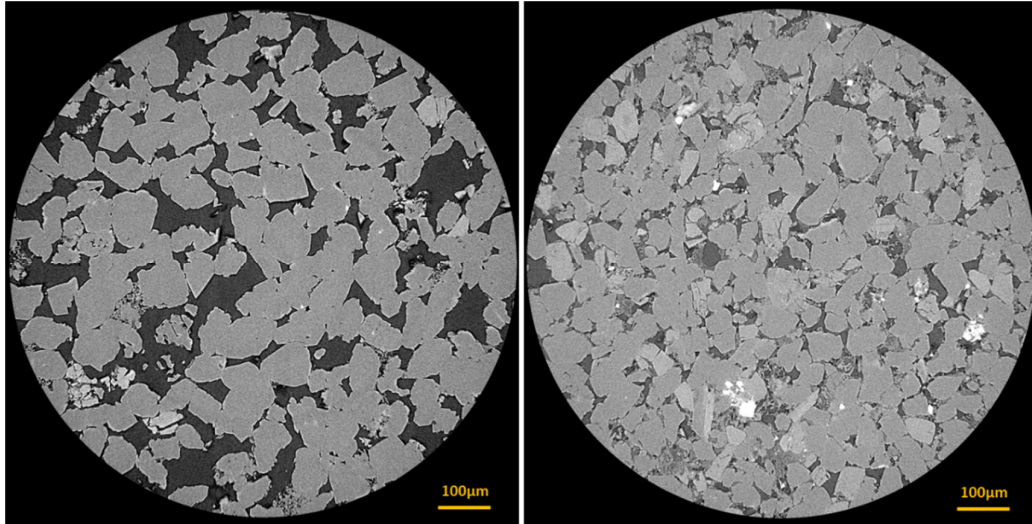


Figure 4.4 Micro-CT images of Bentheimer (left) and S60 sample (right). Only one slice of each set of image is shown here.

4.2.3 Nuclear Magnetic Resonance for pore size distribution estimation

Compared with the SEM image (Figure 4.1), micro-CT images cannot resolve most of the minor pores at grain contact, even with 1µm voxel size length. To quantify the unresolved soft pores, Nuclear Magnetic Resonance (NMR) measurements were used to estimate the pore size distribution of two samples. The measured NMR T_2 relaxation time distributions (Figure 4.5) indicates that there are three groups of pores, which are filled with bound water within the clay clusters, weak bound water at grain contacts and free water in the big pores.

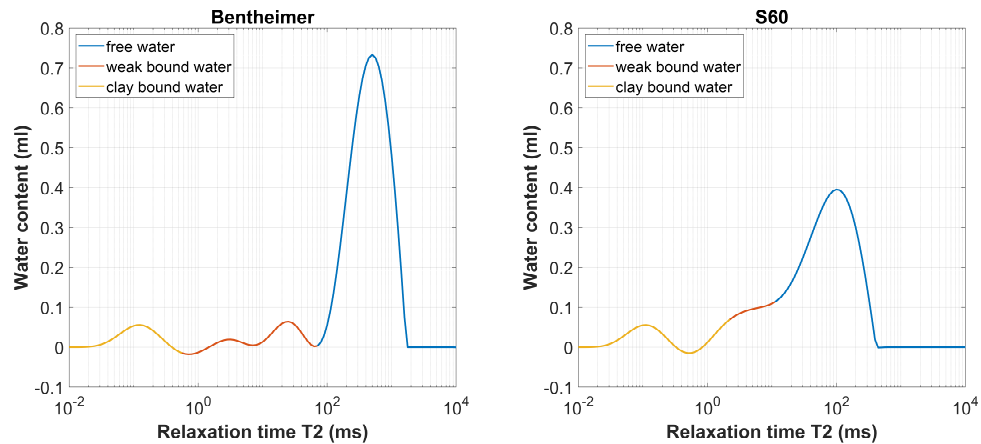


Figure 4.5 The NMR T_2 relaxation time distributions of Bentheimer and S60 sample.

T_2 can be correlated with surface to volume ratio (A/V) of pores by equation (4.1), if the surface relaxivity ρ is known (Zhang, Kruschwitz, Weller, & Halisch, 2018),

$$\frac{1}{T_2} = \rho \left(\frac{A}{V} \right). \quad (4.1)$$

Assuming the pore is cylindrical with radius r , A/V equals $2/r$. Then, pore radius r can be calculated as

$$r = 2\rho T_2. \quad (4.2)$$

The surface relaxivity parameter of Bentheimer sandstone was measured to be 9.5 $\mu\text{m/s}$ using the laser-induced breakdown spectroscopy (Washburn, Sandor, & Cheng, 2017). We can understand that micro-CT with 1 μm voxel length cannot resolve the pores of Bentheimer sample with relaxation time lower than $\sim 50\text{ms}$, which is approximately the separation point between pores filled the free water and bound water. Thus, we assume only the pores filled with free water can be resolved in micro-CT with 1 μm voxel length. Combining the total measured porosity, the resolved porosity is 20.81% for Bentheimer sample and 17.64% for S60 sample. In the following study, we will choose the image set with the porosity similar to the resolved porosity instead of the total porosity. It should be noted that if the image set with the resolved porosity matching the total porosity of sample for ultrasonic measurement is selected, the unresolved pores in image set are overlooked.

4.2.4 Nano-indentation as a reference for mineral moduli

The moduli of mineral are important input parameters for effective elastic moduli estimation (Amini, 2019), yet these parameters are uncertain. These moduli can be obtained from laboratory measurements on mineral crystal or derived by extrapolation of ultrasonic measurements on natural rocks to zero porosity (Table 4.1). The values from different sources are quite different and the best choice is not clear. Also, sandstones can have different variants of the same mineral, so it is best to obtain mineral properties from direct measurements on the same rock (even on a different scale). To help resolve this uncertainty, the stiffness (Young's modulus) was measured with nano-indentation tests on single grains in S60 at the micrometre scale. For that purpose, a billet size piece of S60 was prepared as a polished, blue resin impregnated, section on slide by Adelaide Petrographic Ltd. The apparatus used was an IBIS nano-

indentation system (Model B, Fisher-Crips Laboratories Pty. Ltd.), equipped with a diamond, Berkovich-type indenter, which was used in the static mode (Lebedev, Wilson, & Mikhaltsevitch, 2014). The tests consist in recording the applied incremental load P and the displacement h of the indenter as it pushes into and withdraws from the surface of the polished thin section. A constant maximum loading force of 10mN and an initial contact force of 0.15mN were used. In total, 961 (31×31) measurements were performed on a 150×150μm surface with a spacing of 5μm between the measurement points as in Saenger, Vialle, et al. (2016). Elastic properties, namely indentation moduli, were computed from the $P-h$ curves, assuming a continuum scale mechanical model and a purely elastic material. The nano-indentation system was calibrated using a standard of fused silica (Young’s modulus of 72.5GPa) and data were further corrected from deviation of the indenter tip from ideal geometry, initial penetration into the rock below a load threshold and compliance of the loading column. Uncertainty of the apparatus is estimated to be about 2GPa based on a large number of measurements performed on the silica standard.

Table 4.1 Moduli of common minerals of sandstone matrix from different sources

	Bulk modulus (GPa)	Shear modulus (GPa)	Young’s modulus (GPa)	Source
Quartz	37	44	94.5	McSkimin et al. (1965), mineral measurement
Microcline	59.5	30.3	77.7	Waeselmann et al. (2016), mineral measurement
Albite	59.4	35.5	88.8	J. M. Brown, Abramson, and Angel (2006), mineral measurement
Oligoclase	66.8	35.3	90.0	J. M. Brown, Angel, and Ross (2016), mineral measurement
”Average” matrix	35.7	33	75.7	Vernik (1997), empirical
”Average” feldspar	37.5	15	39.7	Mavko et al. (2009), empirical

The indentation modulus is related to the S the is unloading indentation stiffness $S = (dP/dh)$ by the equation

$$M \stackrel{\text{def}}{=} \frac{\sqrt{\pi}}{2} \frac{S}{\sqrt{A_c}}, \quad (4.3)$$

where A_c is the contact area, extrapolated from the maximum penetration depth h_{max} using the relation $A_c = 24.5h_{max}^2$ adapted to the geometry of Berkovitch-type indenters (Fischer-Cripps & Nicholson, 2004).

Young's moduli E can then be calculated from the indentation moduli according to

$$\frac{1}{M} = \frac{1 - \nu^2}{E} + \frac{1 - \nu_i^2}{E_i}. \quad (4.4)$$

In this study we took $E_i = 1220\text{GPa}$ and $\nu_i = 0.06$, for the indenter properties, according to Klein and Cardinale (1992) and Fischer-Cripps and Nicholson (2004) for diamond material. Calculation of E from M requires the knowledge of the mineral Poisson's ratio, which cannot be obtained from indentation tests. We assumed a constant Poisson's ratio of 0.10 for quartz (Pabst & Gregorová, 2013), 0.28 for albite (Christensen, 1996) and 0.29 for microcline and oligoclase (Christensen, 1996), even though this value will likely vary from measurement to measurement even within a single mineral phase.

Localisation of the grains and mineral of interest was performed using the optical images (that allows choosing grains without cracks) and the TIMA maps (that allows choosing grain with mineralogy of interest, namely quartz and three different types of feldspar identified: albite, oligoclase and microcline). Then, an optical microscope used in reflection mode and synchronised with the nano-indenter, helped focus the nano-indentation tip on the chosen zone of interest (Figure 4.6). Young's modulus map shows that the mineral moduli of grains in S60 are very similar to the values measured with mineral crystal, and higher than the empirical values. In the effective elastic moduli estimation, we will use the mineral moduli measured on crystals from literatures. For quartz, we will use bulk and shear moduli 37 and 44GPa, respectively. The feldspar moduli of Bentheimer is chosen to be the moduli of microcline in Table 4.1. The feldspar moduli of S60 are averaged using Voigt-Reuss-Hill model (Hill, 1952) based on the percentage of different kinds of feldspar from TIMA in Figure 4.2 and the crystal moduli in Table 4.1.

The application of nano-indentation to clay and pyrite is challenging due to their small particle size compared to the indenter, and thus we will use literature mineral moduli for simulations. Clay in Bentheimer sandstone is mainly kaolinite (Peksa et al., 2015),

and the moduli of clay are set to the values from laboratory measurements on kaolinite in Vanorio et al. (2003) (12GPa for bulk modulus and 6GPa for shear modulus). Clay minerals in S60 are more diverse, and empirical “mixed clay” values (bulk modulus 21GPa, shear modulus 7GPa) will be used (Tosaya, 1982). The pyrite moduli are chosen to be 147.4GPa for bulk modulus and 132.5GPa for shear modulus (Simmons & Birch, 1963).

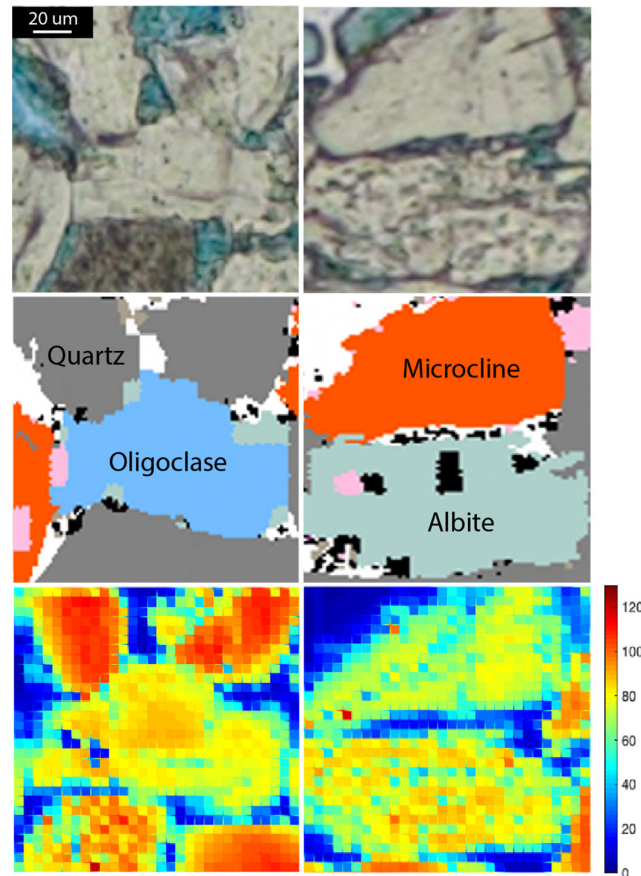


Figure 4.6 Young’s modulus map derived from nano-indentation (third row), guided by optical microscopy images (first row) and TIMA maps (second row) of S60.

4.3 Micro-CT image processing, segmentation and grain contact reconstruction

Micro-CT images (Figure 4.4) were imported into AVIZO software for the following processing. The dimension of the original micro-CT image is around 2000^3 voxels, which needs to be further reduced to 1200^3 when the cylindrical scan is cut into cube for processing and computation (Figure 4.7). We used the processing and multi-mineral segmentation workflow developed in Chapter 2 to suppress noise, segment clay and feldspar from the image. Pyrite in S60 appears in very bright colour due to

the high density, which can be segmented with greyscale thresholding with manually picked threshold value. Watershed separation was used to generate grain contact of one voxel thick (Saenger, Lebedev, et al., 2016). Contact thickness can be controlled by first resampling image to low resolution (larger voxel size), and reconstructing the contact with watershed separation. The contact phase was then resampled back to the original resolution and included as a separate phase in the processed labels. Here, we used 2 μ m thick contact resulting in the contact volume fraction similar to the weak bound water percentage from the NMR measurements. Finally, we have a five-phase label (pore, quartz, clay, feldspar and contact) for Bentheimer sample and six-phase label (pore, quartz, clay, feldspar, pyrite and contact) for S60 sample (Figure 4.7).

The porosity values estimated from the segmented labels are 24.58% for Bentheimer sample and 16.56% for S60 sample, which are very different from the estimated resolvable porosity from the laboratory measurements on core plugs (20.81% for Bentheimer sample and 17.64% for S60 sample). This is due to the scale difference and heterogeneity of the samples. To achieve a reasonable match between the image and the laboratory sample, we select a 600³ voxel subsample from the 1200³ voxel label with the porosity of 20.81% for Bentheimer sample and 17.64% for S60 sample. The selection is conducted by iterating the 1200³ voxel sample with a 600³ voxel fixed boundary until the subsample with the required porosity is located. This subsample will be used for the following study.

4.4 Grain contact moduli inversion

We used the combination of a range of contact bulk moduli (0.1, 1, 5, 20 and 50GPa) and shear moduli (0.1, 1, 5, 20 and 50GPa) to do 5 \times 5 effective elastic moduli computation using the 600³ voxel image set of Bentheimer and S60 sample. Effective elastic moduli were computed using finite-element method, treating each voxel as a trilinear finite element (Arns et al., 2002). The computed results gave a 5 \times 5 grid of the mapping from the contact moduli to effective moduli. To compensate for the incapability of limited mesh density to describe the rapid stress changes at grain contact (Liang, Glubokovskikh, Gurevich, Lebedev, & Vialle, 2020b), the labels of two samples were resampled from 600³ to 1200³ voxel (voxel edge length from \sim 1 μ m to \sim 0.5 μ m) and the effective moduli grid was computed again based on the 1200³ voxel image set. Then, a linear extrapolation of each corresponding grid point to zero

voxel edge length was conducted to compensate for the mesh density limitation. The extrapolated computed effective elastic moduli are shown in Figure 4.8.

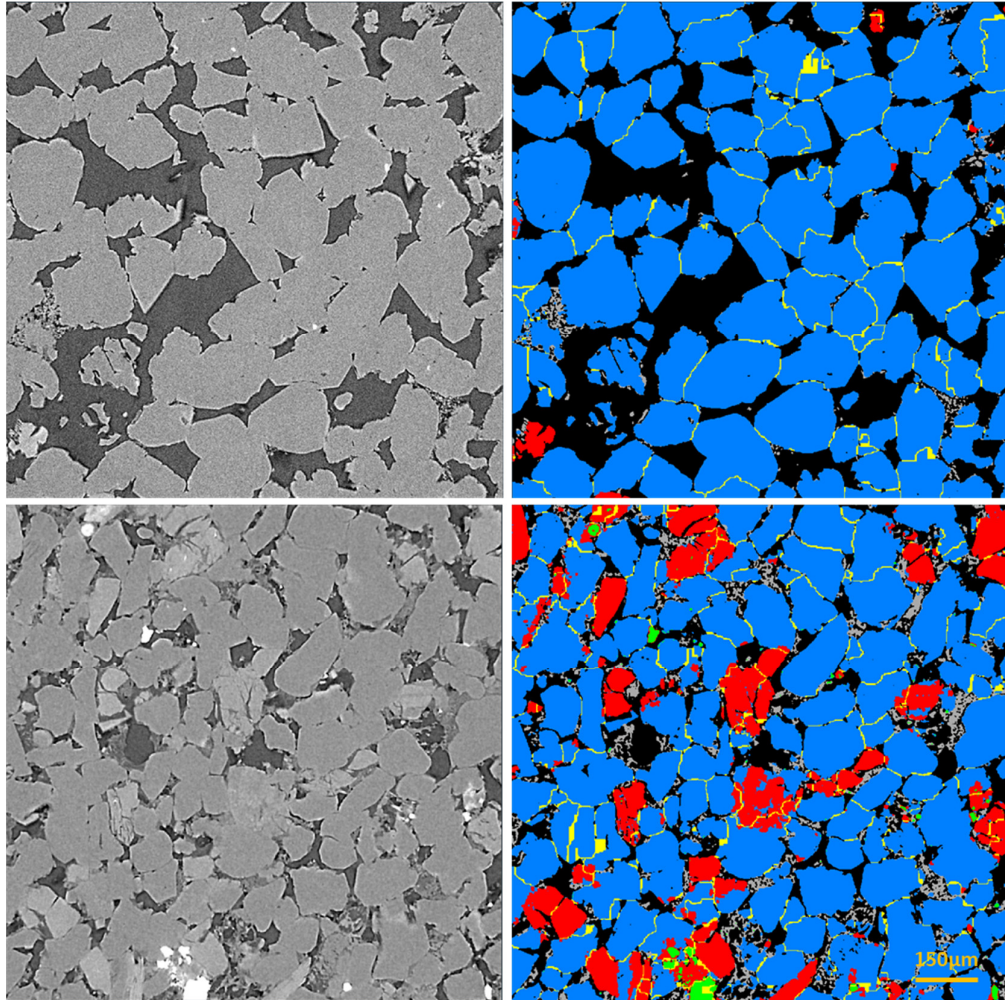


Figure 4.7 Greyscale micro-CT images (left) and processed labels (right). Bentheimer and S60 sample images are shown in each row. In the processed label images, pore, quartz, clay, feldspar, pyrite and reconstructed grain contacts are labelled in black, blue, grey, red, green and yellow, respectively.

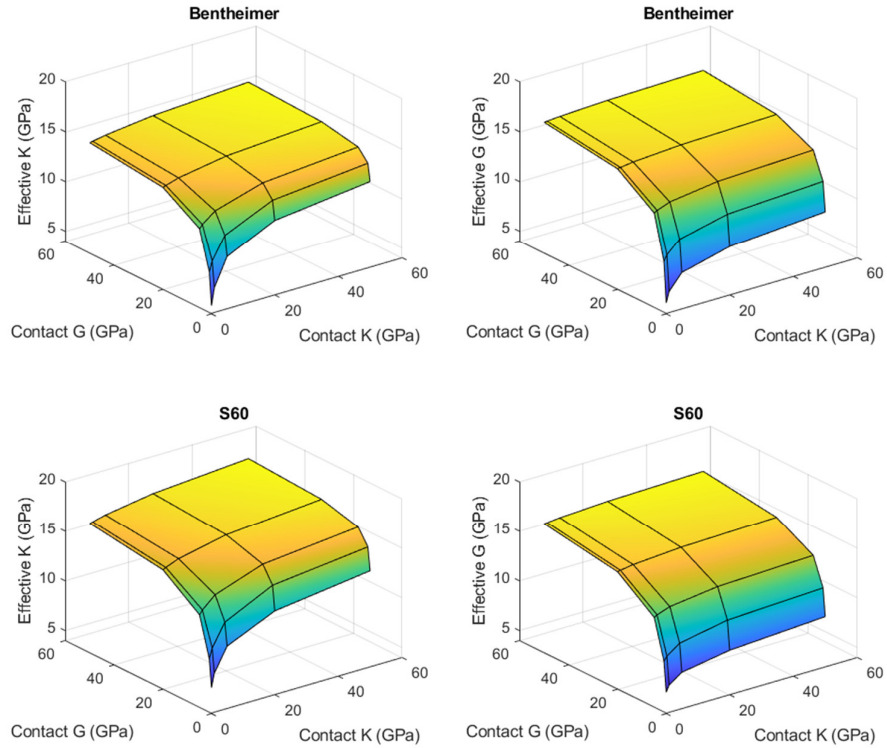


Figure 4.8 Effective moduli of Bentheimer and S60 sample based on the varying contact moduli. The effective moduli are extrapolated to zero voxel edge length using computed moduli from image set with the voxel edge length of $\sim 1\mu\text{m}$ and $\sim 0.5\mu\text{m}$.

We further interpolate the effective moduli surface with 0.1×0.1 GPa contact bulk and shear moduli grid using “Modified Akima piecewise cubic Hermite” method (Akima, 1970). Then, we are able to search for the contact stiffness that leads to the effective moduli matching each ultrasonic measurement as an inversion process. The criteria is to minimise $(K_{grid} - K_{measure})^2 + (G_{grid} - G_{measure})^2$ (Figure 4.9). The results expressed as stiffness values of contact for two samples in different pressure conditions shown in Figure 4.10. The inverted contact stiffness values are significantly smaller than the sandstone matrix for both samples. Also, Bentheimer has stiffer contact and shows less pressure dependency compared with S60.

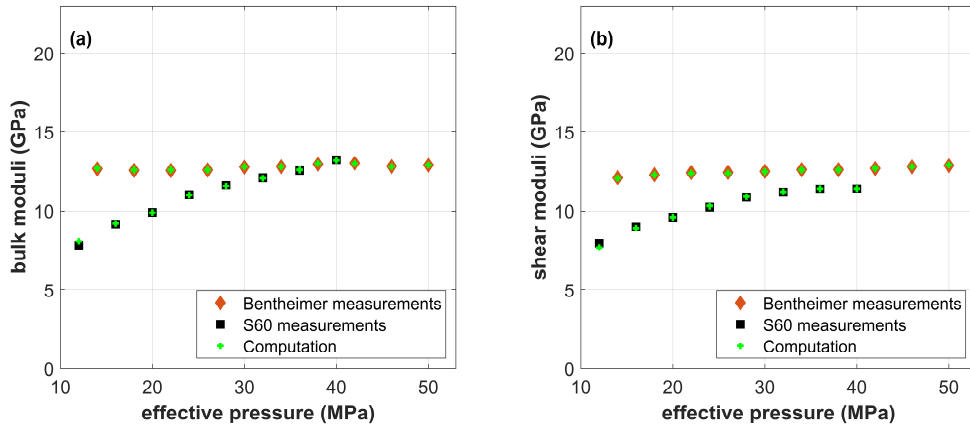


Figure 4.9 The correspondence between elastic moduli derived from laboratory measurements and the best-matching interpolated computed effective moduli.

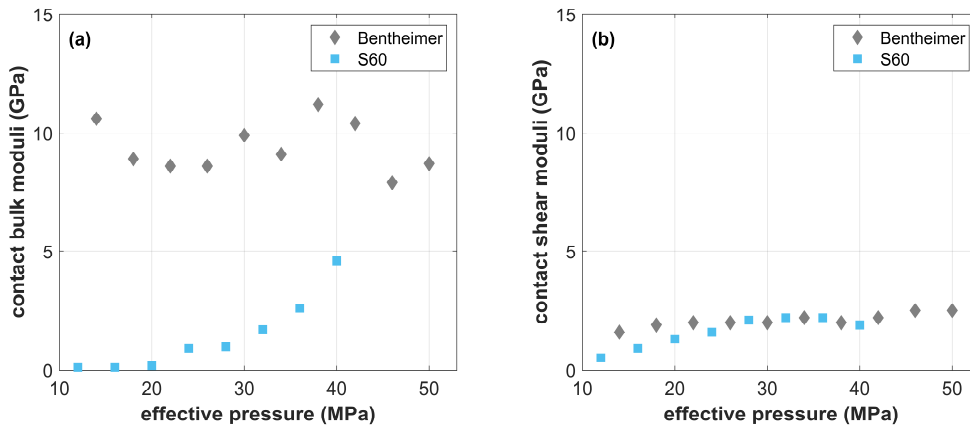


Figure 4.10 Inverted contact stiffness from ultrasonic measurements.

4.5 Discussion

In this chapter, a well-constrained DRP workflow was applied to understand the grain contact stiffness. It should be noted that this workflow assumes that millimetre scale sample used for micro-CT image scanning are representative of the centimetre scale sample used for ultrasonic measurements. In the selection of the matching image set, resolvable porosity of the image set was used as a reference to select a subsample from the larger image. It can be expected that the computed elastic moduli of subsamples with similar porosity still vary within a certain range, even for Bentheimer sandstone, which is relatively homogeneous and with simple mineralogy (see Chapter 2). The variance could result from the mineralogy difference in subsamples. This uncertainty can be reduced by using more subsamples of large image to generate a trend of

computed elastic moduli to compare with ultrasonic measurements. However, it will be very computational expensive to compute an effective moduli grid with varying contact stiffness for many subsamples.

Nano-indentation showed that the local grain stiffness was closer to the elastic moduli measured from pure mineral crystal. However, nano-indentation is limited by the accuracy and the nature of providing only one of the two necessary elastic parameters. Thus, the mineral moduli from nano-indentation were not used for the DRP computation but used as a guide. We also note that there may be some nanoscale flaws inside grains, which may distort the mineral moduli, but it cannot be quantified with nano-indentation. This uncertainty of the mineral stiffness may have been included in our inverted grain contact moduli.

In the DRP workflow, the computed moduli should be independent of boundary conditions, that is, the parts near the boundary should be small compared to the whole sample volume. As the computation tests in Chapter 2 show, the boundary effect may increase the computed moduli by 1-2 percent, which is a minor effect. Hence, the boundary effect has not been corrected in this study.

4.6 Conclusions

By treating grain contact as a separate phase, DRP workflow was used to infer the stiffness of grain contact of a Bentheimer sandstone and a real reservoir sandstone in different pressures. Every step of our DRP workflow was carefully constrained to derive the grain contact moduli representing more about the properties of the contact, instead of incorporating the uncertainties of digital rock physics setups. To achieve this, we investigated the unresolved soft pores with Nuclear Magnetic Resonance measurements, as well as constrained mineral moduli with nano-indentation and TIMA. The more appropriate mineral moduli were assigned to the multi-mineral labels segmented with the advanced segmentation workflow. The stiffness differences of grain contact in different cementation and pressure condition are now quantified. The inverted contact moduli can be used as a reference for setting up the grain contact stiffness in DRP study of other sandstone samples to include the cementation and pressure effect in elastic properties estimation, so the predictive power of DRP is strengthened.

Chapter 5 Multi-mineral segmentation of micro-CT images using a convolutional neural network

5.1 Introduction

The volume fractions and spatial distributions of different rock constituents are critical information for estimating effective properties of rocks (Dræge et al., 2006; Torquato & Haslach Jr, 2002). Micro X-ray-Computed Tomographic (micro-CT) can provide 3D representation of rocks in greyscale values, which result from the X-ray absorption coefficients of each component (Bultreys et al., 2016; Maire & Withers, 2014). Volume fractions and spatial distributions of different rock constituents can be potentially extracted from micro-CT images through the segmentation process. However, this is a challenging task and even considered ‘notorious’ (Schlüter et al., 2014).

The most obvious method of segmentation is through setting global threshold values on the greyscale histogram of the whole micro-CT image. However, greyscale values of different minerals can often overlap. First, the greyscale values of a mineral are distributed within a range. This range may be larger than the difference between mean greyscale values of two minerals. Second, the random noise, which is very common in micro-CT images, makes the greyscale value of some small dotted parts inside a phase fall into the range of another mineral. Third, due to limited resolution, voxels on grain boundaries may include more than one phase, so that the effective greyscale value may fall into the greyscale range of another mineral. As a result, the segmentation of micro-CT images with global greyscale thresholds are not able to generate satisfactory multi-mineral labels (Liang, Gurevich, et al., 2020).

In contrast to the global thresholding method, local adaptive methods can further account for the local variations of greyscale value. In a popular local adaptive method named watershed (Roerdink & Meijster, 2000), only zones with the most distinctive greyscales are selected as markers with global thresholding method, leaving the more ambiguous areas undefined. Then, markers grow like water emerging until they meet at the zones with high greyscale gradient, then the whole image is segmented. However, with the complexity of natural rocks and the artefacts of micro-CT scanning, it is even challenging to select appropriate markers (Liang, Gurevich, et al., 2020). Due to these challenges, micro-CT image analysis is often restricted to two-phase

segmentation, lumping all the mineral phases into one solid phase. This simplification can induce significant systematic errors in the subsequent effective property estimation (Ahmed et al., 2017; Ahmed et al., 2019; Andr a et al., 2013a; Saenger, Lebedev, et al., 2016; Shulakova et al., 2013).

In Chapter 2, we developed a robust segmentation workflow that effectively detected quartz, feldspar and clay minerals from micro-CT images of Bentheimer sandstones, taking advantage of both X-ray density and morphology features of different minerals (Figure 5.1). This workflow combines the benefits of different methods, such as mathematical morphology filters, global thresholding and watershed segmentation algorithms. However, this workflow is time-consuming, as some of its components require interactive parameter adjustments.

Several recent studies suggest that multi-mineral segmentation can be automated using convolutional neural networks (CNN) (Karimpouli & Tahmasebi, 2019; Wang et al., 2020). In any applications of neural network, a critical part is “ground truth” or labeled data. In previous applications of CNN on micro-CT segmentation, significant efforts were devoted to prepare the labeled data. Karimpouli and Tahmasebi (2019) semi-manually segmented only 20 slices of micro-CT images of a sandstone, because the segmentation of each slice required a long time. Then, they augmented the manually segmented images with stochastic image generator algorithm. However, the generated images are very similar to the original ones with limited new mineral features included, which limits the amount of information to be learnt by their CNN. Wang et al. (2020) scanned a mini-plug for micro-CT images and then selected the middle part of the image to create two surfaces. Then, they scanned one surface with Quantitative Evaluation of Minerals by SCANning electron microscopy (QEMSCAN) to automatically generate a mineral map. After that, this 2D QEMSCAN image was used to guide the multi-mineral segmentation of 3D micro-CT using a local adaptive segmentation method. The 3D labels offered more realistic varieties of mineral phases for training than stochastic images generated from 20 slices. However, this label inherited the segmentation errors from QEMSCAN and the local adaptive segmentation method. Moreover, these studies tested the prediction of the CNN models based on sub-images from the same dataset. Ideally, trained CNN models

should show effectiveness and robustness on a separate dataset (creating the so-called blind test).

In this chapter, we combine the advantages of the effective but laborious multi-mineral segmentation workflow developed in Chapter 2 and the intelligence of a CNN model. We segment micro-CT images of three Bentheimer sandstone samples with the multi-mineral segmentation workflow developed in Chapter 2. Based on two micro-CT images and the corresponding segmented labels, we train a CNN model with U-net architecture. Then, the trained model is used to segment all three sets of micro-CT images automatically, including the third one, which has not been used in the training process. The segmented labels with segmentation workflow and CNN model are compared and evaluated. For the third set of micro-CT images, the segmented multi-mineral labels with CNN model can achieve an accuracy of ~97% and the process takes only ~10 minutes.

5.2 Micro-CT images of a Bentheimer sandstone

Three cylindrical mini-plugs of Bentheimer samples (named sample A, B and C) were scanned with 3D X-ray microscope VersaXRM 500 (XRadia-Zeiss) with the similar scanning settings. In micro-CT images of sample A (Figure 5.1), quartz can be clearly recognized as the most abundant grain. Also, feldspar is distinguishable by a slightly brighter colour than quartz, as well as possibly corroded and fractured structure. Clay appears as much smaller particles around bigger grains or gathering as clusters in the pore space. Although these minerals have clear visual patterns according to the greyscale or morphology characteristics, the greyscale histogram of the 3D micro-CT images can only show two categories: pore and solid. The segmentation of greyscale micro-CT images into multi-mineral labels appears a formidable task.

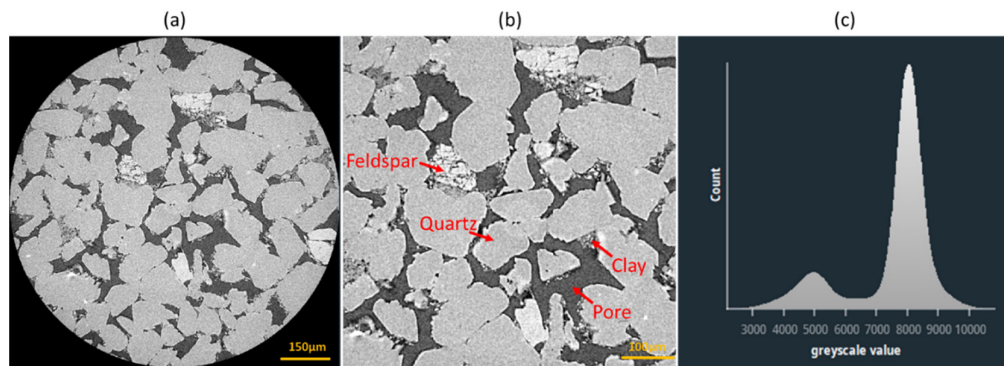


Figure 5.1 The cylindrical Bentheimer sandstone sample A is scanned (a) and the image is then cut into cube with the dimension of $624 \times 624 \times 624$ voxels (b) (only one slice is shown here). The greyscale histogram (c) of (b) only show two categories (pore with lower greyscale value and solid with higher greyscale value).

5.3 Multi-mineral segmentation through a workflow

The multi-mineral segmentation of micro-CT images from sandstones has recently been accomplished with a workflow developed in Chapter 2. This workflow takes advantage of a series of image processing and segmentation modules. For example, the greyscale values of clay particles are similar with other solid components (Figure 5.1). However, clay has a distinct feature in morphology. Clay particles are mixed with pores which are with lower greyscale value. By applying strong local averaging *median filter*, the greyscale of the blurred clay clusters will be lower than the other solid and higher than the pore. Thus, the clay parts can be separated with an *Otsu* global greyscale three-phase segmentation (Otsu, 1979), with other two phases as pore and other solid. Yet, the segmented clay part is mixed with the grain boundaries because grain boundaries were also blurred by *median filter* and now in medium greyscale. An *opening* algorithm (Haralick et al., 1987) is applied here to remove the grain boundaries according to their characteristics of disc shape. After this step, only the blurred clay part is reserved. Then, clay part is used as a *mask* for the unsmoothed *Otsu* two-phase labels to retrieve back the clay particles and micro pores. Furthermore, feldspar can also be segmented with a well-designed combination of image processing and segmentation modules. The whole segmentation workflow can be implemented in a commercial software called Avizo (Liang, Gurevich, et al., 2020).

As Figure 5.2 shows, different minerals are segmented as separate phases after an effective but laborious multi-mineral segmentation workflow. With the same workflow, we segment all the three sets of micro-CT images. In the next section, two sets of micro-CT greyscale images (sample A and B) and the corresponding segmented labels will be used to train a CNN model.

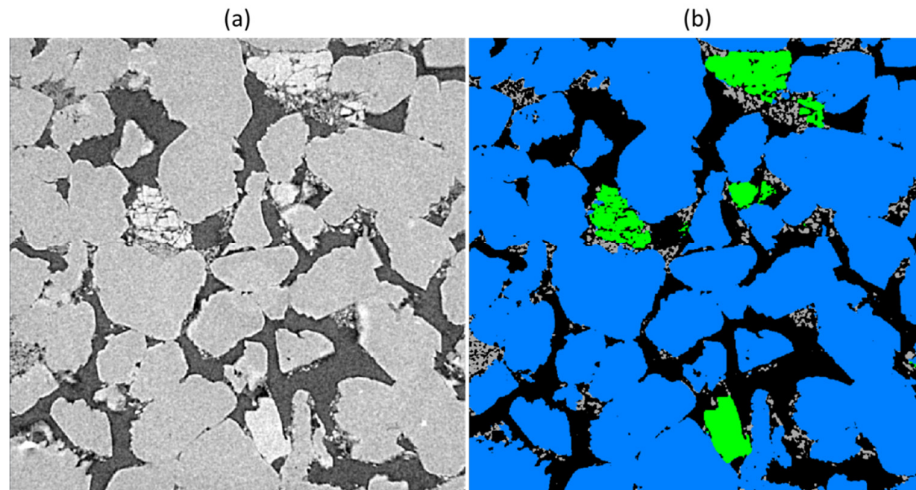


Figure 5.2 Original greyscale micro-CT image of Bentheimer sandstone sample A and the corresponding multi-mineral labels segmented with the workflow in Chapter 2 (only one slice is shown here). In the segmented images, pore, quartz, clay and feldspar are labelled in black, blue, grey and green, respectively.

5.4 Convolutional neural network setup

CNN is especially successful in tasks involving images, because convolution filtering significantly reduces the number of neurons while keeping the spatial structures in the image. CNN was first applied for image classification, where the image is processed to generate a single class label (Simonyan & Zisserman, 2014). By contrast, image segmentation tasks require localization, which means labelling each pixel or voxel. One popular CNN model, U-net (Ronneberger, Fischer, & Brox, 2015), was specifically developed for semantic segmentation of cells in images of biological tissues. U-net proposed to pass the input images through a contracting path - encoder, where the dimensionality of the images is reduced by building a deep representation for the context at each pixel, and an almost symmetric expanding path, decoder, that unravels the deep representation into the segmented image of the same size as the input. Moreover, long skip-connections allow the preservation of fine-scale features (Wang et al., 2020).

A U-net architecture for micro-CT segmentation is implemented using Keras (Chollet, 2015) with Tensorflow (Abadi et al., 2016) as the backend (Figure 5.3). Furthermore, the network is trained with *Adam* optimisation algorithm (Kingma & Ba, 2014) and *categorical cross entropy* as the loss function (Janocha & Czarnecki, 2017).

To prepare the data, we take the 3D greyscale images of three samples (each with $624 \times 624 \times 624$ voxels) and pre-process them in AVIZO. The greyscale images are first processed with *non-local means filter* to suppress the random noise (Buades et al., 2005). Then, *unsharp masking* is applied to recover the micro pores and cracks that are slightly blurred in the denoising process (Badamchizadeh & Aghagolzadeh, 2004). *Normalize greyscale* further reduces the greyscale difference of three datasets. More specifically, it ignores the 0.5 percent both at the beginning and the end of the greyscale histogram, as well as casting the medium part to the same updated greyscale range.

For the model training, we take the preprocessed 3D greyscale images of sample A and B, as well as the corresponding labels segmented with multi-mineral segmentation workflow. Each cube generates 624 2D slices with each combination of two coordinates, so the total number of 2D images for training from sample A and B is 3744 ($624 \text{ slices} \times 3 \text{ combinations of coordinates} \times 2 \text{ datasets}$). To avoid overfitting, randomly selected 20% of training images are used as the validation dataset. The training dataset is further augmented with image rotation, shearing, zooming and flipping to increase the variety of mineral morphology (Shorten & Khoshgoftaar, 2019). The preprocessed 3D greyscale image of sample C is divided into 624 slices of 2D images for the testing the trained model afterwards.

We set the training stopping criteria as the validation loss not decreasing in 10 epochs. In a random sequence, ten slices of greyscale images and the corresponding labels are fed into the network as a batch. After 37 epochs, the training process is stopped (Figure 4) and the trained model is saved as a file in the disk. The training computation does not require advanced hardware, and is done on a common CPU (Intel Xeon W-2123). The whole process takes ~68 hours, but can be significantly accelerated with a modern GPU.

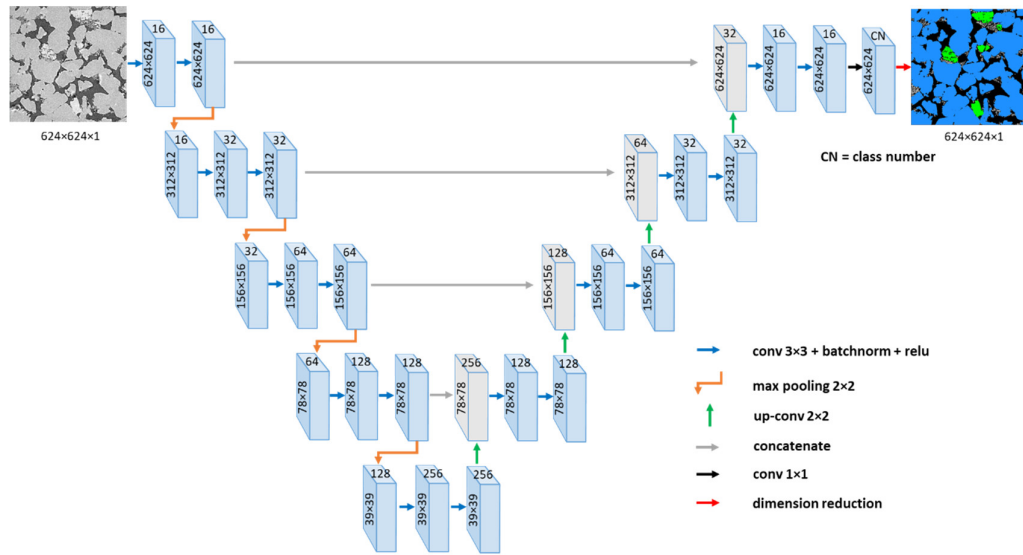


Figure 5.3 U-net architecture. The feature channel number is denoted on top of each box, and the dimension of image is shown on the left side of the box. The total parameter number in this structure is 2,164,356, with 2,161,412 of them trainable.

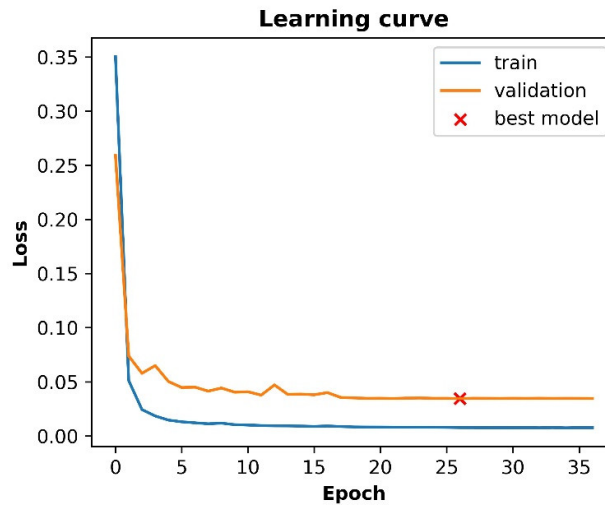


Figure 5.4 Learning process of CNN model for multi-mineral segmentation.

5.5 Results

The trained model is used to segment all the 2D slices of micro-CT images from three samples (Figure 5.5). We measure the consistency between labels segmented with multi-mineral workflow and the CNN model. As previous studies (Karimpouli & Tahmasebi, 2019; Wang et al., 2020), we estimate the accuracy, which is defined as the ratio of the number of correct labels to the total number of voxels. However, accuracy has a tendency to overlook the phase with a small percentage. For example,

if a rock consists of 99% quartz and 1% clay, labelling all pixels as quartz will achieve an accuracy of 99%. In our dataset, the percentages of clay and feldspar are significantly lower than those of quartz and pores, so accuracy is not very informative. We will also use another metric called F1-score, which is more suited for unbalanced datasets (Goutte & Gaussier, 2005).

The accuracy and F1-score values of the whole image and each mineral phase are shown in Table 5.1a. The consistency between labels of sample C from the segmentation workflow and CNN model is mostly only slightly lower than those of sample A and B, which were used in the model training and validation process. Also, for all three samples, phase percentages from the segmentation workflow and CNN model are consistent (Table 5.1b). This indicates that the CNN model successfully replicates the segmentation workflow.

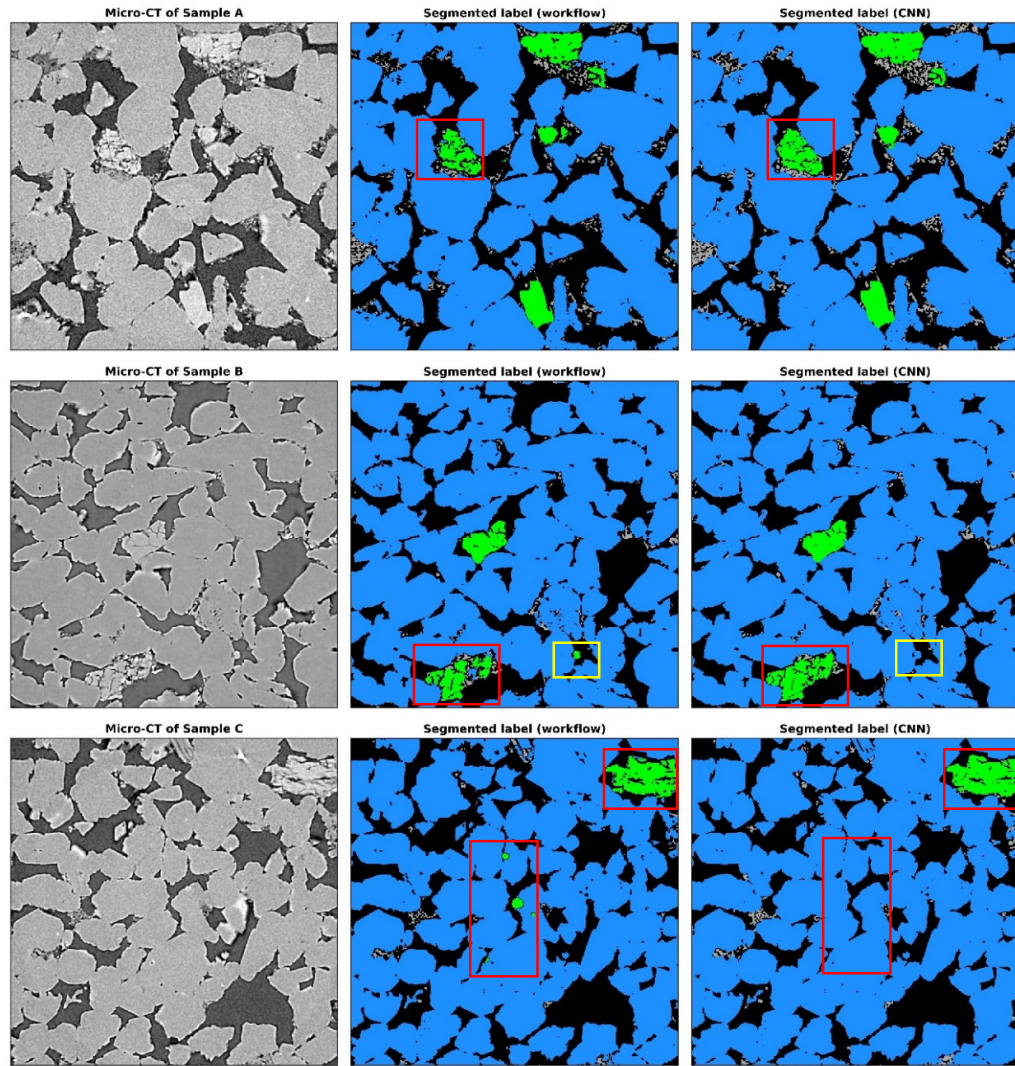


Figure 5.5 Comparison between labels from segmentation workflow and CNN model. Micro-CT images of three samples are shown in each row respectively. In the segmented images, the clay (grey) segmented by the CNN model is more consistent with human judgement. Also, the CNN model suppresses random errors in the labels from the segmentation workflow, especially for feldspar (red rectangles). However, a possible small feldspar grain is recognized by the segmentation workflow, but overlooked by the CNN model (yellow rectangle).

5.6 Discussion

The advantage of an effective but laborious segmentation workflow and CNN model are combined in this study. It should be noted that the labels from the segmentation workflow are not perfect, so that the metrics in Table 5.1 quantifies the agreement between the CNN labeled images, not with the exact distribution of the minerals. We found that the predicted labels even outperform the training labels in certain situations.

First, the clay segmented by the CNN model is more consistent with the human judgement. Secondly, the CNN model suppresses random errors in the labels from the segmentation workflow, especially for feldspar (Figure 5.5). The improvement means that the CNN model has the ability to learn the statistic characteristics of minerals from imperfect labels and does not stick to the random errors in the training labels. The minerals with smaller percentages show higher accuracy but lower F1-score. From the demonstration in Figure 5.5, it is clear that the F1-score provides better quantification of the difference between segmented labels from the segmentation workflow and CNN model.

Table 5.1 CNN model segmentation statistics

a) CNN model performances measured with accuracy (left) and F1-score (right).

	Sample A	Sample B	Sample C
Pore	0.975/0.932	0.979/0.952	0.977/0.952
Quartz	0.978/0.985	0.979/0.985	0.974/0.982
Clay	0.986/0.687	0.996/0.658	0.993/0.604
Feldspar	0.997/0.927	0.997/0.910	0.997/0.849
Overall	0.965/0.881	0.974/0.876	0.969/0.846

b) Phase percentage from segmentation workflow (left) and CNN model (right).

	Sample A	Sample B	Sample C
Pore	0.1958/0.1967	0.2336/0.2341	0.2531/0.2538
Quartz	0.7540/0.7537	0.7390/0.7387	0.7236/0.7246
Clay	0.0280/0.0275	0.0080/0.0074	0.0099/0.0105
Feldspar	0.0222/0.0222	0.0194/0.0199	0.0134/0.0110

The segmentation of CNN model is not always outperforming the segmentation workflow. For example, in the lower-right part of sample B (Figure 5.5), a possible small feldspar grain is recognized by the segmentation workflow, but overlooked by the CNN model. This error may be due to the large variety of feldspar morphology and the lack of training data due to the small percentage of the feldspar.

The segmentation workflow is conducted in 3D, while CNN model is working on 2D slices. In 2D, a tip of quartz or feldspar can be similar to a clay particle in morphology.

However, the slight greyscale differences are successfully captured by the CNN model, so the 2D artifacts are not obvious in the segmentation results (Figure 5.5).

The segmentation workflow requires several hours of interactive processing, while running a trained CNN model takes only ~10 minutes for the whole micro-CT images of a sample. Furthermore, the segmentation results from CNN model can be less affected by human bias, which is a significant advantage for reliable physical properties estimation in a systematic study (Cui, Cao, Liu, Zhu, & Jia, 2021; Saxena et al., 2017).

5.7 Conclusions

This study shows a very encouraging result in a multi-mineral micro-CT segmentation area. It demonstrates that minerals that can be visually identified may also be successfully segmented automatically with artificial intelligence. The prerequisite of this success is an elaborately designed interactive segmentation workflow, which takes advantage of the features of a mineral in greyscale and morphology at the same time. This multi-mineral segmentation workflow appears to provide more accurate and abundant labeled data for the training of a CNN model than previous studies. After the CNN model was trained with the segmented labels from this workflow, it learned the statistical greyscale and morphology features of different minerals. Moreover, the CNN model even improved the segmentation by suppressing random errors in the training labels. The application of the trained model on a new set of micro-CT images showed the effectiveness and efficiency of CNN model in the multi-mineral segmentation task. In summary, the results are very promising but obviously three samples are insufficient to produce definitive conclusions. Future work on many samples of different rocks is required to validate these conclusions and establish quantitative measures of segmentation accuracy.

Chapter 6 Conclusions and future work

6.1 Conclusions

In this thesis, we built and improved a digital rock physics workflow for estimation of elastic moduli based on micro-CT images of sandstones, and used this workflow to help understand the relation between pore scale characteristics and macroscale effective elastic moduli.

First, we tried to build a DRP workflow based on Bentheimer sandstone, which is relatively homogeneous and with simple mineralogy. We performed a set of simulations for images segmented into solid and pore constituents. We found that the boundary conditions induced size dependence into the computed effective moduli, which could be removed by an exponential correcting function. The insufficient resolution could be fixed by linear extrapolation to a desired voxel size based on the computations for images scanned with different resolution. Then, we developed a multi-stage four-phase segmentation graph that targets feldspar and clay minerals. In order to do so, we applied a combination of mathematical morphology filters, Otsu and watershed segmentation algorithms. Numerical simulations indicated that the appropriate segmentation graph and compensation for scanning parameters might reduce significantly the discrepancy between the measurements and computed moduli. Eventually, the computed bulk modulus for multi-mineral matrix agreed well with the ultrasonic measurements at 40MPa, where the effect of unresolved compliant pores was small. The shear modulus remained overestimated. The discrepancy was corrected with an empirically determined matrix moduli. This DRP workflow provided accurate velocity trends with porosity and clay content based on two samples of Bentheimer sandstone. Traditionally, such a relationship for quantitative interpretation would require ultrasonic measurements on dozens of samples and thin sections/XRD.

Secondly, we investigated the pressure effect on high-resolution micro-CT images of a reservoir sandstone and on elastic properties computed from these images. The X-ray transparent pressure cell allowed micro-CT scanning at confining pressures of up to 36MPa. The images produced at different pressures were very close to each other and the differences were almost invisible to a naked eye. To detect these differences, we designed a slice matching workflow. Application of this workflow to our images showed that the same physical part of the studied sample occupied the space of

1255×1021×1620 voxels at 0MPa (without residual stress), 1253×1019×1616 voxels at 0MPa (with residual stress), 1250×1017×1613 at 20MPa, and 1252×1017×1613 at 36MPa. The detected deformation was larger from 0MPa to 20MPa, than from 20MPa to 36MPa. The effect of stress release was also detected by comparing the images at 0MPa with and without residual stress. The derived static bulk modulus from deformation from 0MPa to 20MPa is 2.78GPa, which was consistent with literature values. The porosity change detected from segmented labels was consistent with the value derived from static modulus using poroelastic theory. The images scanned at different pressures were used to compute the effective elastic moduli. The difference between the computed moduli was much smaller than the difference between the ultrasonic measurements. This showed, consistent with previous studies, that micro-CT imaging could not resolve the geometry of grain contacts responsible for the pressure effect on the elastic properties. The accuracy improvement of the estimated elastic properties from images scanned at higher pressures was negligible. One way to overcome this limitation is to parameterize the pressure dependency of the contact stiffness indirectly.

Thirdly, by treating grain contact as a separate phase, DRP workflow was used to infer the stiffness of grain contact of a Bentheimer sandstone and a real reservoir sandstone in different pressures. Every step of our DRP workflow was carefully constrained to derive the grain contact moduli representing more about the properties of the contact, instead of incorporating the uncertainties of digital rock physics setups. To achieve this, we investigated the unresolved soft pores with Nuclear Magnetic Resonance measurements, as well as constrained mineral moduli with nano-indentation and TIMA. The more appropriate mineral moduli were assigned to the multi-mineral labels segmented with the advanced segmentation workflow. The stiffness differences of grain contact in different cementation and pressure condition are now quantified. The inverted contact moduli can be used as a reference for setting up the grain contact stiffness in DRP study of other sandstone samples to include the cementation and pressure effect in elastic properties estimation, so the predictive power of DRP is strengthened.

Fourthly, we presented a very encouraging result in a multi-mineral micro-CT segmentation area. It demonstrated that minerals that can be visually identified, might

also be successfully segmented automatically with artificial intelligence. The prerequisite of this success was an elaborately designed interactive segmentation workflow, which took advantage of the features of a mineral in greyscale and morphology at the same time. This multi-mineral segmentation workflow provided more accurate and abundant labeled data for the training of a CNN model than previous studies. After the CNN model was trained with the segmented labels from this workflow, it learned the statistical greyscale and morphology features of different minerals. Moreover, the CNN model even improved the segmentation by suppressing random errors in the training labels. The application of the trained model on a new set of micro-CT images proved the effectiveness and efficiency of CNN model in the multi-mineral segmentation task.

6.2 Future work

Digital rock physics can give effective elastic moduli based on realistic microscopic information. Where there is no core available for producing micro-CT images, theoretical rock physics models are still valuable for modelling the relationship between elastic moduli and petrophysical properties. Our well-developed digital rock physics workflow can be used as a reference for evaluating and improving rock physics models, as well as investigating how to constrain the input parameters of these models.

The natural heterogeneity of rock may affect the correspondence of the elastic properties estimated based on millimetre scale samples for micro-CT scanning and seismic data at metre scale. It will be very interesting to conduct a more extensive digital rock physics study with more samples from a reservoir to understand the strategy to upscale the digital rock physics results. Moreover, thin sections are more common and cost-effective in the industry, and how to estimate elastic properties from thin section images will be an interesting study.

To establish applicability and accuracy of the convolutional neural network approach for micro-CT image segmentation, this technique should be tested on several different sandstone samples and samples of other rock types.

References

- Abadi, M., Agarwal, A., Barham, P., Brevdo, E., Chen, Z., Citro, C., . . . Devin, M. (2016). Tensorflow: Large-scale machine learning on heterogeneous distributed systems. *arXiv preprint arXiv:1603.04467*.
- Adelinet, M., Fortin, J., Guéguen, Y., Schubnel, A., & Geoffroy, L. (2010). Frequency and fluid effects on elastic properties of basalt: Experimental investigations. *Geophysical Research Letters*, *37*(2).
doi:<https://doi.org/10.1029/2009gl041660>
- Ahmed, S., Müller, T. M., Liang, J., Tang, G., & Madadi, M. (2017). Macroscopic deformation moduli of porous rocks: Insights from digital image pore-scale simulations. In *Poromechanics VI* (pp. 815-821).
- Ahmed, S., Müller, T. M., Madadi, M., & Calo, V. (2019). Drained pore modulus and Biot coefficient from pore-scale digital rock simulations. *International Journal of Rock Mechanics and Mining Sciences*, *114*, 62-70.
doi:<https://doi.org/10.1016/j.ijrmms.2018.12.019>
- Ajdukiewicz, J. M., & Lander, R. H. (2010). Sandstone reservoir quality prediction: The state of the art. *AAPG bulletin*, *94*(8), 1083-1091.
- Akima, H. (1970). A new method of interpolation and smooth curve fitting based on local procedures. *Journal of the ACM (JACM)*, *17*(4), 589-602.
- Al Ibrahim, M. A., Kerimov, A., Mukerji, T., & Mavko, G. (2018). Digital rocks with irregularly shaped grains: A simulator tool for computational rock physics. In *SEG Technical Program Expanded Abstracts 2018* (pp. 3698-3702): Society of Exploration Geophysicists.
- Aliyeva, S., Alabbad, A., Daza, J. P., & Mukerji, T. (2017). *Elasticity, Electrical Conductivity and Permeability in Digital Rocks: A Comparative Study Using Simpleware, NIST, Comsol Multiphysics and Lattice-Boltzmann Algorithms*. Paper presented at the 51st US Rock Mechanics/Geomechanics Symposium.
- Amini, H. (2019). *A Review of Variability of the Effective Mineral's Elastic Moduli in Sandstones*. Paper presented at the 81st EAGE Conference and Exhibition 2019.
- Andrä, H., Combaret, N., Dvorkin, J., Glatt, E., Han, J., Kabel, M., . . . Madonna, C. (2013a). Digital rock physics benchmarks—Part I: Imaging and

- segmentation. *Computers & Geosciences*, 50, 25-32.
doi:<https://doi.org/10.1016/j.cageo.2012.09.005>
- Andrä, H., Combaret, N., Dvorkin, J., Glatt, E., Han, J., Kabel, M., . . . Madonna, C. (2013b). Digital rock physics benchmarks—Part II: Computing effective properties. *Computers & Geosciences*, 50, 33-43.
doi:<https://doi.org/10.1016/j.cageo.2012.09.008>
- Antiga, L., Ene-Iordache, B., Caverni, L., Cornalba, G. P., & Remuzzi, A. (2002). Geometric reconstruction for computational mesh generation of arterial bifurcations from CT angiography. *Computerized Medical Imaging and Graphics*, 26(4), 227-235. doi:[https://doi.org/10.1016/s0895-6111\(02\)00020-4](https://doi.org/10.1016/s0895-6111(02)00020-4)
- Arns, C. H., Knackstedt, M. A., Pinczewski, W. V., & Garboczi, E. J. (2002). Computation of linear elastic properties from microtomographic images: Methodology and agreement between theory and experiment. *Geophysics*, 67(5), 1396-1405. doi:<https://doi.org/10.1190/1.1512785>
- Arns, C. H., Madadi, M., Sheppard, A. P., & Knackstedt, M. A. (2007). Linear elastic properties of granular rocks derived from X-ray-CT images. In *SEG Technical Program Expanded Abstracts 2007* (pp. 1711-1715): Society of Exploration Geophysicists.
- AVIZO. (2019.3). Avizo User's Guide. *Thermo Fisher Scientific.*,
www.thermofisher.com.
- Avseth, P., Mukerji, T., & Mavko, G. (2010). *Quantitative seismic interpretation: Applying rock physics tools to reduce interpretation risk*: Cambridge university press.
- Bachrach, R., & Avseth, P. (2008). Rock physics modeling of unconsolidated sands: Accounting for nonuniform contacts and heterogeneous stress fields in the effective media approximation with applications to hydrocarbon exploration. *Geophysics*, 73(6), E197-E209. doi:<https://doi.org/10.1190/1.2985821>
- Badamchizadeh, M. A., & Aghagolzadeh, A. (2004). *Comparative study of unsharp masking methods for image enhancement*. Paper presented at the Third International Conference on Image and Graphics (ICIG'04).
- Bar-Kochba, E., Toyjanova, J., Andrews, E., Kim, K.-S., & Franck, C. (2015). A fast iterative digital volume correlation algorithm for large deformations.

Experimental Mechanics, 55(1), 261-274. doi:<https://doi.org/10.1007/s11340-014-9874-2>

- Bazaikin, Y., Gurevich, B., Iglauer, S., Khachkova, T., Kolyukhin, D., Lebedev, M., . . . Reshetova, G. (2017). Effect of CT image size and resolution on the accuracy of rock property estimates. *Journal of Geophysical Research: Solid Earth*, 122(5), 3635-3647. doi:<https://doi.org/10.1002/2016jb013575>
- Berryman, J. G. (1995). Mixture theories for rock properties. *Rock physics and phase relations: A handbook of physical constants*, 3, 205-228.
- Brown, J. M., Abramson, E., & Angel, R. (2006). Triclinic elastic constants for low albite. *Physics and Chemistry of Minerals*, 33(4), 256-265.
- Brown, J. M., Angel, R. J., & Ross, N. L. (2016). Elasticity of plagioclase feldspars. *Journal of Geophysical Research: Solid Earth*, 121(2), 663-675.
- Brown, W. L. (2013). *Feldspars and feldspathoids: structures, properties and occurrences* (Vol. 137): Springer Science & Business Media.
- Buades, A., Coll, B., & Morel, J.-M. (2005). *A non-local algorithm for image denoising*. Paper presented at the 2005 IEEE Computer Society Conference on Computer Vision and Pattern Recognition (CVPR'05).
- Bultreys, T., Boone, M. A., Boone, M. N., De Schryver, T., Masschaele, B., Van Hoorebeke, L., & Cnudde, V. (2016). Fast laboratory-based micro-computed tomography for pore-scale research: Illustrative experiments and perspectives on the future. *Advances in water resources*, 95, 341-351.
- Carmichael, R. S. (1989). *Practical handbook of physical properties of rocks and minerals* (Vol. 374): CRC press Boca Raton, FL.
- Cebal, J. R., & Löhner, R. (2001). From medical images to anatomically accurate finite element grids. *International Journal for Numerical Methods in Engineering*, 51(8), 985-1008. doi:<https://doi.org/10.1002/nme.205>
- Cheng, C., & Johnston, D. H. (1981). Dynamic and static moduli. *Geophysical Research Letters*, 8(1), 39-42. doi:<https://doi.org/10.1029/g1008i001p00039>
- Chollet, F. (2015). keras. In.
- Christensen, N. I. (1996). Poisson's ratio and crustal seismology. *Journal of Geophysical Research: Solid Earth*, 101(B2), 3139-3156.
- Cnudde, V., & Boone, M. N. (2013). High-resolution X-ray computed tomography in geosciences: A review of the current technology and applications. *Earth-*

Science Reviews, 123, 1-17.

doi:<https://doi.org/10.1016/j.earscrev.2013.04.003>

COMSOL. (v. 5.4.). COMSOL Multiphysics Reference Manual. *COMSOL Inc.*,
www.comsol.com.

Cotton, R., Tompsett, P., Smigaj, W., Kerim, G., & Agarwal, Y. (2016). *New Tools for Image-Based Meshing and Simulation for Digital Rock Physics*. Paper presented at the ANNUAL GENERAL MEETING OF THE GEOLOGICAL SOCIETY OF INDIA.

Cui, R., Cao, D., Liu, Q., Zhu, Z., & Jia, Y. (2021). VP and VS prediction from digital rock images using a combination of U-Net and convolutional neural networks. *Geophysics*, 86(1), MR27-MR37.

Dai, H., Shikhov, I., Li, R., Arns, J.-Y., & Arns, C. H. (2021). Mechanisms of Confining Pressure Dependence of Resistivity Index for Tight Sandstones by Digital Core Analysis. *SPE Journal*, 1-14. doi:
<https://doi.org/10.2118/205026-pa>

David, E., & Zimmerman, R. W. (2012). Pore structure model for elastic wave velocities in fluid - saturated sandstones. *Journal of Geophysical Research: Solid Earth*, 117(B7). doi:<https://doi.org/10.1029/2012jb009195>

de Paula, O. B., Pervukhina, M., Makarynska, D., & Gurevich, B. (2012). Modeling squirt dispersion and attenuation in fluid-saturated rocks using pressure dependency of dry ultrasonic velocities. *Geophysics*, 77(3), WA157-WA168.

Digby, P. (1981). The effective elastic moduli of porous granular rocks. *Journal of Applied Mechanics*, 48(4), 803-808.

Dræge, A., Johansen, T. A., Brevik, I., & Dræge, C. T. (2006). A strategy for modelling the diagenetic evolution of seismic properties in sandstones. *Petroleum Geoscience*, 12(4), 309-323. doi:<https://doi.org/10.3997/2214-4609-pdb.1.h036>

Dvorkin, J., Derzhi, N., Diaz, E., & Fang, Q. (2011). Relevance of computational rock physics. *Geophysics*, 76(5), E141-E153.
doi:<https://doi.org/10.1190/geo2010-0352.1>

Dvorkin, J., Nur, A., & Yin, H. (1994). Effective properties of cemented granular materials. *Mechanics of materials*, 18(4), 351-366.

- Eberhart-Phillips, D., Han, D.-H., & Zoback, M. (1989). Empirical relationships among seismic velocity, effective pressure, porosity, and clay content in sandstone. *Geophysics*, 54(1), 82-89. doi:<https://doi.org/10.1190/1.1442580>
- Eshelby, J. D. (1957). The determination of the elastic field of an ellipsoidal inclusion, and related problems. *Proc. R. Soc. Lond. A*, 241(1226), 376-396. doi:https://doi.org/10.1007/1-4020-4499-2_18
- Estévez, P. A., Tesmer, M., Perez, C. A., & Zurada, J. M. (2009). Normalized mutual information feature selection. *IEEE Transactions on neural networks*, 20(2), 189-201. doi:<https://doi.org/10.1109/tnn.2008.2005601>
- Fischer-Cripps, A. C., & Nicholson, D. (2004). Nanoindentation. Mechanical engineering series. *Appl. Mech. Rev.*, 57(2), B12-B12.
- Fjær, E. (2009). Static and dynamic moduli of a weak sandstone. *Geophysics*, 74(2), WA103-WA112.
- Garboczi, E. J. (1998). *Finite Element and Finite Difference Programs for Computing the Linear Electric and Elastic Properties of Digital Images of Random Materials* | NIST. Retrieved from
- García, X., & Medina, E. (2007). Acoustic response of cemented granular sedimentary rocks: molecular dynamics modeling. *Physical Review E*, 75(6), 061308.
- Glubokovskikh, S., Gurevich, B., Lebedev, M., & Mikhaltsevitch, V. (2015). *Stress-dependence of elastic properties of rock containing finite cracks with contacting surfaces*. Paper presented at the 2015 SEG Annual Meeting.
- Glubokovskikh, S., Gurevich, B., Lebedev, M., Mikhaltsevitch, V., & Tan, S. (2016). Effect of asperities on stress dependency of elastic properties of cracked rocks. *International Journal of Engineering Science*, 98, 116-125. doi:<https://doi.org/10.1016/j.ijengsci.2015.09.001>
- Goldberg, I., & Gurevich, B. (1998). A semi-empirical velocity-porosity-clay model for petrophysical interpretation of P-and S-velocities. *Geophysical Prospecting*, 46(3), 271-285. doi:<https://doi.org/10.1046/j.1365-2478.1998.00095.x>
- Goutte, C., & Gaussier, E. (2005). *A probabilistic interpretation of precision, recall and F-score, with implication for evaluation*. Paper presented at the European conference on information retrieval.

- Gurevich, B., Makarynska, D., de Paula, O. B., & Pervukhina, M. (2010). A simple model for squirt-flow dispersion and attenuation in fluid-saturated granular rocks. *Geophysics*, 75(6), N109-N120. doi:<https://doi.org/10.1190/1.3509782>
- Han, D.-h., Nur, A., & Morgan, D. (1986). Effects of porosity and clay content on wave velocities in sandstones. *Geophysics*, 51(11), 2093-2107. doi:<https://doi.org/10.1190/1.1442328>
- Haralick, R. M., Sternberg, S. R., & Zhuang, X. (1987). Image analysis using mathematical morphology. *IEEE Transactions on pattern analysis and machine intelligence*(4), 532-550. doi:<https://doi.org/10.1109/tpami.1987.4767941>
- Hashin, Z., & Shtrikman, S. (1963). A variational approach to the theory of the elastic behaviour of multiphase materials. *Journal of the Mechanics and Physics of Solids*, 11(2), 127-140.
- Hill, R. (1952). The elastic behaviour of a crystalline aggregate. *Proceedings of the Physical Society. Section A*, 65(5), 349.
- Hossain, M. M., Arns, J. Y., Liang, Z., Chen, Z., & Arns, C. H. (2019). Humidity effects on effective elastic properties of rock: An integrated experimental and numerical study. *Journal of Geophysical Research: Solid Earth*, 124(8), 7771-7791. doi:<https://doi.org/10.1029/2019jb017672>
- Huet, C. (1990). Application of variational concepts to size effects in elastic heterogeneous bodies. *Journal of the Mechanics and Physics of Solids*, 38(6), 813-841. doi:[https://doi.org/10.1016/0022-5096\(90\)90041-2](https://doi.org/10.1016/0022-5096(90)90041-2)
- Iassonov, P., Gebrenegus, T., & Tuller, M. (2009). Segmentation of X - ray computed tomography images of porous materials: A crucial step for characterization and quantitative analysis of pore structures. *Water Resources Research*, 45(9).
- Janocha, K., & Czarnecki, W. M. (2017). On loss functions for deep neural networks in classification. *arXiv preprint arXiv:1702.05659*.
- Joseph, P. M., & Spital, R. D. (1981). The exponential edge-gradient effect in x-ray computed tomography. *Physics in Medicine & Biology*, 26(3), 473. doi:<https://doi.org/10.1088/0031-9155/26/3/010>
- Kalo, K., Grgic, D., Auvray, C., Giraud, A., Drach, B., & Sevostianov, I. (2017). Effective elastic moduli of a heterogeneous oolitic rock containing 3-D

- irregularly shaped pores. *International Journal of Rock Mechanics and Mining Sciences*, 98, 20-32. doi:<https://doi.org/10.1016/j.ijrmms.2017.07.009>
- Kanit, T., Forest, S., Galliet, I., Mounoury, V., & Jeulin, D. (2003). Determination of the size of the representative volume element for random composites: statistical and numerical approach. *International Journal of solids and structures*, 40(13-14), 3647-3679. doi:[https://doi.org/10.1016/s0020-7683\(03\)00143-4](https://doi.org/10.1016/s0020-7683(03)00143-4)
- Karimpouli, S., & Tahmasebi, P. (2019). Segmentation of digital rock images using deep convolutional autoencoder networks. *Computers & Geosciences*, 126, 142-150.
- Kawakata, H., Cho, A., Yanagidani, T., & Shimada, M. (1997). The observations of faulting in Westerly granite under triaxial compression by X-ray CT scan. *International Journal of Rock Mechanics and Mining Sciences*, 34(3-4), 151. e151-151. e112. doi:[https://doi.org/10.1016/s1365-1609\(97\)00138-x](https://doi.org/10.1016/s1365-1609(97)00138-x)
- Kingma, D. P., & Ba, J. (2014). Adam: A method for stochastic optimization. *arXiv preprint arXiv:1412.6980*.
- Klein, C. A., & Cardinale, G. F. (1992). *Young's modulus and Poisson's ratio of CVD diamond*. Paper presented at the Diamond Optics V.
- Knackstedt, M. A., Latham, S., Madadi, M., Sheppard, A., Varslot, T., & Arns, C. (2009). Digital rock physics: 3D imaging of core material and correlations to acoustic and flow properties. *The Leading Edge*, 28(1), 28-33. doi:<https://doi.org/10.1190/1.3064143>
- Krief, M., Garat, J., Stellingwerff, J., & Ventre, J. (1990). A petrophysical interpretation using the velocities of P and S waves (full-waveform sonic). *The Log Analyst*, 31(06).
- Kuster, G. T., & Toksöz, M. N. (1974). Velocity and attenuation of seismic waves in two-phase media: Part I. Theoretical formulations. *Geophysics*, 39(5), 587-606.
- Lebedev, M., Wilson, M. E., & Mikhaltsevitch, V. (2014). An experimental study of solid matrix weakening in water - saturated Savonnières limestone. *Geophysical Prospecting*, 62(6), 1253-1265.
- Lebedev, M., Zhang, Y., Mikhaltsevitch, V., Inglauer, S., & Rahman, T. (2017). Residual trapping of supercritical CO₂: direct pore-scale observation using a

- low cost pressure cell for micro computer tomography. *Energy Procedia*, 114, 4967-4974. doi:<https://doi.org/10.1016/j.egypro.2017.03.1639>
- Liang, J., Glubokovskikh, S., Gurevich, B., Lebedev, M., & Vialle, S. (2020a). *An optimized digital rock physics workflow for elastic moduli estimation of sandstones with dispersed clay*. Paper presented at the Fifth EAGE Workshop on Rock Physics.
- Liang, J., Glubokovskikh, S., Gurevich, B., Lebedev, M., & Vialle, S. (2020b). The overestimated elastic moduli from digital rock images: Computational reasons. In *SEG Technical Program Expanded Abstracts 2020* (pp. 2505-2509): Society of Exploration Geophysicists.
- Liang, J., Gurevich, B., Lebedev, M., Vialle, S., Yurikov, A., & Glubokovskikh, S. (2020). Elastic moduli of arenites from micro - tomographic images—a practical digital rock physics workflow. *Journal of Geophysical Research: Solid Earth*, e2020JB020422. doi:<https://doi.org/10.1029/2020jb020422>
- Madadi, M., Jones, A. C., Arns, C. H., & Knackstedt, M. A. (2009). 3D imaging and simulation of elastic properties of porous materials. *Computing in Science & Engineering*, 11(4), 65-73. doi: <https://doi.org/10.1109/mcse.2009.110>
- Madhukar, B., & Narendra, R. (2013). *Lanczos resampling for the digital processing of remotely sensed images*. Paper presented at the Proceedings of International Conference on VLSI, Communication, Advanced Devices, Signals & Systems and Networking (VCASAN-2013).
- Madonna, C., Almqvist, B. S., & Saenger, E. H. (2012). Digital rock physics: numerical prediction of pressure-dependent ultrasonic velocities using micro-CT imaging. *Geophysical Journal International*, 189(3), 1475-1482. doi:<https://doi.org/10.1111/j.1365-246x.2012.05437.x>
- Madonna, C., Quintal, B., Frehner, M., Almqvist, B. S., Tisato, N., Pistone, M., . . . Saenger, E. H. (2013). Synchrotron-based X-ray tomographic microscopy for rock physics investigationsSynchrotron-based rock images. *Geophysics*, 78(1), D53-D64. doi:<https://doi.org/10.1190/geo2012-0113.1>
- Maire, E., & Withers, P. J. (2014). Quantitative X-ray tomography. *International Materials Reviews*, 59(1), 1-43. doi:<https://doi.org/10.1179/1743280413y.0000000023>

- Makarynska, D., Gurevich, B., Ciz, R., Arns, C. H., & Knackstedt, M. A. (2008). Finite element modelling of the effective elastic properties of partially saturated rocks. *Computers & Geosciences*, *34*(6), 647-657.
doi:<https://doi.org/10.1016/j.cageo.2007.06.009>
- Mavko, G., & Jizba, D. (1991). Estimating grain-scale fluid effects on velocity dispersion in rocks. *Geophysics*, *56*(12), 1940-1949.
doi:<https://doi.org/10.1190/1.1443005>
- Mavko, G., Mukerji, T., & Dvorkin, J. (2009). *The rock physics handbook: Tools for seismic analysis of porous media*: Cambridge university press.
- McSkimin, H., Andreatch Jr, P., & Thurston, R. (1965). Elastic moduli of quartz versus hydrostatic pressure at 25 and– 195.8 C. *Journal of Applied Physics*, *36*(5), 1624-1632.
- Mindlin, R. (1949). Compliance of elastic bodies in contact. *J. Appl. Mech., ASME*, *16*, 259-268.
- Mondol, N. H., Jahren, J., Bjørlykke, K., & Brevik, I. (2008). Elastic properties of clay minerals. *The Leading Edge*, *27*(6), 758-770.
doi:<https://doi.org/10.1190/1.2944161>
- Mori, T., & Tanaka, K. (1973). Average stress in matrix and average elastic energy of materials with misfitting inclusions. *Acta metallurgica*, *21*(5), 571-574.
- Murphy III, W., Roberts, J., Yale, D., & Winkler, K. (1984). Centimeter scale heterogeneities and microstratification in sedimentary rocks. *Geophysical Research Letters*, *11*(8), 697-700.
- Norris, A. N., & Johnson, D. (1997). Nonlinear elasticity of granular media. *Journal of Applied Mechanics*, *64*(1), 39-49.
- Norris, A. N., Sheng, P., & Callegari, A. J. (1985). Effective - medium theories for two - phase dielectric media. *Journal of Applied Physics*, *57*(6), 1990-1996.
- O'Connell, R. J., & Budiansky, B. (1974). Seismic velocities in dry and saturated cracked solids. *Journal of Geophysical Research*, *79*(35), 5412-5426.
- Otsu, N. (1979). A threshold selection method from gray-level histograms. *IEEE transactions on systems, man, and cybernetics*, *9*(1), 62-66.
doi:<https://doi.org/10.1109/tsmc.1979.4310076>
- Pabst, W., & Gregorová, E. (2013). Elastic properties of silica polymorphs—a review. *Ceramics-Silikaty*, *57*(3), 167-184.

- Peksa, A. E., Wolf, K.-H. A., & Zitha, P. L. (2015). Bentheimer sandstone revisited for experimental purposes. *Marine and Petroleum Geology*, 67, 701-719. doi:<https://doi.org/10.1016/j.marpetgeo.2015.06.001>
- Pervukhina, M., Gurevich, B., Dewhurst, D. N., & Siggins, A. F. (2010). Applicability of velocity—stress relationships based on the dual porosity concept to isotropic porous rocks. *Geophysical Journal International*, 181(3), 1473-1479.
- Roerdink, J. B., & Meijster, A. (2000). The watershed transform: Definitions, algorithms and parallelization strategies. *Fundamenta informaticae*, 41(1, 2), 187-228. doi:<https://doi.org/10.3233/fi-2000-411207>
- Ronneberger, O., Fischer, P., & Brox, T. (2015). *U-net: Convolutional networks for biomedical image segmentation*. Paper presented at the International Conference on Medical image computing and computer-assisted intervention.
- Saenger, E. H., Lebedev, M., Uribe, D., Osorno, M., Vialle, S., Duda, M., . . . Steeb, H. (2016). Analysis of high - resolution X - ray computed tomography images of Bentheim sandstone under elevated confining pressures. *Geophysical Prospecting*, 64(4), 848-859. doi:<https://doi.org/10.1111/1365-2478.12400>
- Saenger, E. H., Vialle, S., Lebedev, M., Uribe, D., Osorno, M., Duda, M., & Steeb, H. (2016). Digital carbonate rock physics. *Solid Earth*, 7(4), 1185-1197.
- Sain, R. (2010). *Numerical simulation of pore-scale heterogeneity and its effects on elastic, electrical and transport properties*: Stanford University.
- Sams, M. S., & Andrea, M. (2001). The effect of clay distribution on the elastic properties of sandstones. *Geophysical Prospecting*, 49(1), 128-150. doi:<https://doi.org/10.1046/j.1365-2478.2001.00230.x>
- Saxena, N., Hofmann, R., Alpak, F. O., Dietderich, J., Hunter, S., & Day-Stirrat, R. J. (2017). Effect of image segmentation & voxel size on micro-CT computed effective transport & elastic properties. *Marine and Petroleum Geology*, 86, 972-990. doi:<https://doi.org/10.1016/j.marpetgeo.2017.07.004>
- Saxena, N., Hofmann, R., Hows, A., Saenger, E. H., Duranti, L., Stefani, J., . . . Kabel, M. (2019). Rock compressibility from microcomputed tomography images: Controls on digital rock simulations. *Geophysics*, 84(4), WA127-WA139. doi:<https://doi.org/10.1190/geo2018-0499.1>

- Sayers, C. M. (1988). Stress-induced ultrasonic wave velocity anisotropy in fractured rock. *Ultrasonics*, 26(6), 311-317. doi:[https://doi.org/10.1016/0041-624x\(88\)90028-5](https://doi.org/10.1016/0041-624x(88)90028-5)
- Schlüter, S., Sheppard, A., Brown, K., & Wildenschild, D. (2014). Image processing of multiphase images obtained via X - ray microtomography: a review. *Water Resources Research*, 50(4), 3615-3639.
- Seyed Alizadeh, S. M. (2014). *Characterisation of flow and deformation in analog reservoir rocks: a micro-computed tomography approach*. University of New South Wales,
- Shapiro, S. A. (2003). Elastic piezosensitivity of porous and fractured rocks. *Geophysics*, 68(2), 482-486. doi:<https://doi.org/10.1190/1.1567215>
- Sheppard, A. P., Sok, R. M., & Averdunk, H. (2004). Techniques for image enhancement and segmentation of tomographic images of porous materials. *Physica A: Statistical mechanics and its applications*, 339(1-2), 145-151. doi:<https://doi.org/10.1016/j.physa.2004.03.057>
- Shi, H.-L., Hosdez, J., Rougelot, T., Xie, S.-Y., Shao, J.-F., & Talandier, J. (2021). Analysis of local creep strain field and cracking process in claystone by X-ray micro-tomography and digital volume correlation. *Rock Mechanics and Rock Engineering*, 1-16. doi:<https://doi.org/10.1007/s00603-021-02375-5>
- Shorten, C., & Khoshgoftaar, T. M. (2019). A survey on image data augmentation for deep learning. *Journal of Big Data*, 6(1), 1-48.
- Shulakova, V., Pervukhina, M., Müller, T. M., Lebedev, M., Mayo, S., Schmid, S., . . . Gurevich, B. (2013). Computational elastic up-scaling of sandstone on the basis of X-ray micro-tomographic images. *Geophysical Prospecting*, 61(2), 287-301. doi:<https://doi.org/10.1111/j.1365-2478.2012.01082.x>
- Sijbers, J., & Postnov, A. (2004). Reduction of ring artefacts in high resolution micro-CT reconstructions. *Physics in Medicine & Biology*, 49(14), N247. doi:<https://doi.org/10.1088/0031-9155/49/14/n06>
- Simmons, G., & Birch, F. (1963). Elastic constants of pyrite. *Journal of Applied Physics*, 34(9), 2736-2738.
- Simonyan, K., & Zisserman, A. (2014). Very deep convolutional networks for large-scale image recognition. *arXiv preprint arXiv:1409.1556*.

- Smith, T. M. (2011). Practical seismic petrophysics: The effective use of log data for seismic analysis. *The Leading Edge*, 30(10), 1128-1141.
- Smith, T. M., Sayers, C. M., & Sondergeld, C. H. (2009). Rock properties in low-porosity/low-permeability sandstones. *The Leading Edge*, 28(1), 48-59. doi:<https://doi.org/10.1190/1.3064146>
- Sun, Y., & Gurevich, B. (2020). Modeling the effect of pressure on the moduli dispersion in fluid - saturated rocks. *Journal of Geophysical Research: Solid Earth*, 125(8), e2019JB019297.
- Torquato, S., & Haslach Jr, H. (2002). Random heterogeneous materials: microstructure and macroscopic properties. *Appl. Mech. Rev.*, 55(4), B62-B63.
- Tosaya, C. A. (1982). *Acoustical properties of clay-bearing rocks*. Stanford University,
- Vanorio, T., Prasad, M., & Nur, A. (2003). Elastic properties of dry clay mineral aggregates, suspensions and sandstones. *Geophysical Journal International*, 155(1), 319-326. doi:<https://doi.org/10.1046/j.1365-246x.2003.02046.x>
- Vernik, L. (1997). *Acoustic velocity and porosity systematics in siliciclastics*. Paper presented at the SPWLA 38th Annual Logging Symposium.
- Vernik, L. (2016). *Seismic petrophysics in quantitative interpretation*: Society of Exploration Geophysicists.
- Vernik, L., & Kachanov, M. (2010). Modeling elastic properties of siliciclastic rocks. *Geophysics*, 75(6), E171-E182.
- Vincent, L., & Soille, P. (1991). Watersheds in digital spaces: an efficient algorithm based on immersion simulations. *IEEE Transactions on Pattern Analysis & Machine Intelligence*(6), 583-598. doi:<https://doi.org/10.1109/34.87344>
- Waeselmann, N., Brown, J. M., Angel, R. J., Ross, N., Zhao, J., & Kaminsky, W. (2016). The elastic tensor of monoclinic alkali feldspars. *American Mineralogist*, 101(5), 1228-1231.
- Walton, K. (1987). The effective elastic moduli of a random packing of spheres. *Journal of the Mechanics and Physics of Solids*, 35(2), 213-226.
- Wang, D. Y., Shabaninejad, M., Armstrong, R. T., & Mostaghimi, P. (2020). Physical accuracy of deep neural networks for 2d and 3d multi-mineral segmentation of rock micro-CT images. *arXiv preprint arXiv:2002.05322*.

- Washburn, K. E., Sandor, M., & Cheng, Y. (2017). Evaluation of sandstone surface relaxivity using laser-induced breakdown spectroscopy. *Journal of Magnetic Resonance*, 275, 80-89.
- Watanabe, N., Ishibashi, T., Ohsaki, Y., Tsuchiya, Y., Tamagawa, T., Hirano, N., . . . Tsuchiya, N. (2011). X-ray CT based numerical analysis of fracture flow for core samples under various confining pressures. *Engineering Geology*, 123(4), 338-346. doi:<https://doi.org/10.1016/j.enggeo.2011.09.010>
- Watt, J. P., Davies, G. F., & O'Connell, R. J. (1976). The elastic properties of composite materials. *Reviews of Geophysics*, 14(4), 541-563.
- Winkler, K. W. (1983). Contact stiffness in granular porous materials: Comparison between theory and experiment. *Geophysical Research Letters*, 10(11), 1073-1076.
- Wollner, U., Kerimov, A., & Mavko, G. (2018). Scale and Boundary Effects on the Effective Elastic Properties of 2 - D and 3 - D Non - REV Heterogeneous Porous Media. *Journal of Geophysical Research: Solid Earth*, 123(7), 5451-5465. doi:<https://doi.org/10.1029/2018jb015664>
- Wong, T. F., & Wu, L. C. (1995). Tensile stress concentration and compressive failure in cemented granular material. *Geophysical Research Letters*, 22(13), 1649-1652. doi:<https://doi.org/10.1029/95gl01596>
- Yastrebov, V. (2011). *Computational contact mechanics: geometry, detection and numerical techniques*. École Nationale Supérieure des Mines de Paris,
- Yeong, C., & Torquato, S. (1998a). Reconstructing random media. *Physical Review E*, 57(1), 495.
- Yeong, C., & Torquato, S. (1998b). Reconstructing random media. II. Three-dimensional media from two-dimensional cuts. *Physical Review E*, 58(1), 224.
- Yu, H., Zhang, Y., Lebedev, M., Wang, Z., Li, X., Squelch, A., . . . Iglauer, S. (2019). X-ray micro-computed tomography and ultrasonic velocity analysis of fractured shale as a function of effective stress. *Marine and Petroleum Geology*, 110, 472-482. doi:<https://doi.org/10.1016/j.marpetgeo.2019.07.015>
- Yurikov, A., Lebedev, M., Gor, G. Y., & Gurevich, B. (2018). Sorption - Induced Deformation and Elastic Weakening of Bentheim Sandstone. *Journal of*

Geophysical Research: Solid Earth, 123(10), 8589-8601.

doi:<https://doi.org/10.1029/2018jb016003>

Zhang, Z., Kruschwitz, S., Weller, A., & Halisch, M. (2018). Enhanced pore space analysis by use of μ -CT, MIP, NMR, and SIP. *Solid Earth*, 9(6), 1225-1238.

Zimmerman, R. W. (1990). *Compressibility of sandstones* (Vol. 29): Elsevier.

List of Figures

- Figure 2.1 Thin section of Bentheimer sandstone. (a) The sample is lower-medium-grained well-sorted sandstone. The grains are predominantly monocrystalline quartz, with potassium feldspar (black arrow) and other rock fragments. Authigenic minerals include minor amounts of clay minerals (red arrow) and moderate quartz overgrowths. Intergranular pores (blue) are abundant, but the largest blue spaces are grain-moldic dissolution pores (green arrows). The location of the high-magnification image (image b) is outlined with a red rectangle within the low-magnification image. Thin section preparation and analysis was conducted by Core Laboratories. 16
- Figure 2.2 Pressure dependent ultrasonic velocities of three Bentheimer sandstone samples at dry conditions. Samples are dried in a vacuum at 50°C for 24h. The effective pressure is varied by changing confining pressure. 17
- Figure 2.3 Digital rock workflow implemented in COMSOL..... 19
- Figure 2.4 Computed moduli change as the edge length grows. Variability of computed moduli decrease, and the values of each single sample relatively stabilise from 1.25mm edge length, but the difference among four samples remain. 21
- Figure 2.5 Boundary condition effect on the computed moduli. In each row, bulk and shear moduli computed from each of our four samples and the corresponding subsamples with half and a quarter of original edge length are plotted. The variability of moduli increases significantly while the edge length decreases as the box plot shows. Assuming the relationship between mean moduli and edge length is exponential, we derive the asymptotic moduli for each sample..... 22
- Figure 2.6 Resolution effect on greyscale and segmented images. (a) Sample D greyscale image (voxel size 1 μ m), (b) Sample D segmented image (voxel size 1 μ m), (c) Sample D greyscale image (voxel size 4 μ m), (d) Sample D segmented image (voxel size 4 μ m)..... 23
- Figure 2.7 The relationship between computed moduli and voxel size. The computed moduli based on images scanned with different voxel size and manually resampled images from one high resolution image are compared..... 24

Figure 2.8 Image processing effects on greyscale and segmented images. (a) Part of original CT image D-2, (b) after <i>non-local means filter</i> with strong parameters from (a), (c) after <i>non-local means filter</i> with mild parameters from (a), (d) <i>unsharp masking</i> from (c). (e) – (h) are segmented images from the corresponding greyscale images above.....	25
Figure 2.9 Micro-CT image of D-2 and the greyscale histogram.....	26
Figure 2.10 Greyscale images segmented into three phases using Otsu (a) and watershed (b) method, segmented into two phases with Otsu method (c).....	27
Figure 2.11 Grayscale image blurred with median filter (a) and histogram (b).	28
Figure 2.12 Three-phase segmented image with <i>Otsu</i> method (a), extracted clay phase (b), further apply <i>Opening</i> algorithm to eliminate the partial volume effect on grain boundaries (c), use clay phase as mask to extract clay particles from the unsmoothed two-phase segmented label (d) and final three-phase segmented label (e).	29
Figure 2.13 Extracted feldspar phase is mixed with random noise and grain boundaries (a), after <i>Closing</i> operation, feldspar grain becomes more connected (b), with <i>Erosion</i> operation, the noise and boundaries artefacts are removed (c), with (c) as watershed seeds, feldspar can be better segmented (d), segmented feldspar acts as Mask for Figure 9c to recover the micro cracks (e) and final segmented four-phase label (f).....	30
Figure 2.14 Optimised segmentation workflow for Bentheimer sandstone.....	30
Figure 2.15 Computed moduli with different segmentation methods versus measurements. Red and yellow marks stand for the moduli computed from two- and four-phase images respectively. The triangle marks stand for the subsamples of image B-2. The square marks stand for subsamples of image D-3. The moduli deduced from our ultrasonic measurements on Bentheimer sandstones are shown in blue diamonds. Also, we show similar measurements on clean arenites (<2% clay) with black cross and arenites (2-14% clay) with grey cross from published laboratory data set of Han et al. (1986).	31

Figure 2.16 Computed moduli with different voxel sizes versus measurements. The triangle marks stand for the subsamples of sample B. The square marks stand for subsamples of sample D. Yellow and light blue marks stand for the moduli computed from four-phase images with low and high resolution respectively. Pink marks stand for the moduli extrapolate from moduli computed based on images with two different resolutions to 1 μ m voxel size. Blue diamonds, grey and black cross are the same as Figure 2.15.	32
Figure 2.17 Computed moduli versus measurements. Green square marks stand for moduli extrapolated to 1 μ m of subsamples of sample B, and green triangle marks stand for moduli extrapolated to 1 μ m of subsamples of sample D. Blue diamonds, grey and black cross are the same as Figure 2.15.....	34
Figure 3.1 The optical microscopy (top) and TIMA (bottom) images of a thin section from S60. The image consists of quartz (shown in grey), feldspar (shown in orange) and other accessory minerals.	41
Figure 3.2 Pressure dependent properties of dry sandstone S60 from laboratory measurement: (a) helium porosity, (b) bulk and shear moduli derived from measured velocities at ultrasonic frequency in dry and glycerol-saturated conditions.	41
Figure 3.3 Diagram of the slice searching workflow in one dimension. The reference image is scanned at 0MPa (without residual stress), and the target image is scanned at 20MPa. In the reference image, two boundary slices with the index of 0 and 1254 (length of 1255 voxels) correspond to the slices with the index of 6 and 1255 (length of 1250 voxels) in the target images.....	43
Figure 3.4 Searching for the best matching slices with normalized mutual information metric. The reference image is scanned at 0MPa (without residual stress), and the target image is scanned at 20MPa. The slices with index of 0 and 1254 (length of 1255 voxels) in the reference image correspond to the slices with the index of 6 and 1255 (length of 1250 voxels) in the target image.	43
Figure 3.5 2D slices of micro-CT images showing the same physical part of sample S60 scanned at (a) 0MPa (without residual stress), (b) 0MPa (with residual stress), (c) 20MPa, and (d) 36MPa.	44

Figure 4.1 Scanning Electron Microscope (SEM) image of a Bentheimer sandstone. The location of the high-magnification image (b) is marked with a yellow dashed square within the low-magnification image (a).	54
Figure 4.2 The optical microscopy (top) and TIMA (bottom) images of a thin section from S60. The image consists of quartz (shown in grey), feldspar (shown in orange) and other accessory minerals.	56
Figure 4.3 Elastic moduli of Bentheimer and S60 sample derived from ultrasonic measurements under different pressures in dry condition.....	56
Figure 4.4 Micro-CT images of Bentheimer (left) and S60 sample (right). Only one slice of each set of image is shown here.	57
Figure 4.5 The NMR T_2 relaxation time distributions of Bentheimer and S60 sample.	57
Figure 4.6 Young's modulus map derived from nano-indentation (third row), guided by optical microscopy images (first row) and TIMA maps (second row) of S60.	61
Figure 4.7 Greyscale micro-CT images (left) and processed labels (right). Bentheimer and S60 sample images are shown in each row. In the processed label images, pore, quartz, clay, feldspar, pyrite and reconstructed grain contacts are labelled in black, blue, grey, red, green and yellow, respectively.	63
Figure 4.8 Effective moduli of Bentheimer and S60 sample based on the varying contact moduli. The effective moduli are extrapolated to zero voxel edge length using computed moduli from image set with the voxel edge length of $\sim 1\mu\text{m}$ and $\sim 0.5\mu\text{m}$	64
Figure 4.9 The correspondence between elastic moduli derived from laboratory measurements and the best-matching interpolated computed effective moduli.	65
Figure 4.10 Inverted contact stiffness from ultrasonic measurements.....	65
Figure 5.1 The cylindrical Bentheimer sandstone sample A is scanned (a) and the image is then cut into cube with the dimension of $624\times 624\times 624$ voxels (b) (only one slice is shown here). The greyscale histogram (c) of (b) only show	

two categories (pore with lower greyscale value and solid with higher greyscale value)..... 70

Figure 5.2 Original greyscale micro-CT image of Bentheimer sandstone sample A and the corresponding multi-mineral labels segmented with the workflow in Chapter 2 (only one slice is shown here). In the segmented images, pore, quartz, clay and feldspar are labelled in black, blue, grey and green, respectively. 71

Figure 5.3 U-net architecture. The feature channel number is denoted on top of each box, and the dimension of image is shown on the left side of the box. The total parameter number in this structure is 2,164,356, with 2,161,412 of them trainable..... 73

Figure 5.4 Learning process of CNN model for multi-mineral segmentation. 73

Figure 5.5 Comparison between labels from segmentation workflow and CNN model. Micro-CT images of three samples are shown in each row respectively. In the segmented images, the clay (grey) segmented by the CNN model is more consistent with human judgement. Also, the CNN model suppresses random errors in the labels from the segmentation workflow, especially for feldspar (red rectangles). However, a possible small feldspar grain is recognized by the segmentation workflow, but overlooked by the CNN model (yellow rectangle) 75

List of Tables

Table 2.1 Bentheimer sandstone micro-CT images	17
Table 2.2 Computational resource requirement for samples of difference sizes and computation efficiency.....	19
Table 2.3 The deviation of computed bulk modulus (GPa) in absolute value and percentage due to boundary effect.	24
Table 2.4 Elastic moduli of the mineral components used in computer simulations.	33
Table 3.1 Comparison of properties from images scanned at different pressures.	47
Table 4.1 Moduli of common minerals of sandstone matrix from different sources.	59
Table 5.1 CNN model segmentation statistics	76

Appendix A: Co-author contribution table

Paper 1: Elastic Moduli of Arenites From Microtomographic Images: A Practical Digital Rock Physics Workflow

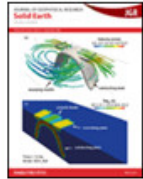
Co-author	Conception and design	Experimental methods and data acquisition	Analysis of results and discussion	Paper writing and editing
Mr. Jiabin Liang	60%	20%	60%	60%
I acknowledge that these represent my contribution to the above research output. Signature:				
Prof. Boris Gurevich	15%	—	10%	10%
I acknowledge that these represent my contribution to the above research output. Signature:				
Prof. Maxim Lebedev	5%	40%	5%	5%
I acknowledge that these represent my contribution to the above research output. Signature:				
Dr. Stephanie Vialle	5%	10%	5%	5%
I acknowledge that these represent my contribution to the above research output. Signature:				
Dr. Alexey Yurikov	—	30%	—	—
I acknowledge that these represent my contribution to the above research output. Signature:				
Dr. Stanislav Glubokovskikh	15%	—	20%	20%
I acknowledge that these represent my contribution to the above research output. Signature:				

Paper 2: High-precision tracking of sandstone deformation from micro-CT images

Co-author	Conception and design	Experimental methods and data acquisition	Analysis of results and discussion	Paper writing and editing
Mr. Jiabin Liang	60%	20%	60%	60%
I acknowledge that these represent my contribution to the above research output. Signature:				
Prof. Maxim Lebedev	15%	50%	10%	10%
I acknowledge that these represent my contribution to the above research output. Signature:				
Prof. Boris Gurevich	15%	—	10%	10%
I acknowledge that these represent my contribution to the above research output. Signature:				
Prof. Christoph H. Arns	5%	20%	5%	5%
I acknowledge that these represent my contribution to the above research output. Signature:				
Dr. Stephanie Vialle	—	10%	5%	5%
I acknowledge that these represent my contribution to the above research output. Signature:				
Dr. Stanislav Glubokovskikh	5%	—	10%	10%
I acknowledge that these represent my contribution to the above research output. Signature:				

Appendix B: Copyright Information

1. Liang, J., Gurevich, B., Lebedev, M., Vialle, S., Yurikov, A., & Glubokovskikh, S. (2020). Elastic Moduli of Arenites From Microtomographic Images: A Practical Digital Rock Physics Workflow. *Journal of Geophysical Research: Solid Earth*, 125(10), e2020JB020422.



Thank you for your order!

Dear Jiabin Liang,

Thank you for placing your order through Copyright Clearance Center's RightsLink® service.

Order Summary



Licensee:	Jiabin Liang
Order Date:	Feb 8, 2022
Order Number:	5244211016910
Publication:	Journal of Geophysical Research: Solid Earth
Title:	Elastic Moduli of Arenites From Microtomographic Images: A Practical Digital Rock Physics Workflow
Type of Use:	Dissertation/Thesis
Order Total:	0.00 AUD

View or print complete [details](#) of your order and the publisher's terms and conditions.

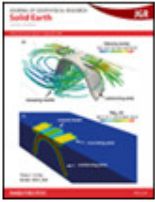
Sincerely,

Copyright Clearance Center

Tel: +1-855-239-3415 / +1-978-646-2777
customercare@copyright.com
<https://myaccount.copyright.com>



2. Liang, J., Lebedev, M., Gurevich, B., Arns, C. H., Vialle, S., & Glubokovskikh, S. (2021). High-Precision Tracking of Sandstone Deformation From Micro-CT Images. *Journal of Geophysical Research: Solid Earth*, 126(9), e2021JB022283.



Thank you for your order!

Dear Jiabin Liang,

Thank you for placing your order through Copyright Clearance Center's RightsLink® service.

Order Summary



Licensee:	Jiabin Liang
Order Date:	Feb 8, 2022
Order Number:	5244211180352
Publication:	Journal of Geophysical Research: Solid Earth
Title:	High-Precision Tracking of Sandstone Deformation From Micro-CT Images
Type of Use:	Dissertation/Thesis
Order Total:	0.00 AUD

View or print complete [details](#) of your order and the publisher's terms and conditions.

Sincerely,

Copyright Clearance Center

Tel: +1-855-239-3415 / +1-978-646-2777
customercare@copyright.com
<https://myaccount.copyright.com>



Every reasonable effort has been made to acknowledge the owners of copyright material. I would be pleased to hear from any copyright owner who has been omitted or incorrectly acknowledged.